UNIVERSITÄT
LEIPZIG

REPORT
Halbleiterphysik
Semiconductor Physics
2019

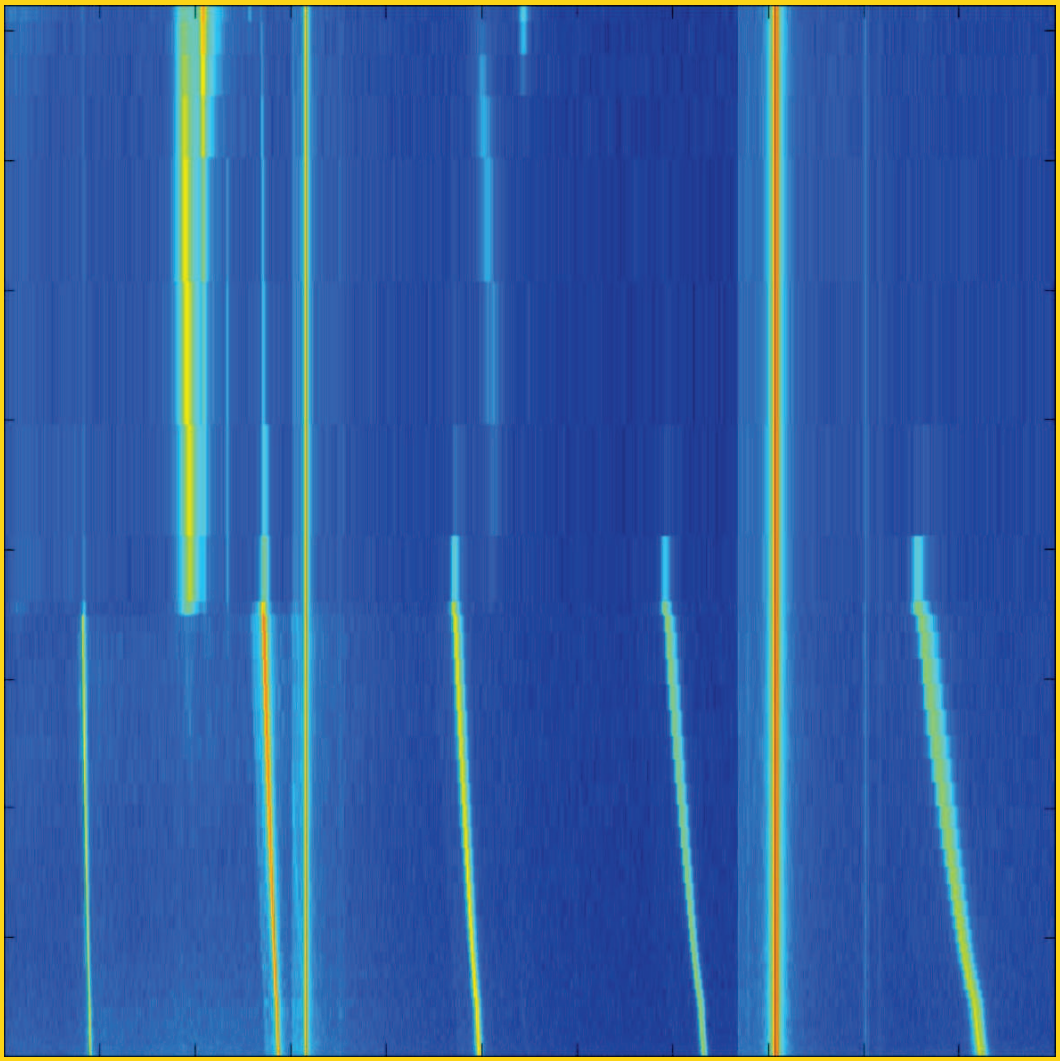

The Semiconductor Physics Group of Universität Leipzig, Report 2019
M. Grundmann (Ed.)

Technical Editor: Anja Heck

online available at
http://research.uni-leipzig.de/hlp/

Front cover

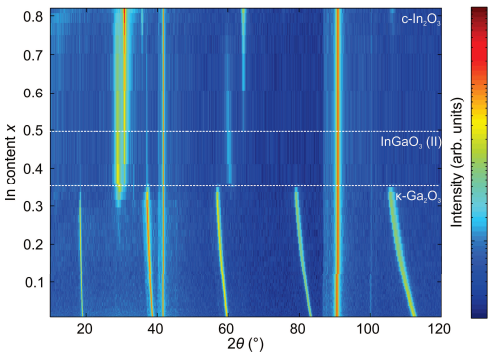

False color map of 55 XRD 2θ-ω scans acquired of an $(In_xGa_{1-x})_2O_3$ thin film with lateral varying cation composition. Up to an In-content of $x = 0.35$ the orthorhombic polymorph is apparent indicated by its characteristic reflection peaks. For $0.35 < x < 0.5$ the hexagonal $InGaO_3$ (II) and for $x \geq 0.5$ the cubic bixbyte phase was observed. For further information see section 2.5.1 and doi:10.1063/1.5054394

Back cover

TCO 2019, Photo by Swen Reichhold

Abteilung Halbleiterphysik

Felix-Bloch-Institut für Festkörperphysik

Fakultät für
Physik und Geowissenschaften

Universität Leipzig

Semiconductor Physics Group

Felix Bloch Institute for Solid State Physics

Faculty of Physics and Earth Sciences

Universität Leipzig

Report 2019

Address

Semiconductor Physics Group

Linnéstraße 5
D-04103 Leipzig, Germany

Phone: +49 341 97-32650
Fax: +49 341 97-32668
WWW: http://research.uni-leipzig.de/hlp/
Mailing address: Postfach 230001, D-04081 Leipzig, Germany

Preface

Our research report gives you an overview of the recent activities and discoveries of the Semiconductor Physics group. We hope it finds your interest and gives you a scientific stimulus.

We welcomed many national and international colleagues for the TCO2019 meeting. Twenty-five invited speakers covered the actual developments in the fields of transparent conductive and semiconducting oxides, from new materials and fabrication methods, optical and electrical properties to high power devices. A special highlight was the first 'Bädeker Lecture' on 'Novel Transparent Oxide Semiconductors' by Prof. Hideo Hosono from the Tokyo Institute of Technology. He also came to Leipzig as the Mercator Professor of the newly established Research Unit FOR 2857 of Deutsche Forschungsgemeinschaft on copper iodide. The historical focus on '120 Years of Drude Theory of the Electron Gas' was enriched by two very instructive tutorials on electrical and optical properties of the electron gas by Prof. Debdeep Jena (Cornell) and Mrs Prof. Vanya Darakchieva (Linköping University).

Figure 1: Participants of TCO 2019, Photo by Swen Reichold

Some of this year's scientific highlights are excellent device properties of amorphous zinc-tin-oxide based devices, controlled formation of thin film Ga_2O_3 and its alloys with indium and aluminum in the orthorhombic κ-phase (promising large polarization effects), cooperative work with Humboldt University Berlin and Ohio State University on band offsets as well as the eventual PRL publication of our investigations on Voigt exceptional points in anisotropic ZnO-based planar microcavities.

We are largely indebted to our funding agencies in particular Deutsche Forschungsgemeinschaft (DFG). Our newly established Research Unit "Copper Iodide as Multifunctional Semiconductor" has started work in October. In eight projects colleagues from Leipzig, Jena and Halle cooperate one this novel widegap p-conducting material and its device perspectives. We are grateful for the continued funding of Sonderforschungsbereich SFB 762 "Functionality of Oxide Interfaces" that has ended by now after twelve years. The work of our students and researchers together with our academic and industrial partners near and far was fruitful and enjoyable and thus it is with great pleasure that the Semiconductor Physics Group presents their progress report.

Leipzig, *Marius Grundmann*
April 2020

Contents

I Report of the Semiconductor Physics Group 13

1 Structure and Staff of the Semiconductor Physics Group 15

2 Reports 17

2.1 Low-voltage operation of ring oscillators based on amorphous zinc tin oxide fabricated at room temperature . . . 17

2.2 Low-voltage, high-gain inverters based on amorphous zinc tin oxide on flexible substrates . . . 19

2.3 Metal-semiconductor field-effect transistors based on amorphous zinc oxynitride . . . 21

2.4 Combinatorial material synthesis by pulsed laser ablation of segmented targets . . . 23

2.5 Investigations of orthorhombic, κ-$(Al_xGa_{1-x})_2O_3$ thin films grown by tin-assisted CCS- and VCCS-PLD . . . 25

2.5.1 Material properties of a κ-$(Al_xGa_{1-x})_2O_3$ thin film with a lateral cation gradient . . . 25

2.5.2 Epitaxial κ-$(Al,Ga)_2O_3$ thin films and heterostructures by tin-assisted VCCS-PLD . . . 27

2.5.3 Epitaxial stabilization of single phase κ-$(In_xGa_{1-x})_2O_3$ thin films on c-sapphire and κ-Ga_2O_3(001) templates by tin-assisted VCCS-PLD . . . 29

2.6 pn-heterojunction diodes with β-Ga_2O_3 . . . 31

2.7 High-quality Schottky barrier diodes on β-gallium oxide thin films on glass substrate . . . 33

2.8 Universal Relation for the Orientation of Dislocations from Prismatic Slip Systems in Hexagonal and Rhombohedral Strained Heterostructures 35

2.9 Band offsets of dielectric coatings on monoclinic $(In,Ga)_2O_3$ and $(Al,Ga)_2O_3$ . . . 37

2.10 Optimized processing strategies for Schottky barriers on n-type semiconducting oxides . . . 38

2.11 Increased breakdown field and improved interfacial roughness in $BaTiO_3$-$BiFeO_3$ multilayers via eclipse-PLD . . . 40

2.12 Raman tensor determination of uniaxial materials . . . 43

2.13 Exceptional points in anisotropic layered photonic structures . . . 44

2.13.1 Voigt exceptional points in a planar microcavity and thin films . 44

2.13.2 Empirical observation of EPs in microcavities based on Mueller matrix symmetries . . . 46

2.14 Femtosecond time-resolved imaging of the dielectric function of ZnO . 48
2.15 Ellipsometric evidence for defect induced magnetism in spinel ferrite thin films 50
2.16 Dielectric function of κ-(In,Al,Ga)$_2$O$_3$ thin films 52
2.17 Low temperature optical properties of CuI thin film 53
2.18 Influence of the excitation wavelength on the emission properties of carbon nanodots 54
2.19 Structural and optical properties of oxygen-doped TiN thin films 56
2.20 A vortex plate in the Mach-Zehnder Interferometer 58

3 Funding, Organizational Duties, External Cooperations 59
3.1 Funding 59
3.2 Organizational Duties 61
3.3 External Cooperations 62

4 Publications 65

5 Graduations 75

6 Guests 77

Author Index 79

I

Report of the Semiconductor Physics Group

1

Structure and Staff of the Semiconductor Physics Group

Prof. Dr. Marius Grundmann

Secretary

Anja Heck
Johanna Lendewig
Birgit Wendisch

Technical staff

Dipl.-Phys. Gabriele Benndorf
Monika Hahn
Dipl.-Ing. Holger Hochmuth
Dipl.-Phys. Jörg Lenzner
Axel Märcker

Academic staff

Dr. Robert Karsthof
Prof. Dr. Michael Lorenz
PD Dr. Rainer Pickenhain
Dr. Anna Reinhardt
Prof. Dr. Bernd Rheinländer (retired)
Dr. Peter Schlupp
Dr. Rüdiger Schmidt-Grund
Dr. Daniel Splith
Dr. Chris Sturm
Dr. Holger von Wenckstern
Dr. Wenlei Yu (guest)
Dr. Chang Yang
Dr. Vitaly Zviagin

PhD candidates

Michitaka Fukumoto, M.Sc. (guest, JSPS)
Fangjuan Geng, M.Sc. (guest, CSC)
Anna Hassa, M.Sc.
Oliver Herrfurth, M.Sc.
Ron Hildebrandt, M.Sc.
Stefan Hohenberger, M.Sc.
Tanja Jawinski, M.Sc.
Stefan Kammer, M.Sc. (First Sensor AG, Berlin)
Max Kneiß, M.Sc.
Evgeny Krüger, M.Sc.
Oliver Lahr, M.Sc.
Fabian Schöppach, M.Sc.
Philipp Storm, M.Sc.
Tillmann Stralka, M.Sc.
Lukas Trefflich, M.Sc.
Sofie Vogt, M.Sc.
Antonia Welk, M.Sc.

Students

Yousif Abou Leila
Michael Bar
Felix-Florian Delatowski
Sebastian Henn
Mario Klebahn
Catharina Krömmelbein
Andreas Müller
Sophie Müller
Eduard Rose
Laurenz Thyen
Christopher Walter
Benjamin Wehr
Jonathan Wernersson

2

Reports

2.1 Low-voltage operation of ring oscillators based on amorphous zinc tin oxide fabricated at room temperature

O. Lahr, S. Vogt, H. von Wenckstern, M. Grundmann

During the last two decades, transparent amorphous oxide semiconductors (TAOSs) have emerged into a novel, distinct area of research for transparent and flexible electronics and since then, the field has grown rapidly toward, for instance, TFT back planes for next-generation flat-panel displays [1]. Multi-cation TAOSs exhibit, alongside their fairly high transparency in the visible range, a superior free-carrier mobility compared to conventional amorphous silicon thin films and enable homogeneous large-area deposition at low-temperatures for the fabrication of low-cost, transparent and flexible devices. The by far most mature and already widely commercially exploited representative indium gallium zinc oxide, however, consists of rare elements such as indium and gallium that innovative research is attempting to substitute by materials consisting of abundant cations only.

Recently, first inverter circuits comprising MESFETs and JFETs based on room-temperature-deposited amorphous zinc tin oxide (ZTO) with peak gain magnitude (pgm) of 141 and uncertainty levels as low as $V_{\mathrm{UC}} = 160\,\mathrm{mV}$ for an operating voltage of only 3 V have been reported, rendering ZTO a suitable and promising candidate for a more sustainable approach to flexible and transparent electronics [2, 3]. In this work, we present Schottky diode FET logic (SDFL) inverters as well as ring oscillators comprising MESFETs based on *n*-ZTO channels that have been deposited entirely at room temperature (RT) and did not require any additional annealing treatment to achieve excellent device functionality.

ZTO layers with a cation composition of 1 : 1 Zn : Sn have been deposited on $10 \times 10\,\mathrm{mm}^2$ SiO_2 substrates by radio frequency long-throw magnetron sputtering at RT using a ceramic target. Between the two necessary SDFL design-related metallization steps, a 200 nm thick insulating HfO_y layer was deposited at RT. A respective schematic cross section through a MESFET sample, illustrating the material stacking order, is depicted in Fig.2.1 (a). On top of the active channel an intrinsic ZTO layer (*i*-ZTO) followed by a PtO_x and a metallic Pt capping layer are deposited to function as gate

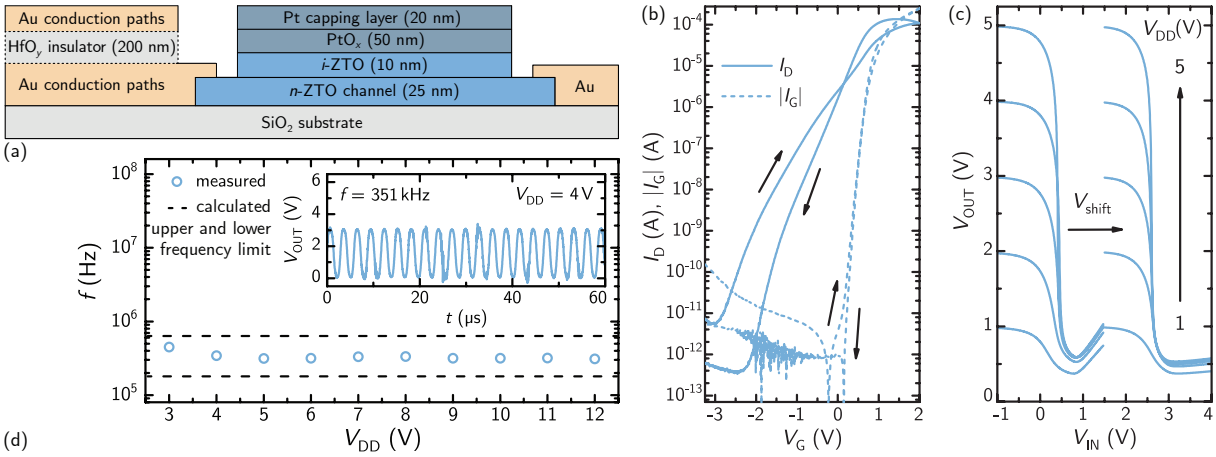

Figure 2.1: (a) Schematic cross section through a MESFET sample visualizing the basic material stacking order. (b) Transfer characteristic and the gate leakage current of a ZTO-based MESFET and (c) Corresponding voltage transfer characteristics of an SDFL inverter for various operating voltages ranging from 1 V to 5 V. For inverters with level shift, a total voltage drop of $V_{\text{shift}} \approx 2.5$ V has been observed across the three level shifting diodes. (d) Oscillation frequencies of a typical ZTO-based three-stage ring oscillator versus the applied operating voltage V_{DD}; dashed lines mark the frequency range expected from the model of Klüpfel *et al.* (see text). The inset displays an example for a measured time trace of a ring oscillator at $V_{DD} = 4$ V, exhibiting an oscillation frequency of 351 kHz

contact. The i-ZTO and the reactively sputtered PtO_x layer ensure low leakage current due to a saturation of under-coordinated cation bonds via transfer of oxygen from PtO_x and *i*-ZTO to ZTO [4].

RT transfer characteristics and the corresponding gate leakage current for both voltage sweep directions of a ZTO-based MESFET with gate width and length of $W = 200\,\mu$m and $L = 3\,\mu$m, respectively, are depicted in Fig.2.1 (b). Investigated MESFETs exhibit a clear field effect with an ON/OFF current ratio as high as 8.6 orders of magnitude, can be switched on and off within a voltage range of less than 3 V and are normally-on with threshold voltages between -0.6 V and -0.3 V. The obtained sub-threshold swing and maximum transconductance are 250 mV dec^{-1} and 205 μS, respectively. Voltage transfer characteristics of a ZTO-based SDFL inverter without and with three level-shifting diodes are depicted in Fig. 2.1 (c) for operating voltages V_{DD} between 1 V and 5 V. The basic SDFL circuit implements PtO_x/*i*-ZTO/ZTO Schottky barrier diodes for level shifting in order to switch a subsequent inverter. An additional transistor with its gate and source shorted is supplied with a negative operating voltage of $V_{\text{bias}} = -2$ V and acts as constant-current bias source for the level-shifting diodes. The inverters display stable performance under operation with level shift and exhibit a pgm as high as 83 and $V_{UC} = 0.5$ V for an operation voltage of 5 V.

Measured frequencies as a function of V_{DD} as well as the typical time trace of a three-stage ZTO-based SDFL ring oscillator are depicted in Fig. 2 (d). A maximum oscillation frequency of 451 kHz is observed at $V_{DD} = 3$ V, corresponding to single stage delay times of 277 ns. Oscillations start to occur at a minimum operating voltage of 3 V, which is attributed to the voltage drop across the level shifting diodes. The observed frequencies are independent of V_{DD} as expected for SDFL circuits, since the supply current is limited by the pull-up and pull-down transistors which operate in saturation and

act as constant current sources. An analytical model, developed by Klüpfel *et al.*, has been employed to estimate the single stage delay time $\tau_D = \delta V C_G F / I_{PU}$ based on easily obtainable FET and inverter quantities, where δV, C_G, I_{PU}, and F are the voltage swing which is present at the input of each driving gate, the driving gate capacitance, the saturation current of the pull-up FET, and the fan-out of each inverter, respectively [6]. The expected maximum and minimum oscillation frequencies are represented by the dashed lines in Fig. 2 (d). Overall, the presented results prove feasibility of amorphous ZTO as a promising candidate for cost-efficient, sustainable electronics and furthermore show that low-temperature-processed ZTO-based integrated circuits can compete with previously reported high-temperature-treated devices in terms of their performance.

[1] H. Hosono, Journal of Non-Crystalline Solids **352**, 851 (2006)
[2] S. Vogt, H. von Wenckstern, M. Grundmann Appl. Phys. Lett. **113**, 133501 (2018)
[3] O. Lahr, Z. Zhang, F. Grotjahn, P. Schlupp, S. Vogt, H. von Wenckstern, A. Thiede, M. Grundmann, IEEE Transact. Electr. Dev. **66**, 3376 (2019)
[4] T. Schultz S. Bitter, P. Schlupp, H. von Wenckstern, N. Koch, M. Grundmann, Phys. Rev. Appl. **9**, 064001 (2018)
[5] O. Lahr, S. Vogt, H. von Wenckstern, M. Grundmann, Adv. Electron. Mater. **5**, 1900548 (2019)
[6] F. Klüpfel, H. von Wenckstern, M. Grundmann , Adv. Electron. Mater. **2**, 1500431 (2016)

2.2 Low-voltage, high-gain inverters based on amorphous zinc tin oxide on flexible substrates

P. Schlupp, S. Vogt, H. von Wenckstern, M. Grundmann

Amorphous oxide semiconductors (AOS) exhibit high electron mobilities even when fabricated at low temperature [1, 2]. This enables the use of thermally unstable but flexible plastic substrates. With that, a cost-efficient roll-to-roll fabrication is possible. The most common AOS is indium gallium zinc oxide, which is already used in pixel drivers for flat panel displays [3]. Since indium and gallium are rare, we investigate the AOS zinc tin oxide (ZTO) [4]. In this work, junction field-effect transistors (JFET) with ZTO channels fabricated on flexible polyimide (PI) are presented. The gate diode of the JFETs was realized using p-type nickel oxide. Furthermore, inverters containing two identical FETs are demonstrated. All devices were investigated before and after tensile bending stress applied by bending them to radii from 5 to 2 mm.

The ZTO thin films were fabricated by sputter deposition using a long-throw magnetron sputter system from MANTIS [5]. The target consists of 67 wt.% SnO_2 and 33 wt.% ZnO. The thin films have a Sn:Zn ratio of about 1:1. To avoid an electron accumulation at the substrate/thin film interface, prior to the deposition of the conducting ZTO a semi-insulating layer was deposited. This layer has a higher oxygen content. The process was developed in this group and details can be found in Vogt *et al.* [6]. The about 60 nm thick NiO gate layer was fabricated by pulsed laser deposition at an oxygen pressure of 0.1 mbar. Source and drain contacts consist of gold and are fabricated

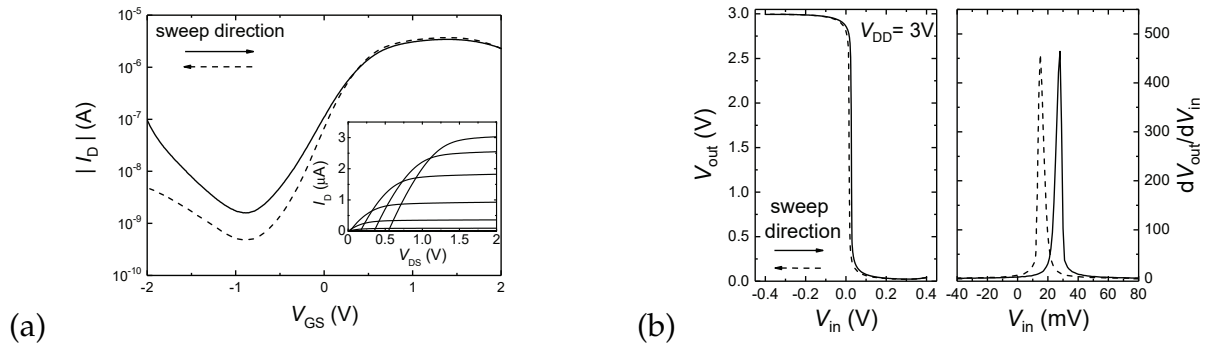

Figure 2.2: (a) Transfer characteristics of JFET with ZTO channel and NiO gate material. A drain voltage of $V_d = 2\,V$ is used. In the inset, the output characteristics is depicted for different gate voltages. (b) Voltage transfer characteristics of the ZTO-based inverters and voltage gain using a supply voltage $V_{DD} = 3\,V$.

by sputtering. All layers were fabricated entirely at room temperature. Structuring was performed using photolithography (lift-off) including two 90 s baking steps at 90° C.

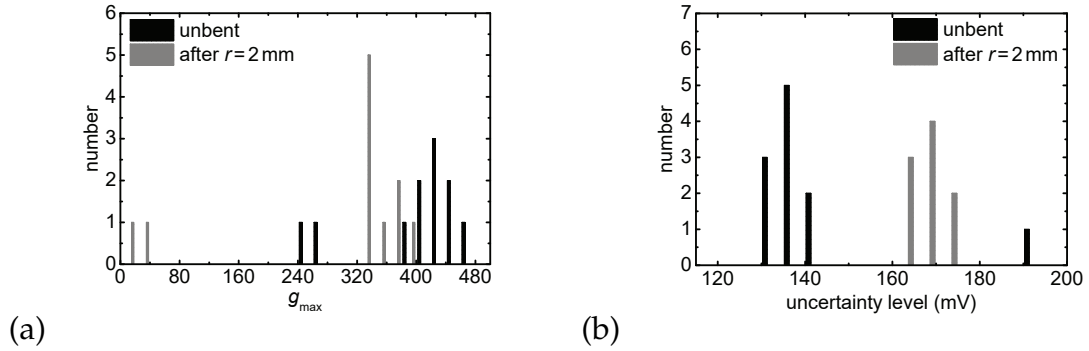

Figure 2.3: Statistics of the peak gain magnitude (pgm, left) and the uncertainty level (ucl, right) of eleven inverters on one sample before and after tensile bending at $r = 2\,mm$. In the ucl, two inverters are not shown due to the high ucl of > 0.5 V.

A typical transfer characteristic of a ZTO-based JFET on flexible PI is depicted in figure 2.2(a). The current increase at gate voltages smaller than −1 V is due to the leakage current through the gate diode. The current rectification at ±1 V is at most four orders of magnitude and needs further optimization. The subthreshold swing is about 340 mV/dec and the threshold voltage is slightly below zero volts. The output characteristics, depicted in the inset of figure 2.2(a) shows a clear saturation for higher drain voltages.

Two identical JFETs were integrated to a simple inverter circuit. The voltage transfer characteristic for a supply voltage $V_{DD} = 3\,V$ is depicted in figure 2.2(b). Full swing is obtained. The switching point is at about zero volts because of the identical geometry of the JFETs used. It could be shifted by using, e.g., a Schottky diode FET logic [7]. The voltage gain, which is the negative first derivative, is depicted in figure 2.2(b) on the right side. The maximum gain, called the peak gain magnitude (pgm) is 464. The uncertainty level (ucl), that characterizes the transition width, is about 130 mV. After bending a sample with 11 inverters on a metal rod with 2 mm radius, pgm and ucl

change for most of the inverters only slightly. The values before and after bending are depicted in figure 2.3. This makes the inverters suitable for applications in more complex circuits. The bending stress can be further reduced using encapsulation to shift the devices in the neutral plane of the bending stress.

[1] K. Nomura, H. Ohta, A. Takagi, T. Kamiya, M. Hirano and H. Hosono, Nature **432**, 488 (2004)
[2] J. S. Park, W.-J. Maeng, H.-S. Kim, and J.-S. Park, Thin Solid Films **520**(6), 1679 (2012)
[3] J.-S. Park, T.-W. Kim, D. Stryakhilev, J.-S. Lee, S.-G. An, Y.-S. Pyo, D.-B. Lee, Y. G. Mo, YD.-U. Jin and H. K Chung, Appl. Phys. Lett. **95**, 013503 (2009)
[4] P. Schlupp, F.-L. Schein, H. von Wenckstern and M. Grundmann, Adv. Electron. Mater. **1**, 1400023 (2015)
[5] H. Frenzel, T. Dörfler, P. Schlupp, H. von Wenckstern and M. Grundmann, physica status solidi (a) **212**(7), 1482 (2015)
[6] S. Vogt, H. von Wenckstern and M. Grundmann, Appl. Phys. Lett. **113**(13), 133501 (2018)
[7] R. C. Eden, B. M. Welch and R. Zucca, IEEE J. Solid-State Circuits **SC-13**, 419 (1978)

2.3 Metal-semiconductor field-effect transistors based on amorphous zinc oxynitride

A. Reinhardt, H. von Wenckstern, M. Grundmann

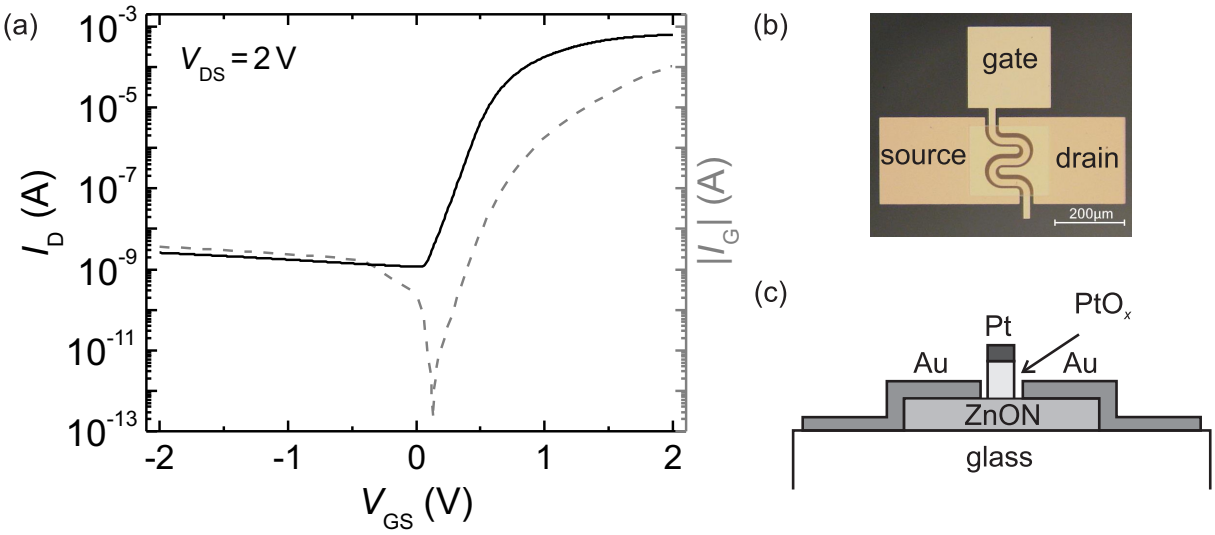

Figure 2.4: (a) Transfer characteristic (black) and absolute gate current $|I_G|$ (grey dashed line) of a ZnON MESFET with a gate width-to-length ratio of 430 μm/10 μm. (b) exemplary laser microscope image (top view) and (c) Schematic side view of the fabricated device structure.

Electronic devices based on amorphous oxide semiconductors (AOS) provide a variety of advantages such as low-temperature and homogeneous large-scale fabrication in combination with high carrier mobility, enabling for example low-cost, high-performance transistors on flexible substrates [1].

Amorphous zinc oxynitride (a-ZnON) came into focus as active channel material for high-performance thin-film transistors (TFTs) due to a superior field-effect mobility $> 50\,\mathrm{cm^2V^{-1}s^{-1}}$, which is beneficial to overcome the performance limits inherent to amorphous silicon-based devices [2, 3]. Furthermore, the incorporation of nitrogen in this multi-anion compound shifts the oxygen vacancy state, being a source of bias-stress instability and performance changes of multi-cation AOS-based TFTs under visible light illumination, into the valence band resulting in an inherent stability of ZnON TFTs under bias illumination stress [4].

Up to now, the reported ZnON-based TFTs are metal-insulator-semiconductor field-effect transistors (MISFETs). We present the metal-semiconductor field-effect transistors (MESFETs) comprising a-ZnON as active channel material [5]. MESFETs are especially suited for low-voltage and high-frequency applications due to the missing gate dielectric. For device fabrication, we used DC-sputtered a-ZnON thin films on glass substrates, which were supplied by Y. Ye (formerly *Applied Materials, Inc.*). Hall effect measurements at room temperature reveal a free electron concentration of $n = 1.5\times10^{17}\,\mathrm{cm^{-3}}$ and a Hall mobility of $\mu_{\mathrm{Hall}} \approx 100\,\mathrm{cm^2V^{-1}s^{-1}}$ for the as-received a-ZnON thin film. Top-gate TFT structures were processed by means of standard photolithography and lift-off. Defined 60-nm-thick ZnON channel mesas were formed by wet chemical etching. The source and drain electrodes were fabricated by DC sputtering of 40 nm-thick Au and patterned using lift-off technique. Finally, the gate contact was realized by reactively sputtered platinum providing the formation of a Schottky barrier diode. The investigated MESFET device structure can be seen in Fig. 2.4 (b,c).

The PtO_x/ZnON Schottky barrier diodes yield sufficient rectification behavior and low ideality factors of 1.4±0.1 resulting in excellent MESFET performance. Fig. 2.4 (a) depicts a typical transfer characteristic and the respective absolute gate current $|I_G|$ of the investigated MESFETs at a drain-source voltage of $V_{DS} = 2\,\mathrm{V}$. Best MESFET devices exhibit a drain-current on/off ratio of 5×10^5, $75\,\mathrm{cm^2V^{-1}s^{-1}}$ channel mobility, a near-zero threshold voltage of 0.4 V and a minimal subthreshold swing of $112\,\mathrm{mV\,dec^{-1}}$ within a gate voltage sweep of less than 2 V rendering them interesting for inexpensive, fast-switching low-voltage applications. The obtained drain-current on/off-ratio lies in the typical range for AOS-based MESFET devices whereas the channel mobility is much higher, cf. $I_{on}/I_{off} = 10^4 - 10^6$ and $\mu_{ch} = 3 - 12\,\mathrm{cm^2V^{-1}s^{-1}}$ for amorphous zinc tin oxide [6, 7].

[1] L. Petti, N. Münzenrieder, C. Vogt, H. Faber, L. Büthe, G. Cantarella, F. Bottacchi, T. D. Anthopoulos and G. Tröster , Appl. Phys. Rev. **3**, 021303 (2016)
[2] Y. Ye, R. Lim and J. M. White, J. Appl. Phys. **106**, 074512 (2009)
[3] H.-S. Kim, S. H. Jeon, J. S. Park, T. S. Kim, K. S. Son, J.-B. Seon, S.-J. Seo, S.-J. Kim, E. Lee, J. G. Chung, H. Lee, S. Han, M. Ryu, S. Y. Lee and K. Kim , Sci. Rep. **3**, 1459 (2013)
[4] M. Ryu, T. S. Kim, K. S. Son, H.-S. Kim, J. S. Park, J.-B. Seon, S.-J. Seo, S.-J. Kim, E. Lee, H. Lee, S. H. Jeon, S. Han, S. Y. Lee, in Proc. IEEE International Electron Devices Meeting, 5.6.1-5.6.3 (2012)
[5] A. Reinhardt, H. von Wenckstern and M. Grundmann, Adv. Electron. Mater. (2020), DOI: 10.1002/aelm.201901066
[6] G. T. Dang, T. Kawaharamura, M. Furuta and M. W. Allen, Appl. Phys. Lett. **110**, 073502 (2017)

[7] S. Vogt, H. von Wenckstern and M. Grundmann, Appl. Phys. Lett. **113**, 133501 (2018)

2.4 Combinatorial material synthesis by pulsed laser ablation of segmented targets

H. von Wenckstern, M. Kneiß, A. Hassa, P. Storm, D. Splith, M. Grundmann

Combinatorial material synthesis has led to a significant acceleration in the optimization of solid state alloys. Two approaches to combinatorial material synthesis based on ablation of segmented ceramic targets during pulsed-laser deposition (PLD) were recently developed at Universität Leipzig [1–3] and are shortly reviewed herein. Azimuthally or radially segmented targets enable the creation of in-plane (lateral) and out-of-plane (vertical) continuous composition spreads (CCS), respectively. Radially segmented targets can additionally be used to synthesize a discrete binary material library.

The creation of lateral composition spreads requires offset-PLD, for which the centre of the substrate and the position of the laser spot on the target have a lateral spatial shift [1]. Further, the substrate and target must be rotated synchronously. These two conditions enable a spatial control of the material flux composition incident on the substrate. In fig. 2.5 potential target segmentations and the resulting lateral variation of the alloy composition are depicted. A target, composed of two semicircular segments, leads to a unidirectional change of composition, while the composition does not vary along lines being perpendicular to the gradient. Two- or three-directional lateral material gradients can be realized with three- or four-fold segmented targets. We have characterized material properties of ternary alloys of semiconducting oxides synthesized using two-fold segmented targets . These include (Mg,Zn)O, $(In,Ga)_2O_3$, $(Al,Ga)_2O_3$, (Zn,Sn)O [3]. Threefold segmented targets were used for the deposition of a two-directional material variation of (Mg,Zn)O:Al and (Mg,Zn)O:Ga thin films allowing to study the influence of donor concentration as a function of the ternary alloy composition [4].

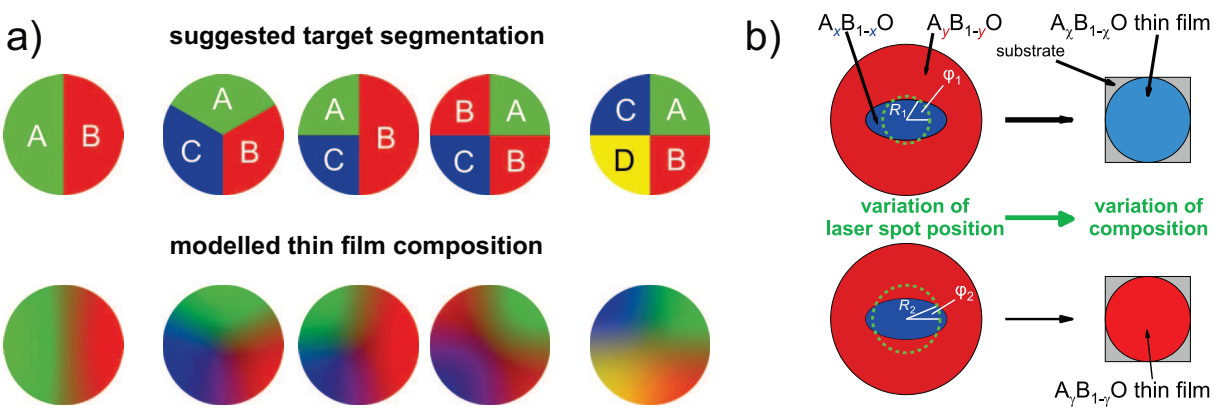

Figure 2.5: Schematic representation of i) potential azimuthal PLD target segmentations and resulting lateral variation of material composition and ii) radial target segmentation and thin film composition for two radially distinct ablation tracks.

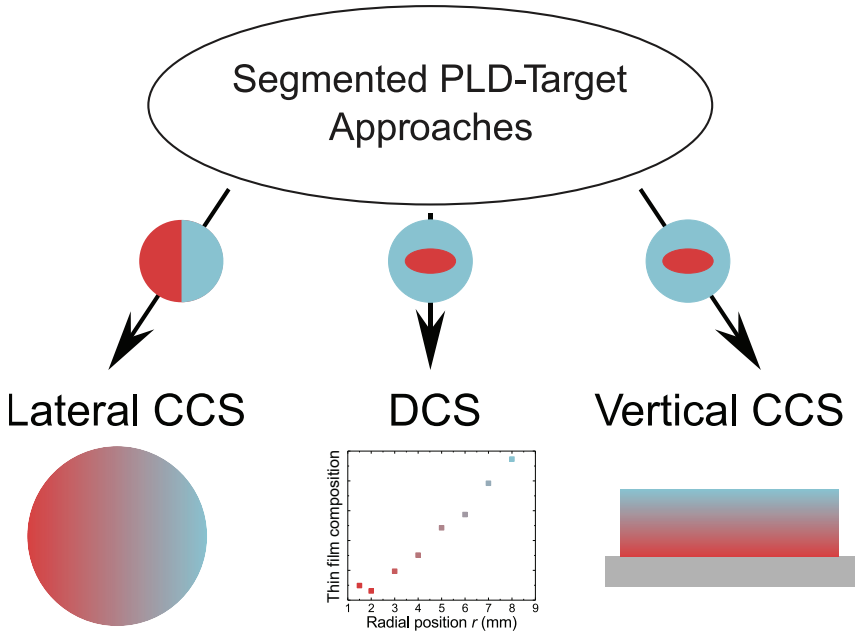

Figure 2.6: Schematic representation of variants of combinatorial synthesis based on pulsed laser deposition using azimuthally (left) and radially (middle, right) segmented ceramic targets, respectively.

Radially segmented targets have been implemented to create compositional gradients in growth direction as necessary for, e.g., strain engineering [2, 3]. Quasi-continuous changes of the cation ratio were demonstrated for ternary (Mg,Zn)O [2, 3]. Radially segmented targets additionally enable discrete combinatorial synthesis which was employed for deposition of sample sets of ternary (Mg,Zn)O, $(In,Ga)_2O_3$ and $(Al,Ga)_2O_3$ [2, 3, 5].

Fig. 2.6 shows a schematic comparison of the different segmented target approaches established in Leipzig and the corresponding types of composition spread or discrete material library. An in-depth review can be found in Ref. [3].

[1] H. von Wenckstern, Z. Zhang, F. Schmidt, J. Lenzner, H. Hochmuth, M. Grundmann, CrystEngComm **15**, 10020, (2013)
[2] M. Kneiß, P. Storm, G. Benndorf, M. Grundmann, H. von Wenckstern, ACS Comb. Sci. **20**, 643 (2018)
[3] H. von Wenckstern, M. Kneiß, A. Hassa, P. Storm, D. Splith, and M. Grundmann, phys. stat. sol. (b), **30**, 1900626 (2019)
[4] A. Mavlonov, S. Richter, H. von Wenckstern, R. Schmidt Grund, M. Lorenz, and M. Grundmann, J. Appl. Phys. **120**, 205703 (2016), A. Mavlonov, S. Richter, H. von Wenckstern, R. Schmidt Grund, J. Lenzner, M. Lorenz, and M. Grundmann, physica status solidi (a) **212**, 2850 (2015)
[5] M. Kneiß, A. Hassa, D. Splith, C. Sturm, H. von Wenckstern, M. Lorenz, and M. Grundmann, APL Mater. **7**, 101102 (2019), P. Storm, M. Kneiß, A. Hassa, T. Schultz, D. Splith, H. von Wenckstern, N. Koch, M. Lorenz, and M. Grundmann, APL Mater. **7**, 111110 (2019)

2.5 Investigations of orthorhombic, κ-$(Al_xGa_{1-x})_2O_3$ thin films grown by tin-assisted CCS- and VCCS-PLD

Gallium oxide can potentially be applied in electronic high-power devices, because of its exceptional material properties such as large breakdown fields and high Baliga's figure of merit [1]. Further, quantum-well infrared photodetectors, UV-photodetectors, touch panel displays, or optical communication systems [2] may become fields of applications. The wide bandgap semiconductor can crystallize in different polymorphs [3], with the monoclinic β-gallia structure being the most studied polymorph, so far. The orthorhombic κ-polymorph attracted in the recent years increasing interest, because of its predicted large spontaneous electrical polarization of 23 μC/cm^2 [4]. A jump of the polarization at the interface of κ-Ga_2O_3/κ-$(Al_xGa_{1-x})_2O_3$ heterostructures induces an accumulation of charge carriers, which can be utilized within high-electron mobility transistors. Hence, studies of the stabilization of the κ-phase and composition-dependent material properties, such as lattice parameters, optical bandgaps or growth rates, are of interest.

2.5.1 Material properties of a κ-$(Al_xGa_{1-x})_2O_3$ thin film with a lateral cation gradient

A. Hassa, C. Sturm, M. Kneiß, D. Splith, H. von Wenckstern, T. Schultz[*†], N. Koch[*†], M. Lorenz, M. Grundmann

[*]Department of Physics, Humboldt-Universität zu Berlin
[†]Helmholtz-Zentrum für Energie und Materialien GmbH

To study the material properties of κ-$(Al_xGa_{1-x})_2O_3$ in dependence on the cation concentration, a two inch diameter thin film with a lateral continuous composition spread (CCS) was prepared by pulsed laser deposition (PLD) with CCS approach [5]. For that, a twofold segmented target consisting of Ga_2O_3 and Al_2O_3 was ablated. Both segments were doped with tin to facilitate the growth of the orthorhombic polymorph [6]. Due to the CCS-approach a lateral cation gradient forms that was spatially resolved by energy-dispersive X-ray spectroscopy (EDX) measurements. The resulting false color map, depicted in Fig. 2.7, reveals an Al-content between $x = 0.08$ and $x = 0.78$. Parallel to the cation gradient, a 10 mm wide stripe was sawed out and investigated by means of XRD measurements to identify the crystallographic structure, epitaxial growth and rotational domains. 55 XRD 2θ-ω scans, acquired along the gradient, are depicted in dependence on x in Fig. 2.7(c) and reveal the growth of κ-$(Al_xGa_{1-x})_2O_3$ up to $x = 0.46$ [7] being the highest reported Al-content in the orthorhombic polymorph on c-sapphire, so far. XRD ϕ-scans confirmed the κ-phase as well as the growth in three rotational domains. The c-lattice constants were determined from the $(00n)$-reflexes and are shown in Fig. 2.7(c). Their dependence on the Al-content can be described by

$$c(x)(\text{Å}) = \begin{cases} (9.271 \pm 0.001) - (0.333 \pm 0.008) \cdot x, & \text{for } 0.07 \leq x \leq 0.13 \\ (9.276 \pm 0.001) - (0.357 \pm 0.002) \cdot x, & \text{for } 0.14 \leq x \leq 0.46. \end{cases} \tag{2.1}$$

Further, spectroscopic ellipsometry was utilized to estimate the optical bandgap E_g

and growth rate r. Both are presented in Fig.2.7(b) as a function of x. The bandgap energy increases with increasing x from 5.02 eV for $x = 0.07$ up to 5.85 eV for $x = 0.46$. The deduced change can be described by

$$E_g(x)(\text{eV}) = (4.85 \pm 0.01) + (2.14 \pm 0.03) \cdot x. \tag{2.2}$$

The growth rate exhibits a non-linear behavior with a maximum of 15.7 pm/pulse for $x = 0.07$ and a minimum of 12.0 pm/pulse for $x = 0.46$. A more detailed study can be found in Ref. 7.

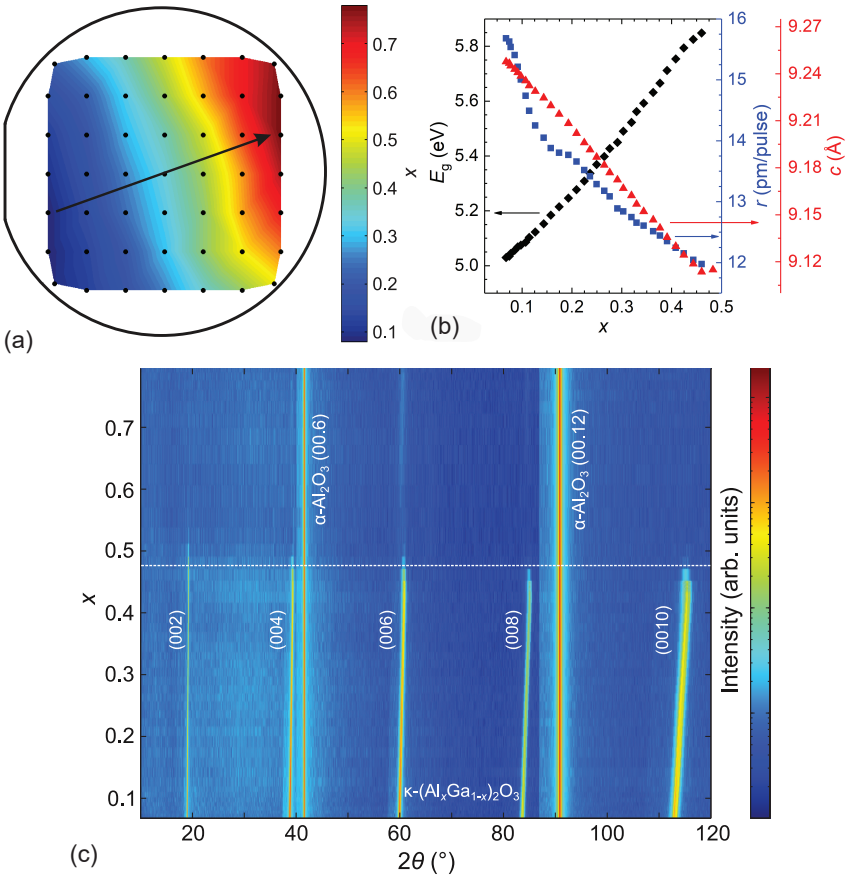

Figure 2.7: (a) False color plot of the Al-content of a $(Al_xGa_{1-x})_2O_3$ thin film grown on a 2 inch in diameter c-plane sapphire substrate. (b) c-lattice constant determined from XRD patterns as well as the band gap E_g and growth rate r obtained from spectroscopic ellipsometry measurements in dependence on x. (c) False color map of 55 single 2θ-ω measurements acquired along the gradient direction marked by black arrow in (a).

[1] M. Higashiwaki, K. Sasaki, A. Kuramata, T. Masui, S. Yamakoshi, Appl. Phys. Lett. **100**, 013504 (2012)
[2] H. von Wenckstern, Adv. Electron. Mater **3**, 1600350 (2017)
[3] R. Roy. V.G. Hill, E.F. Osborn, J. Am. Chem. Soc. **74**, 719–722 (1952)
[4] M. B. Maccioni, V. Fiorentini, Appl. Phys. Express **9**, 04102 (2016)
[5] H. von Wenckstern, Z. Zhang, F. Schmidt, J. Lenzner, H. Hochmuth and M. Grundmann, CrystEngComm **15**, 10020 (2013)

[6] M. Kneiß, A. Hassa, D. Splith, C. Sturm, H. von Wenckstern, T. Schultz, N. Koch, M. Grundmann, APL Materials **7**, 022516 (2019)
[7] Hassa C. Sturm, M. Kneiß, D. Splith, H. von Wenckstern, T. Schultz, N. Koch, M. Lorenz, M. Grundmann, APL Materials **8**, 021103 (2020)
[8] M. Kneiß, P. Storm, G. Benndorf, M. Grundmann and H. von Wenckstern, ACS Comb. Sci. **20**, 643-652 (2018)
[9] A. Hassa, H. von Wenckstern, L. Vines and M. Grundmann, ECS J. Solid State Sci. Technol. **8**, Q3217 (2019)
[10] P. Storm, M. Kneiß, A. Hassa, T. Schultz, D. Splith, H. von Wenckstern, N. Koch, M. Lorenz and M. Grundmann, APL Materials **7**, 111110 (2019)

2.5.2 Epitaxial κ-(Al,Ga)$_2$O$_3$ thin films and heterostructures by tin-assisted VCCS-PLD

P. Storm, M. Kneiß, A. Hassa, T. Schultz*, D. Splith, H. von Wenckstern, N. Koch*, M. Lorenz, M. Grundmann

*Department of Physics, Humboldt-Universität zu Berlin

The structural, morphological, and optical properties of phase-pure κ-$(Al_xGa_{1-x})_2O_3$ thin films on c-sapphire and STO(111):Nb substrates as well as on MgO(111) and κ-Ga_2O_3(001) templates were investigated as a function of the alloy composition. The thin films were grown by tin-assisted pulsed laser deposition utilizing elliptically segmented targets (VCCS-PLD) [1]. Initially, the growth window regarding growth pressure was determined. For all samples the κ-phase is (001) oriented and forms for growth pressures $p(O_2) < 0.02$ mbar. For higher pressures, the formation of the β-phase was observed. The aluminium content, incorporated into the thin film, was found to be strongly pressure dependent as shown in Fig. 2.8(a). For lower pressures, the transfer of aluminium is non-stoichiometric with up to twice the amount of aluminum incorporated compared to the aluminium content of the PLD-target. The observed behavior is similar to the PLD-growth of β-(Al,Ga)$_2$O$_3$ as discussed by Hassa *et al.* [2] and suggests a significant influence of the bond dissociation energy of the Ga-O and Al-O bonds and desorption of gallium on the growth of κ-(Al,Ga)$_2$O$_3$ by PLD.
For fixed growth conditions of 650°C and $p(O_2)$= 0.002 mbar the aluminium content was varied by changing the radial position r_{PLD} of the laser spot on an elliptically segmented target as presented in Fig. 2.8(b). Without an additional κ-Ga_2O_3 template the κ-$(Al_xGa_{1-x})_2O_3$ thin films crystallized phase-purely up to $x \approx 0.38$. For higher aluminum contents, XRD amorphous thin films were obtained. However, growth on a κ-Ga_2O_3 template led to a significant increase in the maximum quantity of incorporated aluminum without the occurrence of side phases up to $x \approx 0.65$. This result represents a significant increase compared to literature with values up to $x = 0.4$ [3]. The out-of- and in-plane lattice constants for all investigated thin films follow Vegard's law as demonstrated in Fig. 2.8(d). Epitaxial and relaxed growth was verified by XRD ϕ-scans and RSM measurements (Fig. 2.8(c)). The crystalline quality was estimated in terms of the FWHM of the κ-$(Al_xGa_{1-x})_2O_3$ (004) reflections in XRD 2θ-ω scans and did not reveal a systematic change for increasing aluminum contents with values close to

the resolution limit of the employed instrument. Reciprocal space map measurements revealed an increase in tilt mosaicity for increasing aluminum contents but still visible $K_{\alpha,1}$/ $K_{\alpha,2}$ splitting (Fig.2.8(c)), indicating a very high crystalline quality of corresponding thin films. The morphological properties were investigated by AFM. As depicted in Fig. 2.8(f), the surface consists of small grains with sizes between 50 nm to 200 nm. The root-mean square surface roughness ranged from 0.4 nm to 2 nm. To estimate the bandgap energies, transmission spectroscopy measurements were performed for samples deposited on c-sapphire. The obtained trend is presented in Fig. 2.8(e) with values up to 5.8 eV. For κ-$(Al_xGa_{1-x})_2O_3$ on κ-Ga_2O_3 template layers, energies up to 6.4 eV are expected for $x = 0.65$.

In conclusion, κ-$(Al_xGa_{1-x})_2O_3$ was grown by VCCS-PLD on various substrate and template materials. The thin films exhibit suitable crystalline and morphological properties for heterostructure device applications. The aluminum content was significantly increased for growth on κ-Ga_2O_3 template layers. The corresponding thin films also represent first heterostructures in the κ-$(Al_xGa_{1-x})_2O_3$/κ-Ga_2O_3 alloy system. A more detailed description can be found in Ref. [4].

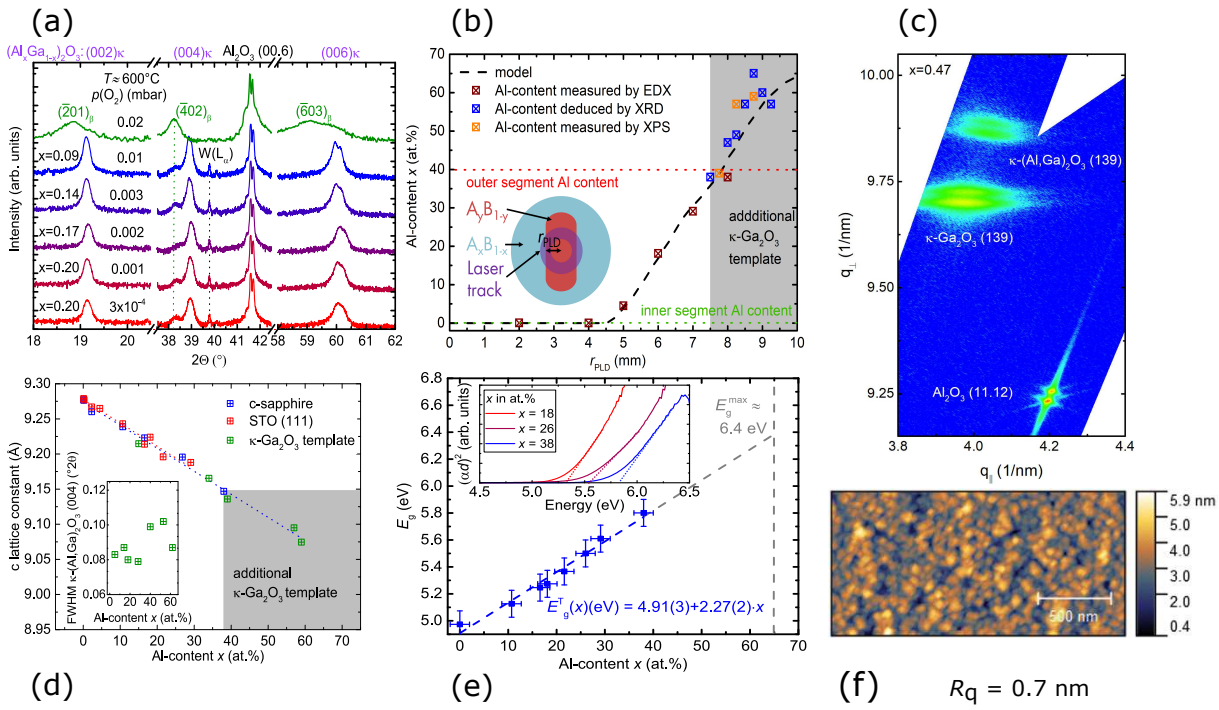

Figure 2.8: (a) XRD 2θ-ω scans of samples grown on c-sapphire at oxygen pressures as labeled. (b) Aluminum content in dependence on the radial position r_{PLD} of the PLD laser spot on the target. The compositions were determined by EDX, XPS, and XRD peak positions. (c) Reciprocal space map in the vicinity of the α-Al_2O_3 (11.12) reflection of a κ-$(Al_xGa_{1-x})_2O_3$ thin film on a κ-Ga_2O_3 template with $x = 0.47$. Epitaxial growth is confirmed by the occurrence of the thin film (139) reflections at the same ϕ-angle as the substrate reflection. (d) Evolution of the c-lattice constant and the FWHM of the (004) reflection in XRD 2θ-ω scans as shown in the inset. (e) Dependence of the bandgap estimated by transmission spectroscopy measurements for Al-contents up to $x = 0.38$. The dashed, gray line represents the extrapolation of the linear fit up to the highest aluminum content stabilized in κ-phase of $x = 0.65$. (f) Exemplary AFM surface scan of a κ-$(Al_{0.17}Ga_{0.83})_2O_3$ thin film on c-sapphire.

[1] M. Kneiß, P. Storm, G. Benndorf, M. Grundmann and H. von Wenckstern, ACS Comb. Sci. **20**, 643-652 (2018)
[2] A. Hassa, H. von Wenckstern, L. Vines and M. Grundmann, ECS J. Solid State Sci. Technol. **8**, Q3217-Q3220 (2019)
[3] D. Tahara, H. Nishinaka, S. Morimoto. and M. Yoshimoto, Appl. Phys. Lett. **112**, 152102 (2018)
[4] P. Storm, M. Kneiß, A. Hassa, T. Schultz, D. Splith, H. von Wenckstern, N. Koch, M. Lorenz and M. Grundmann, APL Materials **7**, 111110 (2019)

2.5.3 Epitaxial stabilization of single phase κ-$(In_xGa_{1-x})_2O_3$ thin films on c-sapphire and κ-Ga_2O_3(001) templates by tin-assisted VCCS-PLD

M. Kneiß, A. Hassa, D. Splith, C. Sturm, H. von Wenckstern, M. Lorenz, M. Grundmann

For the realization of devices based on the orthorhombic κ-phase of Ga_2O_3 such as quantum-well infrared photodetectors or high-electron mobility transistors, both the growth of high-quality heterostructures as well as bandgap engineering is a prerequisite. The latter is possible in this alloy system by incorporation of Al or In, leading to an increase and decrease of the bandgap, respectively [1–3]. Reports on the growth of heterostructures however are scarcely available so far.
In this study, we focused on the precise manipulation of the In-content in κ-$(In_xGa_{1-x})_2O_3$ thin films and the growth of high-quality κ-$(In_xGa_{1-x})_2O_3$/κ-Ga_2O_3 heterostructures as well as the solubility limit of In in this phase. For the variation of the In-content, we employed one elliptically-segmented and tin-doped Ga_2O_3/$(In_{0.4}Ga_{0.6})_2O_3$ target for pulsed laser deposition (PLD) schematically shown in Fig. 2.9 (a). The In-content was adjusted using the vertical continuous composition spread (VCCS) PLD technique by the radial position of the laser spot r on the target surface as described in previous reports [1, 4]. Tin is needed as surfactant to stabilize the κ-phase in PLD growth [8].
Fig. 2.9 (a) shows the In-content x of the κ-$(In_xGa_{1-x})_2O_3$ thin films grown on c-sapphire as well as the κ-$(In_xGa_{1-x})_2O_3$/κ-Ga_2O_3 heterostructures, where the κ-$(In_xGa_{1-x})_2O_3$ layer was deposited on a κ-Ga_2O_3 (001) growth template, as function of r. The In-content is monotonously increasing and follows an analytical model [4] for the expected In-content in VCCS PLD when stoichiometric transfer is considered (red dashed line). This indicates a suppression of the desorption of volatile In_2O and Ga_2O suboxides when the κ-phase is formed that typically cause sub stoichiometric incorporation of In for thin films in the monoclinic β-phase [9, 10].
Fig. 2.9 (b) shows X-ray diffraction (XRD) 2θ-ω scans of the κ-$(In_xGa_{1-x})_2O_3$/κ-Ga_2O_3 heterostructures. (001) oriented growth in the κ-phase for all samples is indicated from the XRD patterns. Additional XRD ϕ-scans were evaluated to confirm epitaxial growth of all layers with three rotational domains (not shown). Further, the κ-$(In_xGa_{1-x})_2O_3$ (004) reflection shifts to lower angular positions upon increase of x in agreement with an expected increase of the c-lattice constant. For $x \geq 0.30$, phase separation with occurrence of cubic In_2O_3 reflections takes place, similar to thin films on c-sapphire (not shown, see Ref. [1]) as well as previous reports [2]. The solubility limit can therefore not be enhanced by the growth of heterostructures in contrast to the κ-$(Al_xGa_{1-x})_2O_3$

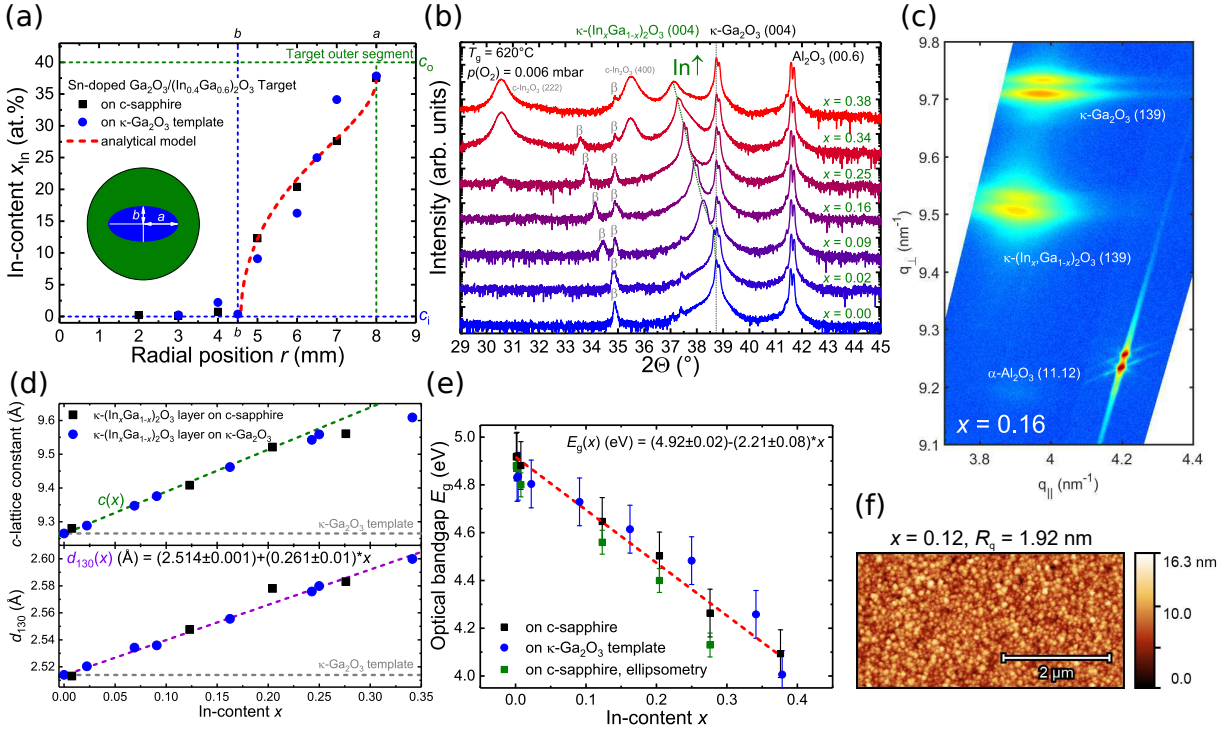

Figure 2.9: (a) In-content of all $(In_xGa_{1-x})_2O_3$ thin films investigated in this study as determined by energy dispersive X-ray spectroscopy measurements in dependence on the radial position of the laser spot r on the elliptically segmented target schematically shown in the inset. The red dashed line is the expected thin film composition from an analytical model for stoichiometric transfer from the PLD target in the thin film as described in Refs. [1, 4]. (b) XRD 2θ-ω scans of a series of $(In_xGa_{1-x})_2O_3$ thin films deposited via PLD on a κ-Ga_2O_3 template (cf. blue markers in (a)). c-In_2O_3 denotes reflections of a cubic In_2O_3 impurity phase. (c) RSM measurement around the κ-Ga_2O_3 (139) reflection of a κ-$(In_{0.16}Ga_{0.84})_2O_3$ thin film on a κ-Ga_2O_3 growth template. (d) Out-of-plane c-lattice parameter and in-plane d_{130} lattice plane distance as function of In-content x. The values were determined by the position of the (139) reflection in RSM measurements. Colored dashed lines are linear fits to the data, others indicate values of binary κ-Ga_2O_3. (e) Estimated optical bandgap for the investigated thin films versus In-content x. The red dashed line is a linear fit to the data. (f) Typical AFM image of a κ-$(In_{0.12}Ga_{0.88})_2O_3$ thin film on c-sapphire substrate. R_q denotes the root-mean-squared surface roughness.

alloy system, see section 2.5.2 and Ref. [3]. Nevertheless, the crystalline quality of the κ-$(In_xGa_{1-x})_2O_3$ layers was significantly enhanced by the growth on the templates since they show much lower broadening and higher intensity of respective reflections in XRD patterns.

Reciprocal space map (RSMs) measurements were evaluated to deeper investigate the growth of the κ-$(In_xGa_{1-x})_2O_3$ layers. The corresponding (139) reflections show low broadening for the heterostructures corroborating their high crystalline quality, see for example Fig. 2.9 (c) for a typical RSM.

From the positions of the (139) reflections, we could confirm relaxed growth of the alloy layers. And, using these, we further determined out-of-plane c-lattice parameters and in-plane d_{130} lattice plane distances as function of x, see Fig. 2.9 (d). Both show a linear increase with increasing x in agreement with Vegard's law.

To evaluate the limits for bandgap engineering, we determined the optical bandgaps

E_g of the alloy layers both by transmission spectroscopy and by spectroscopic ellipsometry. Fig. 2.9 (e) shows the estimated E_g as function of x. Similar to the lattice parameters, these show a linear dependence on x and are decreasing with increasing In-content. A tuning of E_g from 4.9 eV down to 4.2 eV is feasible within the phase pure regime of In-contents indicating a large potential for the application in quantum-well heterostructures. However, for these, smooth interfaces are needed as well.
Therefore, Fig. 2.9 (f) shows a typical atomic force microscopy (AFM) image of a single κ-$(In_{0.12}Ga_{0.88})_2O_3$ thin film on c-sapphire. Low surface roughnesses in the low nm regime are observed for phase pure growth sufficient for the application of this κ-phase alloy in heterostructures.
In conclusion, we were able to stabilize κ-$(In_xGa_{1-x})_2O_3$ thin films up to $x = 0.28$ phase pure, with high crystalline quality and precisely adjustable In-contents by VCCS-PLD. The results suggest a high potential of this phase for heterostructure device applications. Further, the κ-$(In_xGa_{1-x})_2O_3$ layers on κ-Ga_2O_3 growth templates are the first heterostructures for this alloy system. These results were published in Ref. [1], where also a more detailed investigation can be found.

[1] M. Kneiß, A. Hassa, D. Splith, C. Sturm, H. von Wenckstern, M. Lorenz and M. Grundmann, APL Materials **7**, 101102 (2019)
[2] A. Hassa, H. von Wenckstern, D. Splith, C. Sturm, M. Kneiß, V. Prozheeva and M. Grundmann, APL Materials **7**, 022525 (2019)
[3] P. Storm, M. Kneiß, A. Hassa, T. Schultz, D. Splith, H. von Wenckstern, N. Koch, M. Lorenz and M. Grundmann, APL Materials **7**, 111110 (2019)
[4] M. Kneiß, P. Storm, G. Benndorf, M. Grundmann and H. von Wenckstern, ACS Comb. Sci. **20**, 643-652 (2018)
[5] A. Hassa, H. von Wenckstern, L. Vines and M. Grundmann, ECS J. Solid State Sci. Technol. **8**, Q3217-Q3220 (2019)
[6] D. Tahara, H. Nishinaka, S. Morimoto. and M. Yoshimoto, Appl. Phys. Lett. **112**, 152102 (2018)
[7] P. Storm, M. Kneiß, A. Hassa, T. Schultz, D. Splith, H. von Wenckstern, N. Koch, M. Lorenz and M. Grundmann, APL Materials **7**, 111110 (2019)
[8] M. Kneiß, A. Hassa, D. Splith, C. Sturm, H. von Wenckstern, T. Schultz, N. Koch, M. Grundmann, APL Materials **7**, 022516 (2019)
[9] P. Vogt and O. Bierwagen, Appl. Phys. Lett. **108**, 072101 (2016)
[10] P. Vogt, O. Brandt, H. Riechert, J. Lähnemann and O. Bierwagen, Phys. Rev. Lett. **119**, 196001 (2017)

2.6 pn-heterojunction diodes with β-Ga_2O_3

D. Splith, P. Schlupp, H. von Wenckstern, M. Grundmann

β-Ga_2O_3 has promising material properties to be exploited in, e. g., high-power applications. However, due to its unipolarity and small predicted hole mobilities, bipolar homojunction diodes are unfeasible for this material. A valid alternative is the realization of heterojunction diodes, especially with other, p-type oxide semiconductors, as they also exhibit a high chemical stability as well as typically large bandgaps. Possible

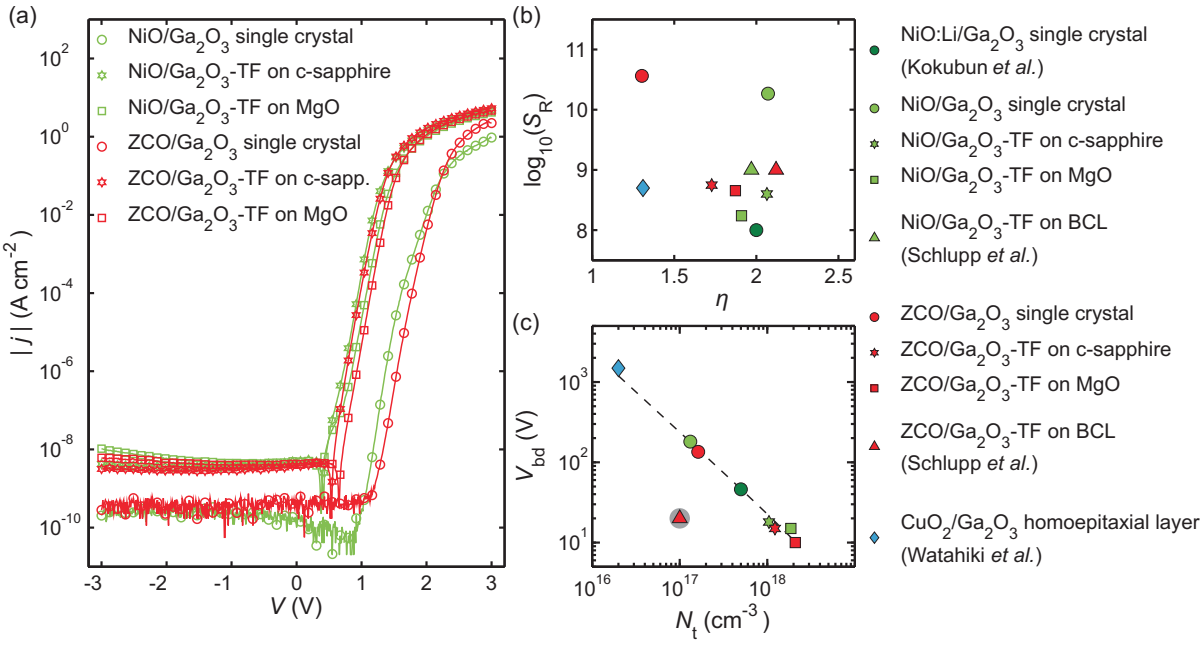

Figure 2.10: (a) Current density-voltage characteristics of NiO and ZCO pn-heterojunctions with β-Ga_2O_3 thin films (TF) and single crystals. (b) Rectification ratio in dependence on the ideality factor. For comparison, the values published by Kokubun *et al.*, Schlupp *et al.* and Watahiki *et al.* are also plotted. (c) Breakdown voltage in dependence on the net-doping density. All results lie on the same line in the log-log plot, except those of Schlupp *et al.*

candidates for such p-type oxide semiconductors are e. g. nickel oxide (NiO), cuprous oxide (Cu_2O) or zinc cobalt oxide (ZCO). Here, we report on pn-heterojunction diodes fabricated on β-Ga_2O_3 thin films grown by pulsed laser deposition (PLD) as well as on β-Ga_2O_3 single crystals and compare their characteristics to results published in literature.

Figure 2.10 (a) shows the current density-voltage characteristics of NiO and ZCO pn-heterojunction diodes with β-Ga_2O_3 single crystals as well as PLD-grown thin films on MgO and c-plane sapphire substrates. All diodes show high rectification ratios S_R of at least 8 orders of magnitude. The current in reverse direction can be attributed to the current charging the space charge region capacitance. This is also the reason for the lower reverse current of the heterojunction diodes on single crystals, since they have a lower doping density and therefore a lower space charge region capacitance than the thin films. In Fig. 2.10 (b), the rectification ratios are shown in dependence on the ideality factors η. Additional to the diodes in Fig. 2.10 (a), the following results published in literature are depicted: Li doped NiO junctions on β-Ga_2O_3 single crystals published by Kokubun *et al.* [1], NiO and ZCO junctions on PLD-grown β-Ga_2O_3 thin films with a ZnO back contact layer (BCL) published by Schlupp *et al.* [2] and Cu_2O junctions on homoepitaxial β-Ga_2O_3 grown by hydride vapour phase epitaxy published by Watahiki *et al.* [3]. Most of the ideality factors bunch around 2, indicating interface recombination as the dominating current transport mechanism [4]. Highest rectification was achieved for the heterojunction diodes on single crystals.

Since β-Ga_2O_3 is of interest for high-power applications, the breakdown of the heterojunction diodes was also investigated. In Fig. 2.10 (c), the breakdown voltage is plot-

ted in dependence on the net-doping density, which was determined from capacitance-voltage measurements. Here, the results from Kokubun *et al.*, Schlupp *et al.* and Watahiki *et al.* are included as well. Except for the results of Schlupp *et al.* that used vertical diodes with the thinnest drift layers of all diodes discussed here, all results lie on the same line in the log-log plot, which means that for all of them, about the same breakdown field was achieved. From a fit, the breakdown field can be determined to be 3 MV cm^{-1}, which is lower than the expected breakdown field of β-Ga_2O_3 of 8 MV cm^{-1}. However, no field-plate structure was used for all heterojunctions discussed here, therefore the field at the edge of the junctions might be significantly larger. More details on this study can be found in Ref. [5].

[1] Y. Kokubun, S. Kubo, S. Nakagomi, Appl. Phys. Express **9**, 091101 (2016)
[2] P. Schlupp, H. von Wenckstern and M. Grundmann, phys. status solidi (a) **216**, 1800729 (2019)
[3] T. Watahiki, Y. Yuda, A. Furukawa, M. Yamamuka, Y. Takiguchi and S. Miyajima, Appl. Phys. Lett. **111**, 222104 (2017)
[4] M. Grundmann, R. Karsthof and H. von Wenckstern, ACS Appl. Mater. Interfaces **6**, 14785 (2014)
[5] D. Splith *et al.*: Diodes 2. In: M. Higashiwaki, S. Fujita (eds): Gallium Oxide, Springer Series in Materials Science 293

2.7 High-quality Schottky barrier diodes on β-gallium oxide thin films on glass substrate

H. von Wenckstern, D. Splith, L. Thyen, S. Müller, A. Reinhardt, M. Grundmann

The ultra wide band gap material Ga_2O_3 has attracted enormous interested due to its potential applications in power electronics, deep-UV sensing or as visible- and solar-blind infrared detectors [1]. For these applications, highly rectifying Schottky barrier diodes (SBD) are essential. As a step towards low-cost deep-UV photo detectors we exploit properties of SBDs on Ga_2O_3 thin films on glass substrates and compare their current-voltage characteristics to similar SBDs on Ga_2O_3 bulk single crystals and on thin films grown heteroepitaxially on c-plane sapphire, respectively.

Structural, optical and electrical properties of monoclinic $\beta-Ga_2O_3$:Si were investigated. The thin films were grown by pulsed laser deposition on glass substrate for growth temperatures T_G between 20°C and 650°C and oxygen pressures p_{O_2} of 3×10^{-4} and 1×10^{-3} mbar, respectively. Further, the influence of low-temperature buffer layers, some of which were annealed ex-situ, on the thin film quality was evaluated [2].

Thin films grown on the substrate without buffer layer were X-ray amorphous if the growth temperature was below 510°C and exhibited an optical bandgap between 4.2 and 4.3 eV. Otherwise polycrystalline layers with optical bandgap of about 5.0 eV were obtained. For $T_G = 650$°C highest electrical conductivity of $\sigma = 2$ S/m was determined, the root mean square surface roughness of that film was $R_q = 4.0$ nm and hence this growth temperature was used for all subsequently studied $\beta-Ga_2O_3$:Si main layers. The introduction of a low-temperature grown and high-temperature annealed

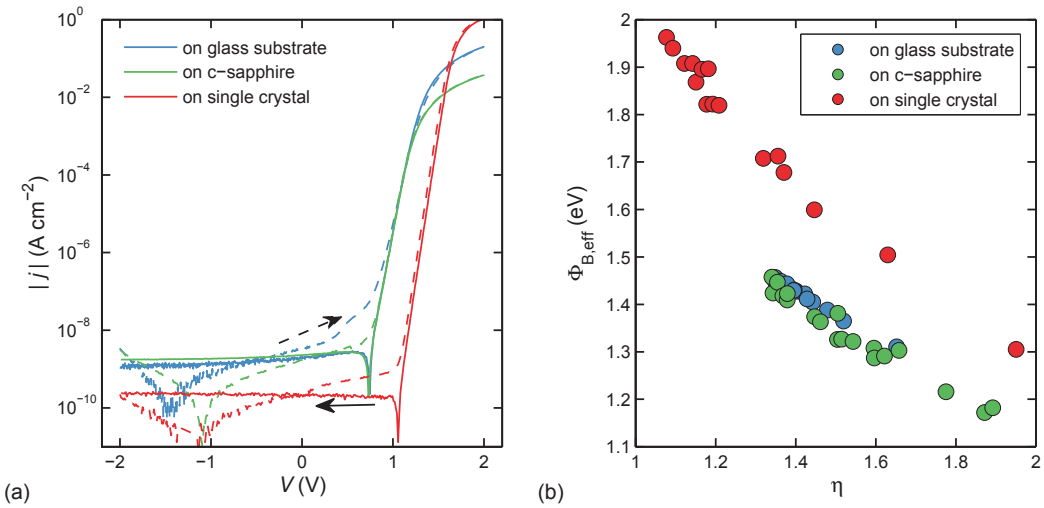

Figure 2.11: (a) Room temperature current density-voltage characteristics of PtO_x SBDs in heteroepitaxial β−Ga_2O_3:Si thin films and β−Ga_2O_3 bulk single crystals. (b) Effective barrier height versus ideality factor for arrays of SBDs on the samples shown in (a).

buffer layer leads to an increase of thin film conductivity. Promising thin film properties were obtained for buffer layer A: $T_G = 20°C$, $p_{O_2} = 3 \times 10^{-4}$ mbar and buffer layer B: $T_G = 400°C$, $p_{O_2} = 1 \times 10^{-3}$ mbar. The electrical conductivity of the β−Ga_2O_3 layers systematically increases if the buffer layers were thermally annealed prior to thin film deposition. However, the increase in conductivity is at least partially due to an increased grain size leading to higher R_q. The highest electrical conductivity of 890 S/m is achieved for a film on an annealed buffer layer A for $T_{ann} = 1100°C$. The surface roughness of this layer is $R_q = 18.4$ nm [2].

To evaluate the potential of β−Ga_2O_3:Si on glass for functional devices, PtO_x Schottky barrier diodes (SBD) were fabricated on layers on glass and on as-grown and annealed buffer layers A and B. All SBDs exhibited highly rectifying behavior. As expected, the on-resistance scales with the electrical conductivity of the main layer and is lowest for SBDs on buffer layer A that was annealed at 1100°C. Further, the leakage current density is correlated to the electrical conductivity and with that to the thin film surface roughness, such that SBDs on as-grown thin films on glass have lowest leakage current density. The ideality factor of the diodes is correlated to the surface roughness as well. For SBDs on buffer layers the ideality factors range between 1.3 and 3.5, for diodes on as-grown layers values between 1.3 and 1.7 are deduced. Finally, the effective barrier height is among the highest for these films. These results indicate that neither a buffer layer nor an annealing step is necessary to obtain highly rectifying SBDs with comparatively low ideality factor on β−Ga_2O_3:Si thin films on glass substrates. This is substantiated by comparing their current-voltage characteristics to diodes realized on heteroepitaxial thin films on Al_2O_3 and on bulk Ga_2O_3 single crystals as shown in fig. 2.11a). Further, the effective barrier height as well as the ideality factor of diodes fabricated on thin films on glass and Al_2O_3, respectively, are alike as depicted in fig. 2.11b). These results demonstrate that SBDs on Ga_2O_3 on glass substrates have the potential to be exploited in, e.g., deep-UV photo detectors [2].

[1] H. von Wenckstern, Adv. Electron. Mater. **3**, 1600350 (2017)
[2] S. Müller, L. Thyen, D. Splith, A. Reinhardt, H. von Wenckstern, M. Grundmann, ECS J. Solid State Sci. Techn. **8**, Q3126-Q3132 (2019)

2.8 Universal Relation for the Orientation of Dislocations from Prismatic Slip Systems in Hexagonal and Rhombohedral Strained Heterostructures

M. Grundmann

The strain relaxation in heteroepitaxial systems beyond the critical thickness can occur via misfit dislocations. In many cases, the dislocation lines arise from slip systems. In particular, for hexagonal wurtzite nitride heterostructures the basal-plane (*c*-plane) {0001} slip system has been found to enable plastic strain relaxation for growth on polar and semipolar orientations. In several cases, also the wurtzite prismatic slip systems on *m*-plane ($\{1\bar{1}00\}$ $1/3\langle 11\bar{2}0\rangle$) and *a*-plane ($\{11\bar{2}0\}$ $1/3\langle 1\bar{1}01\rangle$) have been found [1–4]. There are also similar slip systems in the rhombohedral (trigonal) corundum structure [5].

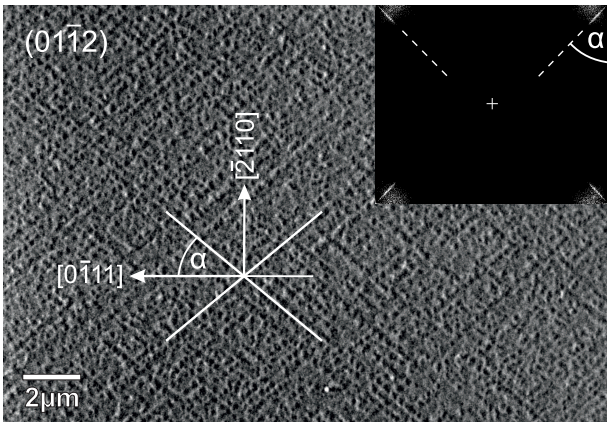

Figure 2.12: SEM image of (partially) relaxed $(Al_{0.47}Ga_{0.53})_2O_3$ epilayer on *r*-plane Al_2O_3. The inset is the Fourier transform of the image. The white solid (dashed) lines indicate the evaluated angle of the crosshatch pattern in the real space (Fourier) image. From the latter, $\alpha = 40.2(5)°$ is measured.

The anisotropic strain relaxation in corundum-phase α-$(Al,Ga)_2O_3/Al_2O_3$ heterostructures has been reported by us [6, 7]. In Fig. 2.12 we show as example the crosshatch pattern due to slip on the surface of a partially relaxed $(Al_{0.47}Ga_{0.53})_2O_3$ epilayer on (01.2) (*r*-plane) Al_2O_3, fabricated in our laboratory using pulsed laser deposition [7]. The angle α towards the projection of the *c*-direction in the interface plane has been measured to be $\alpha = 40.2(5)°$.

The orientation of the dislocation lines for epitaxial planes tilted against the *c*-axis in the *a*- and *m*-azimuth for prismatic glide systems in the *a*- or *m*-plane depend only

on the inclination angle against the c-axis via [8],

$$\alpha_a^m = \pm \arctan\left(\sqrt{3}\,\cos\theta\right) \tag{2.3}$$

$$\alpha_m^m = \pm \arctan\left(\cos\theta/\sqrt{3}\right) . \tag{2.4}$$

In this notation, the upper index denotes the azimuth, the lower index the glide plane, with $\alpha_m^a = \alpha_a^m$ and $\alpha_a^a = \alpha_m^m$. It is remarkable that the formulas depend only on the interface inclination angle θ, and thus are universal and material independent!

The dislocation angles for various systems reported in the literature are visualized in Fig. 2.13 and agree with the above formulas. Further details can be found in [8].

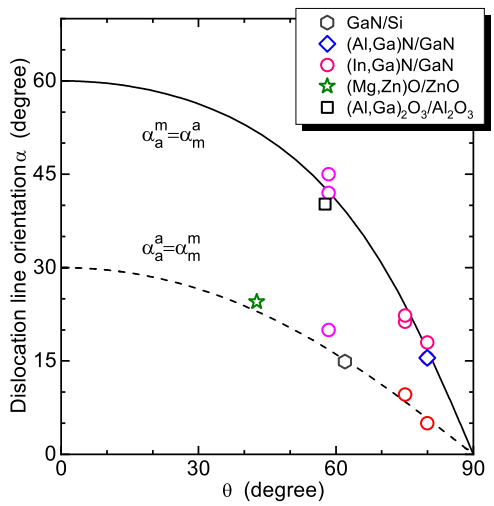

Figure 2.13: Dislocation line orientation angle α (versus the projected c-axis direction) for the a-plane (solid line) and the m-plane (dashed line) prismatic slip systems as a function of interface inclination angle θ together with various experimental data from heteroepitaxial systems as labeled.

[1] A.M. Smirnov, E.C. Young, V.E. Bougrov, J.S. Speck, A.E. Romanov, APL Mater. **4**, 016105:1–8 (2016)
[2] D.L. Becerra, Y. Zhao, S.H. Oh, C.D. Pynn, K. Fujito, S.P. DenBaars, S. Nakamura, Appl. Phys. Lett. **105**, 171196:1–4 (2014)
[3] M.T. Hardy, P.S. Hsu, F. Wu, I.L. Koslow, E.C. Young, S. Nakamura, A.E. Romanov, S.P. DenBaars, J.S. Speck, Appl. Phys. Lett. **100**, 202103:1–4 (2012)
[4] F. Wu, E.C. Young, I. Koslow, M.T. Hardy, P.S. Hsu, A.E. Romanov, S. Nakamura, S.P. DenBaars, J.S. Speck, Appl. Phys. Lett. **99**, 251909:1–4 (2011)
[5] J.D. Snow, A.H. Heuer, J. Amer. Ceram. Soc. **56**, 153–157 (1973)
[6] M. Lorenz, S. Hohenberger, E. Rose, M. Grundmann, Appl. Phys. Lett. **113**, 231902:1-5 (2018)
[7] M. Grundmann, M. Lorenz, APL Mater. **8**, 021108:1-14 (2020)
[8] M. Grundmann, Appl. Phys. Lett. **116**, 082104:1-3 (2020)

2.9 Band offsets of dielectric coatings on monoclinic $(In,Ga)_2O_3$ and $(Al,Ga)_2O_3$

H. von Wenckstern, M. Kneiß, C. Fares*, M. Tadjer†, F. Ren*, S. Pearton*, M. Grundmann

*Department of Chemical Engineering, University of Florida, Florida
†Department of Physics, Arizona State University, Tempe, Arizona

Monoclinic β-Ga_2O_3 and its ternary alloys $(In,Ga)_2O_3$ and $(Al,Ga)_2O_3$ have potential applications within next generation power electronics and solar-blind photodetectors resulting in significant recent scientific attention. The choice of dielectrics to be used within, e.g., metal-oxide-semiconductor junctions is crucial for optimizing their performance and durability. In collaboration with the University of Florida, band offsets of atomic-layer-deposited (ALD) Al_2O_3 and SiO_2 on monoclinic $(In,Ga)_2O_3$ and $(Al,Ga)_2O_3$ have been determined for various cation compositions [2, 3]. Further, the impact of annealing of the dielectrics was investigated [4, 5].

Ternary $(In,Ga)_2O_3$ and $(Al,Ga)_2O_3$ thin films with lateral composition spread were grown heteroepitaxially on MgO(100) by combinatorial pulsed laser deposition [1]. $(In_xGa_{1-x})_2O_3$ crystallized in monoclinic (cubic bibyite) crystal structure for $x < 0.3$ ($x > 0.75$); otherwise the sample was X-ray amorphous [2]. $(Al_yGa_{1-y})_2O_3$ crystallized in monoclinic (spinel γ) crystal structure for $x < 0.4$ ($x > 0.65$); in between, a mixture of both phases exists [3]. On both thin films, ALD layers were deposited at 200°C in remote oxygen plasma mode using trimethylaluminum or dimethylamino silane as precursors. Bandgaps of the dielectrics were determined by reflection electron energy loss spectroscopy. The bandgaps of the $(In_xGa_{1-x})_2O_3$ and $(Al_yGa_{1-y})_2O_3$ layers were obtained from X-ray photoelectron spectroscopy (XPS) energy loss measurements of the O1s peak. Valence band maxima and core level energies were measured by XPS for the dielectrics and the heteroepitaxial thin films. Then the difference of core level energies was obtained from heterojunctions of thin dielectric layers on the $(In_xGa_{1-x})_2O_3$ and $(Al_yGa_{1-y})_2O_3$ layers.

Figure 2.14 represents the experimentally determined valence and conduction band offsets of $(In_xGa_{1-x})_2O_3$ to $(Al_yGa_{1-y})_2O_3$ and SiO_2 and Al_2O_3, respectively. All investigated heterostructures are of type I. In the case of $(In_xGa_{1-x})_2O_3$, the valence band offset increases systematically and significantly with increasing indium content for both dielectrics. The decrease of the bandgap is due to the increase of the valence band energy and a somewhat smaller decrease of the conduction band minimum (CBM) with increasing x with respect to the the CBM of SiO_2 and Al_2O_3. In the case of $(Al_yGa_{1-y})_2O_3$, the valence band offset to SiO_2 and Al_2O_3 decreases only marginally. The increase of the bandgap is here mainly due to an increase of the conduction band energy as indicated by the decrease of the conduction band offset to both dielectrics.

In order to simulate the effect of the thermal budget during ohmic contact and device fabrication, the $Al_2O_3/(In,Ga)_2O_2$ and $SiO_2/(Al,Ga)_2O_3$ heterostructures were reinvestigated after annealing for 5 min at 600°C in nitrogen ambient [4, 5]. The changes of the valence band offsets (VBO) are depicted in fig. 2.15. For both ternary alloys the VBO decreases significantly during annealing and the change is stronger for higher In/Al contents. For the highest investigated In content the heterostructure changes to type II. Increased disorder is likely modifying the interface and its properties. Future

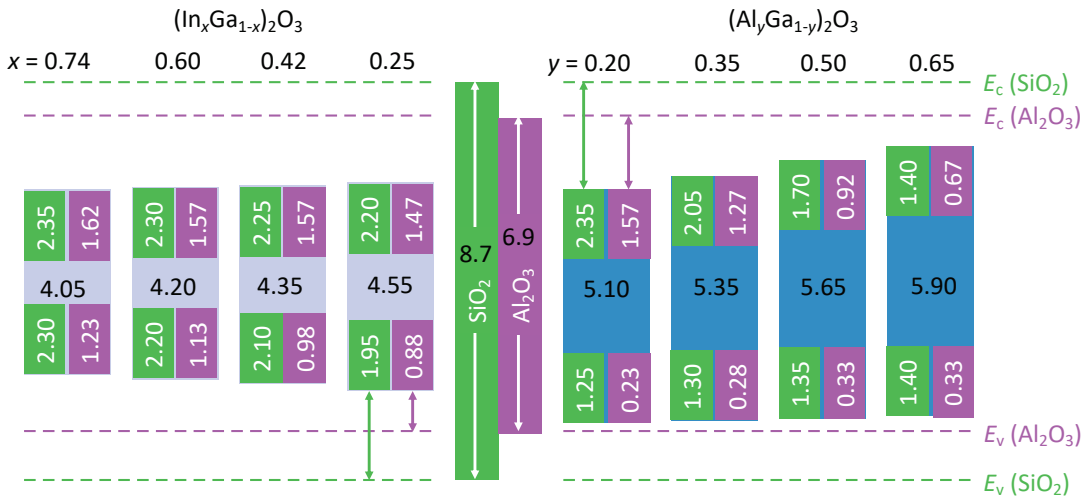

Figure 2.14: Schematic representation of conduction and valence band offsets of $(In_xGa_{1-x})_2O_3$ and $(Al_yGa_{1-y})_2O_3$ and SiO_2 and Al_2O_3, respectively. Values of band offsets are provided in white numbers, bandgap values are depicted in black. Numbers on green (purple) represent the offset with respect to SiO_2 (Al_2O_3).

tasks include the determination of interface state densities after annealing as well as radiation effects on band alignment.

[1] H. von Wenckstern, M. Kneiß, A. Hassa, P. Storm, D. Splith, M. Grundmann:physica status solidi (b), 1900626 (2019)
[2] C. Fares, M. Kneiß, H. von Wenckstern, M. Grundmann, M. Tadjer, F. Ren, E. Lambers, and S. J. Pearton, APL Mater. **7**, 071115 (2019)
[3] C. Fares, M. Kneiß, H. von Wenckstern, M. Tadjer, F. Ren, E. Lambers, M. Grundmann, and S. J. Pearton, ECS Journal of Solid State Science and Technology **8**, P351 (2019)
[4] C. Fares, Z. Islam, A. Haque, M. Kneiß, H. von Wenckstern, M. Grundmann, M. Tadjer, F. Ren, and S. J. Pearton, ECS Journal of Solid State Science and Technology **8**, P751 (2019)
[5] C. Fares, M. Xian, D. J. Smith, M. R. McCartney, M. Kneiß, H. von Wenckstern, M. Grundmann, M. Tadjer, F. Ren, and S. J. Pearton, J. Appl. Phys. **127**, 105701 (2020)

2.10 Optimized processing strategies for Schottky barriers on n-type semiconducting oxides

H. von Wenckstern, D. Splith, J. Michel*, J. Rombach*, A. Papadogianni†, T. Berthold*, M. Himmerlich*, O. Bierwagen†, S. Krischok*, M. Grundmann

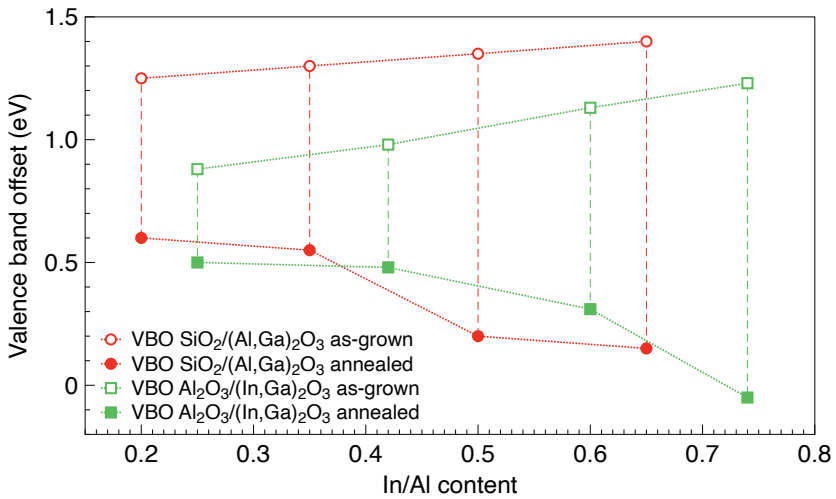

Figure 2.15: Valence band offsets for as-deposited and annealed $Al_2O_3/(In,Ga)_2O_2$ and $SiO_2/(Al,Ga)_2O_3$ heterostructures.

*Technische Universität Ilmenau, Institut für Mikro- und Nanotechnologien MacroNano
†Paul-Drude-Institut für Festkörperelektronik, Berlin

Semiconducting oxides tend to have an increased free electron density towards their surface. For CdO and In_2O_3 even two-dimensional surface electron accumulation layers (SEAL) were observed. The fabrication of Schottky barrier diodes (SBDs) with relevant current rectification is not possible on such surfaces without adequate pre-treatment and an optimized deposition process for the contact metal. In collaboration with the Universtät Ilmenau and the Paul-Drude-Institut für Festkörperphysik, Berlin, the electronic surface properties of as-grown and oxygen plasma treated surfaces of In_2O_3 thin films grown by molecular beam epitaxy on c-plane sapphire substrates were investigated. Further, the barrier height (BH) of Pt Schottky contacts deposited by evaporation or sputtering were determined by X-ray photoelectron spectroscopy (XPS) and room temperature current-voltage measurements [1]. The SEAL layer, present at the as-grown In_2O_3 surfaces, can be removed by oxygen plasma processing (PLOX) leading to an increase of the In_3O_3 work function. XPS measurements reveal that Pt forms a Schottky barrier on oxygen plasma treated surfaces independent of the deposition method, whereas for as-grown surfaces notable BH was observed only for reactively sputtered SBDs. Figure 2.16 summarizes values of BH determined by XPS and IV measurements for the differently deposited Pt layers on as-grown and oxygen plasma treated surfaces. In contrast to XPS, IV measurements only reveal current rectification for reactively sputtered Pt contacts and hence only for those a non-zero BH can be deduced by fitting the forward current of the diode. The in parts significant deviations of the XPS BH and the BH obtained from IV characteristics are traced back to the rather high free electron concentration of the investigated thin films, making thermionic field emission the dominating transport process for evaporated and inertly sputtered contacts. For reactively sputtered contacts this is strongly reduced and thermionic emission is governing electron transport. Highest current rectification up to six orders of magnitude is observed for reactively sputtered contacts on oxygen plasma treated surfaces. We further demonstrated that an additional and final oxygen plasma

treatment of entire SBDs leads to further reduction of the reverse current and increase of the IV BH.

Figure 2.16: Schematic representation of Schottky barrier heights determined by XPS (blue) and current-voltage measurements (green) for e-beam evaporated, inertly sputtered and reactively sputtered platinum on In_2O_3 thin films on c-plane sapphire.

The optimal processing strategy for Schottky barrier diodes on n-type semiconducting oxides is: i) removal of surface electron accumulation by oxygen plasma treatment, ii) reactive sputtering of the Schottky contact metal and iii) additional oxygen plasma treatment of the entire Schottky barrier diode.

[1] J. Michel, D. Splith, J. Rombach, A. Papadogianni, T. Berthold, S. Krischok, M. Grundmann, O. Bierwagen, H. von Wenckstern, and M. Himmerlich, ACS Appl. Mater. Interfaces **11**, 27073 (2019)

2.11 Increased breakdown field and improved interfacial roughness in $BaTiO_3$-$BiFeO_3$ multilayers via eclipse-PLD

S. Hohenberger, M. Lorenz

The study of magnetoelectric (ME) room temperature multiferroics, a rare class of materials that combines coupled ferroelectric and magnetic properties, is highly dependent on high quality samples [1]. The archetype intrinsic multiferroic bismuth ferrite ($BiFeO_3$, BFO) is a canted antiferromagnet that produces a weak net magnetic moment only in epitaxial thin film form, which leads to a magnetoelectric coupling coefficient of ca. 6 $Vcm^{-1}Oe^{-1}$ [1, 2]. One major experimental issue when working with BFO is leakage current in ferroelectric measurements as well as destructive breakdown at fields lower than the coercive field of the BFO films [3]. Both effects are an intrinsic

property of BFO, but also linked to crystal defects such as oxygen vacancies and dislocation density within the films. We have recently published a review on the topic of epitaxial multilayers of barium titanate ($BaTiO_3$, BTO) and BFO in [4]. The interlayers of BTO are an effective way of mitigating the intrinsic leakage current of BFO, as depicted in Fig. 1a). Depicted are the DC leakage current densities of capacitor structures deposited on Nb-doped strontium titanate ($SrTiO_3$, NSTO) with sputter-deposited Pt top contacts. The leakage current density at -5 V and +5 V is decreased by one and close to three orders of magnitude, respectively, when comparing a BFO single layer and a conventional BTO-BFO multilayer. Both films were deposited under identical conditions using conventional pulsed laser deposition (PLD), for details see [2]. The asymmetry in the leakage current density curves stems from the asymmetric electrode design.

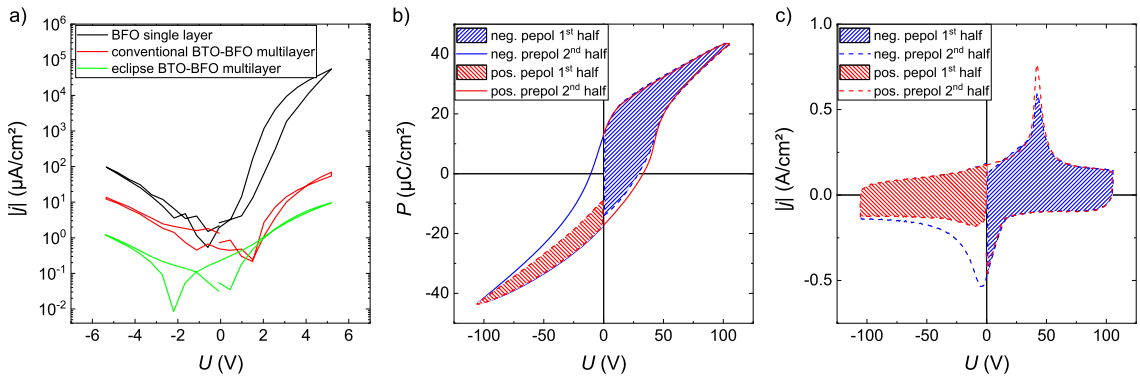

Figure 2.17: (a) DC leakage current density measurements of a BFO single layer, a conventionally grown multilayer and a eclipse PLD multilayer; **(b)** $P(U)$ and **(c)** $j(U)$ loops of a $15 \times [(BaTiO_3)_{20\ nm}$ - $(BiFeO_3)_{17\ nm}]$ eclipse PLD multilayer.

However, these conventionally deposited BTO-BFO multilayers suffer from breakdown fields of ca. 0.6 MV/cm at 1 kHz measurement frequency and considerably lower fields in DC measurements. If a field above the breakdown field is applied, BFO decomposes exothermically into Bi_2O_3 and Fe_3O_4 [5]. As the coercive field of such multilayers lies in the same order of magnitude, it is generally nor possible to record fully saturated ferroelectric hysteresis loops. Transmission electron microscopy (TEM) measurements of conventionally grown BTO-BFO multilayers reveal a fair amount of defect-related strain contrast and interface roughness in the nanometer range [2]. Furthermore, films deposited with conventional PLD show large droplet densities of 20-100 particles/100 μm, as determined by optical microscopy. Droplets is the name given to macroscopic particles that are generated as a byproduct of the laser ablation process, which can easily reach the size of the total film diameter. Such a droplet will not necessarily have the same stoichiometry as the deposited film and can cause a short in electrical measurements due to increased conductivity.

Recently, we have deposited BTO-BFO multilayers with a advanced PLD technique called eclipse-PLD. A shadow mask is placed between the ablation target and the substrate, thereby blocking the physical path of high energetic ablation species and macroscopic particles. The resulting films show drastically reduced particle densities of 0.1-10 particles/100 μm. Fig. 2a) shows a TEM cross section of the last four layers

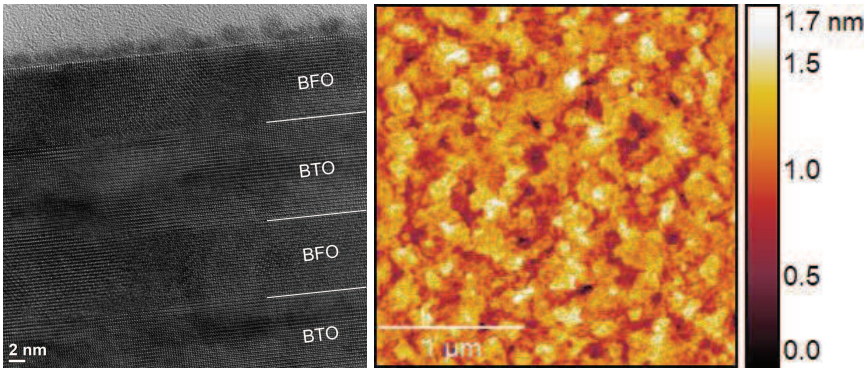

Figure 2.18: (a) TEM crossectional image and **(b)** topographical AFM image of a 15 × $[(BaTiO_3)_{10\ nm}$ - $(BiFeO_3)_{10\ nm}]$ multilayer deposited with eclipse PLD.

of a BTO-BFO multilayer with 20 nm double layer thickness, repeated 15× to yield a total layer thickness of ca. 300 nm. As can be seen, the interface and surface roughness are in the range of only one unit cell and strain contrast is only minimal. Fig. 2b) additionally shows a surface scanning probe microscopy image, confirming the unit-cell stepped surface morphology found in TEM measurements (R_{ms} roughness of 0.19 nm in a $10 \times 10 \mu m^2$ area). This relates to a highly ordered and defect-deficient crystal growth. As shown in Fig. 1a), the leakage current density in eclipse-PLD multilayers is decreased by a further order of magnitude when compared to the films derived by conventional PLD technique. The average breakdown field of eclipse-PLD BTO-BFO multilayers is notably increased to on average 3.2 MV/cm, which allows for fully saturated ferroelectric hysteresis measurements, as shown in Fig. 1b) and 1c). The presented polarization- (a)) and current-voltage (b)) curves were measured at 1 kHz at a maximum voltage of 100 V, which equates to a field of 3.4 MV/cm. The measurements are performed in two steps of triangular voltage pulses following a positive and negative pre-polarization pulse with a relaxation time of 1 s. Hence the respective first halves of the measurements contain information about the relaxation following the pre-polarization pulses. It is evident that a so-called imprint field exists, which shifts the entire curves towards positive voltages. This is a common feature in all of our BTO-BFO multilayers [2, 4, 6]. As Fig. 2c) shows, the negative switching peak is absent only following the positive pre-polarization, i.e. the ferroelectric self-biases towards a negative polarization state in zero applied electric field.

It is only by means of progressively enhanced sample quality such as gained from the application of eclipse-PLD it is possible to delve deeper into the understanding of the enhanced magnetoelectric coupling in BTO-BFO multilayers. We recently found ME coupling coefficients of up to 480 V/cmOe [6] in samples that were not previously electrically polarized, which can be in part facilitated by the above demonstrated self-biasing effect. We are furthermore conducting voltage and magnetic field dependent polarized neutron reflectometry measurements in early 2020 at the NREX reflectometer at the research neutron source FRM II. This measurement type benefits profoundly from minimized interface roughness and requires the destruction-free application of large electric fields.

[1] J. Wang *et al.*, *Science*, **299** (5613), 1719-1722 (2003)

[2] S. Hohenberger *et al.*, *J. Phys. D: Appl. Phys.* **51**, 184002 (2018)
[3] W. Eerenstein *et al.*, *Philos. Mag. Lett.* **3-4**, 249-257 (2007)
[4] S. Hohenberger *et. al.*, *Phys. Stat. Sol. B* **1900613** (2020)
[5] X. Lou *et. al.*, *Appl. Phys. Lett.* **26**, 90 (2007)
[6] S. Hohenberger *et. al.*, *Materials* **13 (1)**, 197 (2020)

2.12 Raman tensor determination of uniaxial materials

R. Hildebrandt, C. Sturm, M. Wieneke*, A. Dadgar*, M. Grundmann

*Otto-von-Guericke-Universität Magdeburg, Institute for Physics, Universitätsplatz 2, 39106 Magdeburg, Germany

Non-destructive characterization techniques are of high interest for applications in research and industry. Raman scattering is a common technique used to characterize materials of interest, such as high band-gap semiconductors, by applying polarized light. For anisotropic materials, the polarization of light changes during the propagation through the crystal. For uniaxial crystals, this birefringence is considered in the standard Raman scattering formalism by introducing an additional phase ξ' to the Raman tensor elements [1]. The magnitude of this phase is determined by the penetration depth profile and the birefringence of the material. By means of this extension, we were able to model the Raman scattering intensity depending on the polarization of incident light [2].

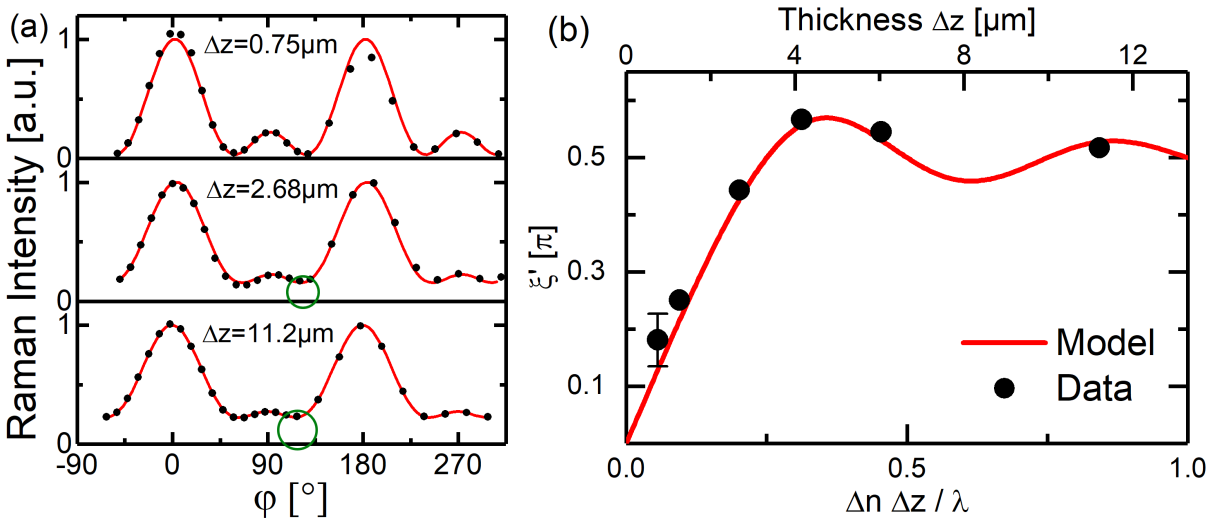

Figure 2.19: (a) Polarized Raman intensity of the A_1 mode as a function of the angle of incidence for films of different thickness. Shown are experimental data (black dots) and theoretical approximation (red line) in the parallel scattering configuration. While for the thinnest film the offset of the minimum is almost zero, the offset has to be considered for films with higher thickness (green circles). This offset effect can be described by the apparent angle parameter ξ'. (b) Apparent angle as function of the film thickness as well as the fit parameter values, deduced from measurements.

By using a-plane GaN films with thicknesses in the range of 0.7-11.2μm, the Raman intensity was measured as a function of the incident as well as the scattered polarization and the apparent angle ξ' was investigated in dependence on the film thickness. The A_1 peak intensity was extracted from the polarized Raman spectra as the polarization direction of the incident light was varied via the angle φ (Fig. 2.19(a)). The apparent angle ξ' was determined by the theoretical description of the angle-resolved polarized Raman spectra and plotted with the model prediction as a function of the film thickness (Fig. 2.19(b)). The theoretical model provides a reasonable approximation to the measured Raman spectra and validates the theoretical description of uniaxial media.

[1] C. Kranert, C. Sturm, R. Schmidt-Grund, and M. Grundmann, Phys. Rev. Lett. **116**, 127401 (2016), doi:10.1103/PhysRevLett.116.127401
[2] C. Kranert, C. Sturm, R. Schmidt-Grund, and M. Grundmann, Sci. Rep. **6**, 35964 (2016), doi:10.1038/srep35964

2.13 Exceptional points in anisotropic layered photonic structures

E. Krüger, S. Henn, C. Sturm, R. Schmidt-Grund*, M. Grundmann

*Technische Universität Ilmenau, Institut für Physik, Ilmenau, Germany

Exceptional points (EPs) correspond to non-Hermitian degeneracies and represent topological charges, due to the Riemann-sheet structure of two energy levels that have a complex square dependency as depicted in Fig.2.20 [1]. This renders EP very interesting in the context of topologically non-trivial photonic systems due to their possible technological applications, such as fast on-chip optical data transfer devices or the realization of optical isolators. Such EPs can occur in the momentum space of a photonic system and therefore represent directions around which the eigenmodes of the photonic system coalesce in the real space, thereby yielding a degeneracy in energy, broadening and polarization.

Similarly, a notable phenomenon is the splitting of both classic optic axes within an optically biaxial material into two singular optic axes, which occurs in the absorption spectral range [2, 3]. The eigenmodes are either single left- or right-handed circular polarized along such singular optic axes, thus representing Voigt EPs in the energy-momentum space. However, the occurrence of EPs in bulk crystals requires polarization dependent absorption or gain, which are intrinsic material properties and therefore are difficult to modify. This limitation can be overcome by considering planar layered structures, such as conventional planar microcavities. In the transparent regime, the dissipation is caused by a photon loss at the interfaces, rather than material absorption as in the former case. This enables manipulation of the occurrence and the direction of EPs in the momentum space by varying the degrees of freedom in such systems [4, 5].

2.13.1 Voigt exceptional points in a planar microcavity and thin films

Here, we report on a microcavity, based on an m-plane oriented ZnO, that assumes a non-Hermitian system and therefore mimics the behavior of natural Voigt points in

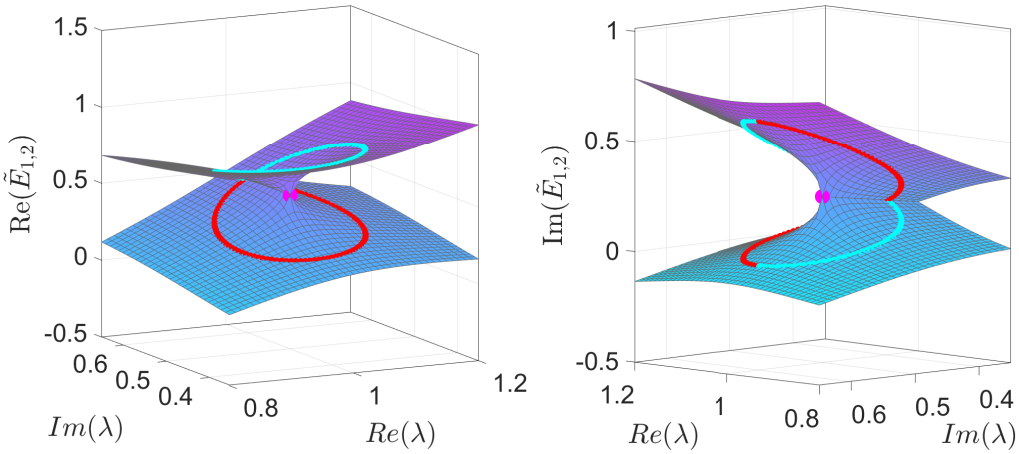

Figure 2.20: Exemplary complex-square-root topology $\tilde{E}_{1,2} \propto \pm\sqrt{(\lambda-\lambda_1)(\lambda-\lambda_2)}$ for the 'interaction parameter' $\lambda \in \mathbb{C}$. Continuously encircling the EP (pink dot) in λ-space once (red and blue trajectories) yields an exchange of the imaginary parts of $E_{1,2}$ and thus of the two energy levels.

an anisotropic bulk crystal [5]. The bottom distributed Bragg reflector (DBR) consists of 16 pairs of ZnO and $Mg_{0.29}Zn_{0.71}O$ as well as a cavity layer, which were fabricated by means of molecular beam epitaxy on an m-plane oriented ZnO substrate [6], such that all ZnO and $Mg_{0.29}Zn_{0.71}O$ layers were oriented in the m-plane. The top-DBR was prepared non-epitaxially by pulsed laser deposition and consists of 6 pairs of Al_2O_3 and Y-stabilized ZrO_2 (YSZ). The thickness of the cavity layer is tuned to 9/8 of the central wavelength of the DBR ($\approx$ 400 nm) and corresponds to a cavity photon mode energy of about 3 eV, thereby enhancing functionality in the transparent spectral range of the aforementioned materials.

Polarization-resolved reflection experiments at angles of incidence θ $(10-75)^\circ$ and sample azimuth angles ϕ $(0-360)^\circ$ were conducted to map the momentum space of the radiative cavity modes. In order to obtain the optical mode energies and their degeneracies in the two-dimensional momentum space, an effective Hamiltonian model was developed to approximate the obtained Stokes parameter spectra for each configuration (θ, ϕ) in a spectral range of 100 meV around the cavity modes. Fig.2.21 shows the eigenvalues of the fitted Hamiltonian for the entire momentum space as well as their differences. Four Voigt points are found at approximately $(\pm k_x, \pm k_y) \approx (\pm 4\,\mu\mathrm{m}^{-1}, \pm 8\,\mu\mathrm{m}^{-1})$, where the mode energy and broadening degenerate simultaneously. The complex-square-root topology of the mode-energy surface was verified by tracking the mode energies along a path in the momentum space that encircles an EP. One round-trip yields a continuous exchange of the two modes, namely the energetically higher (spectrally narrower) mode is converted to an energetically lower (broader) mode and vice versa. Under quasistatic encirclement, this exchange establishes the existence of an EP in the investigated system. Furthermore, due to the optical anisotropy of the microcavity, the polarization dependence of the dissipation along the energy degeneracy path between two EPs is reproduced by the fitted Hamiltonian approximation, thereby confirming that each diabolical point indeed splits into a pair of EPs.

The photonic modes in anisotropic microcavities can be modeled numerically by

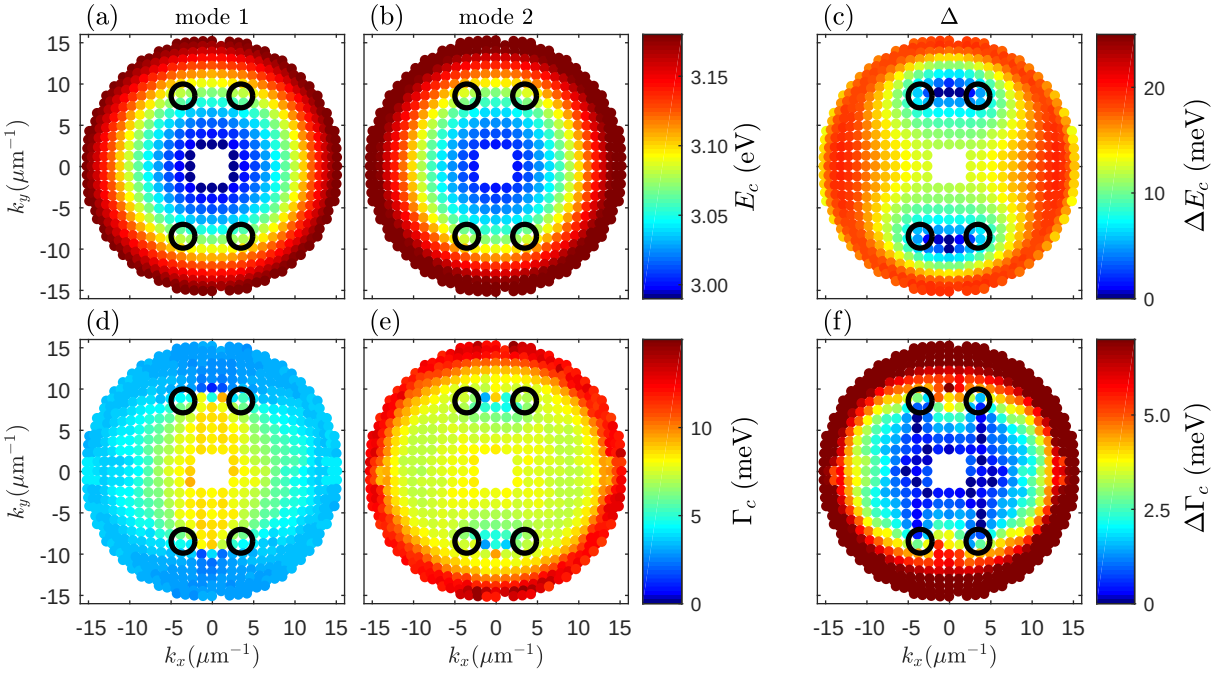

Figure 2.21: Complex mode energies $\tilde{E}_{1,2} = E_{1,2} - i\Gamma_{1,2}$ in dependence on the in-plane wave vector $\vec{k}_{\|}$, derived from the effective Hamiltonian [5]. Energies of mode 1 (a) as well as mode 2 (b) and their difference (c). Broadening of mode 1 (d) as well as mode 2 (e) and their difference (f). Modes are sorted such that $E_1 \leq E_2$. The positions of four EPs, where the mode energy and broadening degenerate simultaneously, are marked by black circles.

a transfer-matrix approach based on the Maxwell's theory, where the complex mode energies are found as the poles of the resulting scatter matrix for a given momentum and orientation of the sample. The characteristics of such Fabry-Pérot-type resonances in microcavities carry over to the thin film systems (in the limit $N_{DBR} \to 0$), representing simple layer thickness oscillations. Therefore, a straight-forward adaptation of the transfer-matrix formalism yields predictions for the occurrence of EPs in an anisotropic thin film system (Fig.2.22). The materials, chosen for this purpose, were the m-plane oriented ZnO and a-plane oriented GaN. The mode coalescence and associated mode exchange behavior upon encircling an EP in the momentum space were confirmed.

The appealing reduction of both cost and complexity of these systems, as compared to the microcavities, is counterbalanced by the enhanced broadening of the photonic modes, thereby leading to a large spectral overlap. However, using complex Lorentzian oscillators to describe the mode line-shape, eventually leads to an inaccurate description of the measured Stokes parameter spectra and thus hinders the efforts to experimentally observe the EPs in a thin film system.

2.13.2 Empirical observation of EPs in microcavities based on Mueller matrix symmetries

The inherent difficulty for experimental observation of complex-valued energies serves as a motivation for an alternative approach to investigate the occurrence of EPs. In symmetric anisotropic ZnO-based microcavity, the Mueller matrix (MM) behavior was

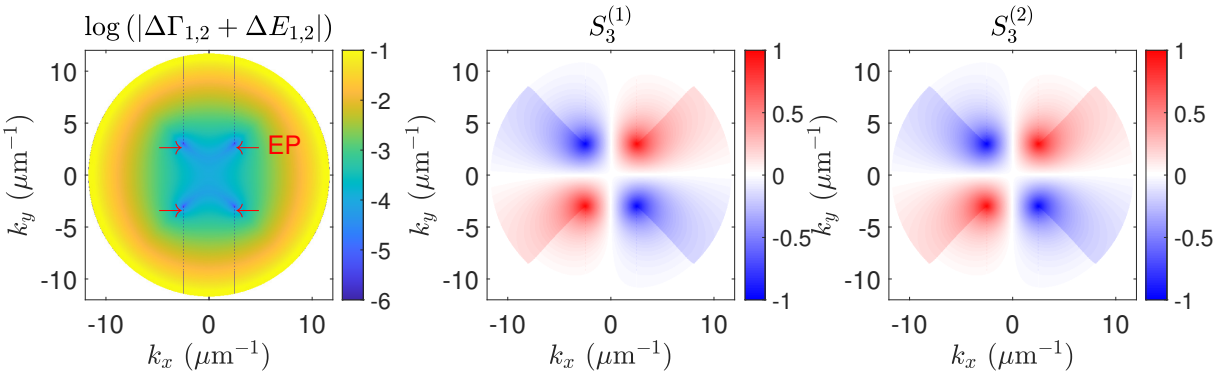

Figure 2.22: Differences of the complex mode energies $\tilde{E}_{1,2} = E_{1,2} - i\Gamma_{1,2}$, as a function of the in-plane momentum for a 500 nm ZnO thin film (left). The four EPs, where these differences are (nearly) zero, are indicated by the arrows. The S_3 Stokes components, describing the degree of circular polarization, are shown for Mode 1 (center) and Mode 2 (right). The degree of circular polarization is ≈ 100% at the EP and equal for both modes, such that the modes are coalesced.

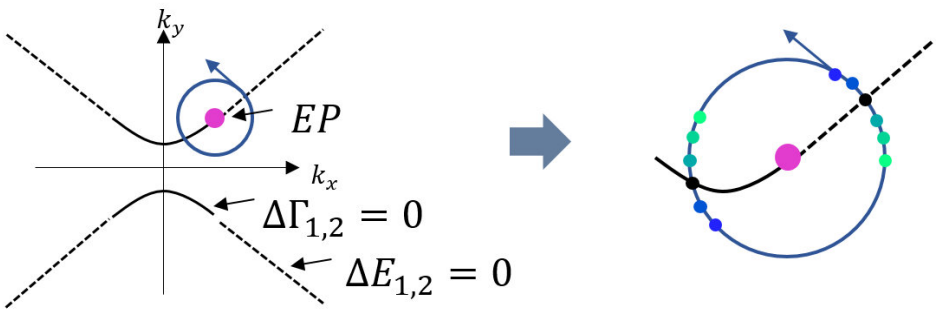

Figure 2.23: Schematic representation of the encircling of an EP in the $k_{\|}$-space. Mueller matrix spectra are computed along the dark blue circular trajectory and analyzed in the vicinity of the degeneracy crossings (black dots).

analyzed along a closed trajectory around an EP in the parameter space of the system, namely the in-plane component of the wave vector. As mentioned above, the topological nature of the system yields an exchange of the two photonic modes, which is visible in the measured MM spectra. In this case, the trajectory crosses two degeneracies at different $k_{\|}$, namely the energy ($\Delta E_{1,2} = 0$) and the broadening ($\Delta\Gamma_{1,2} = 0$), Fig.2.23.

While the MM spectra clearly indicate the crossing of the degeneracy, differentiating between the two degeneracies is crucial, since the crossing of both is a necessary condition for an EP within the trajectory. It was possible to distinguish between $\Delta E_{1,2} = 0$ and $\Delta\Gamma_{1,2} = 0$ using the symmetry properties of the MM elements around the degeneracies. While the spectral positions of the two modes (peaks) are identical in the first case, they are different in the latter. This allows to identify two distinct peaks for the two modes that follow the reflection symmetry in the MM spectra, Fig.2.24.

[1] W. D. Heiss, J. Phys. A: Math. Theor. **45**, 444016 (2012), doi:10.1088/1751-8113/45/44/444016
[2] C. Sturm, and M. Grundmann, Phys. Rev. A **93**, 053839 (2016), doi:10.1103/PhysRevA.93.053839
[3] W. Voigt, Ann. Phys. **314**, 367 (1902), doi:10.1002/andp.19023141006

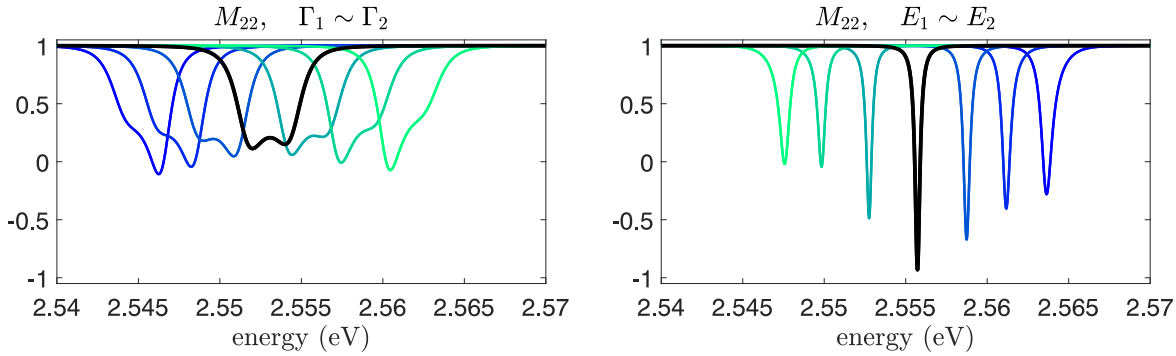

Figure 2.24: M_{22} spectra around $\Delta\Gamma_{1,2} = 0$ (left) and $\Delta E_{1,2} = 0$ (right). Green curves move towards and blue curves move away from the degeneracy. The two distinct peaks are visible in the left image, even at the degeneracy.

[4] S. Richter *et al.*, Phys. Rev. A **95**, 023836 (2017), doi:10.1103/PhysRevA.95.023836
[5] S. Richter *et al.*, Phys. Rev. Lett. **123**, 227401 (2019), doi:10.1103/PhysRevLett.123.227401
[6] J. Zuñiga-Perez *et al.*, Appl. Phys. Lett. **108**, 251904 (2015), doi:10.1063/1.4954796

2.14 Femtosecond time-resolved imaging of the dielectric function of ZnO

O. Herrfurth, T. Pflug[*†], M. Olbrich[*], M. Grundmann, A. Horn[*], R. Schmidt-Grund[‡]

[*]Laserinstitut Hochschule Mittweida, Mittweida, Germany
[†]Technische Universität Chemnitz, Institut für Physik, Chemnitz, Germany
[‡]Technische Universität Ilmenau, Institut für Physik, Ilmenau, Germany

Transient optical properties, represented by the dielectectric function (DF) following ultrafast laser excitation, can be obtained using time-resolved spectroscopic ellipsoemtry (tSE) [1, 2]. Laser excitation of the electronic system of a semiconductor induces also spatio-temporal dynamics of the DF, which can be studied by time-resolved ellipsometry in imaging mode [3, 4]. Pump-probe imaging ellipsometry (tIE) measurements at the corresponding setup at Laserinstitut Hochschule Mittweida are performed as previously described [3] and the experimental parameters are listed in Ref. [4]. A c-plane oriented ZnO thin film 30 nm grown by pulsed-laser deposition on a fused silica substrate is used. The substrate is transparent for the pump wavelength (266 nm) such that the pump laser pulses generate an electron-hole-pair density of $\approx 5 \times 10^{20}$ cm^3 in the ZnO film only. The DF is computed from a transfer-matrix model [5] and agrees very well with recent results, obtained by time-resolved spectroscopic ellipsometry (tSE) on ZnO [1].

Cross sections of the difference in ε_1, with respect to their reference value without excitation ($\Delta\varepsilon_1$), are visualized in Fig. 2.25 for selected time delays Δt. The cross section of the imaginary component of the DF $\Delta\varepsilon_2$ corresponds to a Gaussian distribution within the irradiated area, which exhibits a maximum value for $\Delta t \approx 400$ fs and subsequently decreases. The cross section, corresponding to the real part of the DF $\Delta\varepsilon_1$, is found to

be broader for all Δt than the cross sections of the imaginary part of the DF $\Delta\varepsilon_2$. Furthermore, a plateau, respectively a local maximum, is observed in $\Delta\varepsilon_1$ for $\Delta t > 600$ fs, which indicates a formation of a ring in the image. The observations are explained by

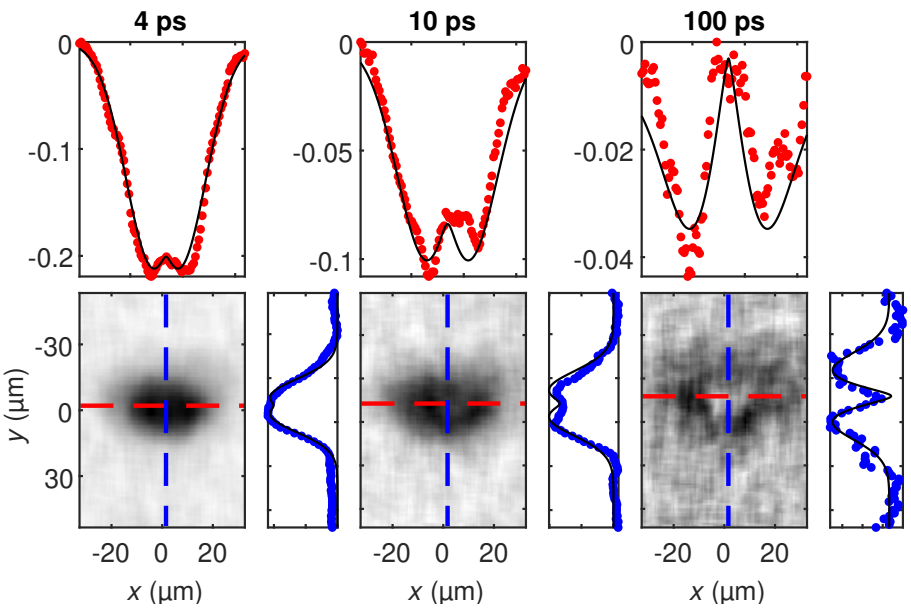

Figure 2.25: Images of $\varepsilon_1(t)$ for 2.25 eV probe-photon energy and selected time delays. The *dashed lines* indicate the position of the cross sections. The scale of the cross sections (*symbols*) is the same in both directions and the same as in the image at the respective time delay.

the combined effect of fast carrier transport and carrier cooling, both determined by the pump-laser-induced carrier-density profile.

For simplicity, the spatial carrier-density profile is assumed to consist of an inner region I, where the maximum pump intensity creates the largest electron (hole) density n_e^I (n_h^I). The inner region is surrounded by the outer region O, where a lower charge-carrier density ($n_e^O < n_e^I$ and $n_h^O < n_h^I$) is created. The density of electrons and holes $n_{e,h}$ determines the changes in the DF. In the inner region I, the high hole density n_h^I and their broad distribution in the Brillouin zone is determined by their temperature, which leads to the occurrence of the IVB absorption[1, 6], as visible in ε_2. However, this is not detected in the outer region O, where the hole density n_h^O is much lower. The electron density in the inner region n_e^I has no direct effect on ε_2 in the visible spectral range of ZnO, but it does have a strong influence on ε_1 via the Kramers-Kronig relations (KKR) [1]. This "KKR-effect" is weakly present in the outer region O, where $n_e^O < n_e^I$, because it requires a lower carrier density than the IVB absorption. This explains why $R_1 > R_2$ holds after a few picoseconds. Charge carriers undergo diffusion due to the pump-induced concentration gradient and loose their excess energy by scattering preferrably with longitudinal-optical (LO) phonons. Most excess energy is lost until 2 ps after excitation [1], but the re-absorption of phonons (hot-phonon effect[7, 8]) delays the carrier relaxation for several picoseconds and keeps the carrier temperature higher than the lattice temperature. The hot-phonon effect is dominating in the inner region I, because the larger carrier density induces a larger local phonon density, which increases the probability for phonon re-absorption contrary to O. Therefore, the energy loss rate is larger in the outer region O and thus the carrier temperature is larger in the inner

region *I*. In effect, there is a thermal gradient radially outwards and as soon as the resulting force becomes stronger than the diffusion due to the concentration gradient a ring forms gradually in the image of ε_1. This can be regarded as Seebeck effect due to the temperature gradient between the outer and the inner region as suggested by references [7, 8], which depends on the induced charge-carrier density and thus on the pump fluence.

A random-walk simulation starting from a two-dimensional Gaussian distribution of particles, mimicking carrier transport within the relaxation-time approximation, strongly indicates that ballistic carrier transport contributes simultaneously to the diffusion of the observed spatio-temporal evolution of the DF. This transport simulation reproduces the observed ring structure on the same time scale as observed in the experiment, assuming the speed $1,5\times10^6$ m/s and the scattering rate 1×10^{10} Hz of the particles [4]. Our simulation can be regarded as a very simplified version of the microscopic models reported in Refs. [7, 8]. In effect, this would influence the results of the pump-probe experiments without spatial resolution when the respective beam spot radii are of the same magnitude as the carrier's propagation distance.

[1] S. Richter *et al.*, *Ultrafast dynamics of hot charge carriers in an oxide semiconductor probed by femtosecond spectroscopic ellipsometry*, https://arxiv.org/abs/1902.05832v2
[2] S. Espinoza *et al.*, Appl. Phys. Lett. **115**, 052105 (2019), doi:10.1063/1.5109927
[3] T. Pflug *et al.*, Appl. Phys. A **124**, 17572 (2018), doi:10.1007/s00339-018-1550-4
[4] O. Herrfurth *et al.*, Appl. Phys. Lett. **115**, 212103 (2019), doi:10.1063/1.5128069
[5] M. Schubert, Phys. Rev. B **56**, 4075 (1996), doi:10.1103/PhysRevB.53.4265
[6] A. Segura *et al.*, Phys. Rev. B **56**, 4075 (1997), doi:10.1103/physrevb.56.4075
[7] M. M. Glazov, Phys. Rev. B **100**, 045426 (2019), doi:10.1103/PhysRevB.100.045426
[8] R. Perea Causín, Nano Lett. **19**, 7317 (2019), doi:10.1021/acs.nanolett.9b02948

2.15 Ellipsometric evidence for defect induced magnetism in spinel ferrite thin films

V. Zviagin, C. Sturm, R. Denecke*, P. Esquinazi, M. Grundmann, R. Schmidt-Grund†

*Universität Leipzig, Wilhelm-Ostwald-Institut für Physikalische und Theoretische Chemie, Linnéstr. 2, Germany
†Technische Universität Ilmenau, Institut für Physik, Ilmenau, Germany

The wide range of tunable properties in spinel iron oxides can be realized through the optimization of synthetic fabrication and treatment parameters. For example, the magnetic and electric properties of inverse spinel magnetite ($Fe^{2+}Fe_2^{3+}O_4$), a half-metallic ferromagnet, can be tuned to a ferrimagnetic semiconductor or to that of normal spinel franklinite ($Zn^{2+}Fe_2^{3+}O_4$), a superparamagnetic insulator by Zn substitution. In our work, the dielectric function of $ZnFe_2O_4$ thin films of a wide range of crystalline quality was parametrized and individual approximation functions were assigned to electronic transitions involving valence- and site-specific cations based on their resonance energy. Ideally, $ZnFe_2O_4$ consists of tetrahedrally and octahedrally coordinated lattice sites occupied by Zn^{2+} and Fe^{3+} cations, respectively, shown in (Fig. 2.26(e)).

However, the increase in Fe^{3+} on the tetrahedral site was directly related to the increase in amplitude of the Gaussian function located at 3.5 eV. This transition showed an increase in the magneto-optical response at the same energy as well as the magneto-static response with the decrease in fabrication temperature of $ZnFe_2O_4$ thin films[1, 2]. The presence of tetrahedral Fe^{3+} would be due to a cation inversion, namely the Zn and Fe exchange (Fig. 2.26(d)), or due to Fe on nominally unoccupied tetrahedral lattice site (Fig. 2.26(b)). In both cases, the antiferromagnetic interaction between tetrahedral and octahedral Fe^{3+} cations would be dominant, yielding a strong ferrimagnetic response.

The semiconducting properties of $ZnFe_2O_4$ thin films were realized by the choice of a low oxygen partial pressure during deposition. This was related to the presence of Fe^{2+} cations as a result of oxygen vacancies, which show a strong contribution to the ferrimagnetic order, schematically depicted in Fig. 2.26(c). Additional contributions were necessary for the description of the dielectric function of $ZnFe_2O_4$ grown at low oxygen partial pressure or upon annealing the high pressure films in argon at 250 ℃. The features ≤2 eV were related to electronic transitions between d orbitals of Fe^{2+}[3]. The decrease in this defect was apparent after annealing the low pressure grown films in oxygen atmosphere. Consistent with previous X-ray studies, both defects were found to decrease upon annealing at temperatures above 300 ℃ in oxygen and argon atmospheres. This was explained by the cation recrystallization toward a normal spinel cation configuration and a significant decrease in the net ferrimagntic response was observed. By varying the Zn concentration in the $Zn_xFe_{3-x}O_4$ thin films from 0 to 1.26, a spinel of inverse to normal configuration was achieved. Comparing the cation distribution in film bulk (optical transitions in the dielectric function) and near-surface region (X-ray absorption), it was found that an inhomogeneous cation distribution leads to a weaker magnetic response in films of inverse configuration, whereas defects in the normal spinel are likely to be found at the film surface. The spectroscopic determination of the type and concentration of individual defects allows the possibility to engineer the defect distribution in the thin film structure and tailor the desired magnetic properties.[3]

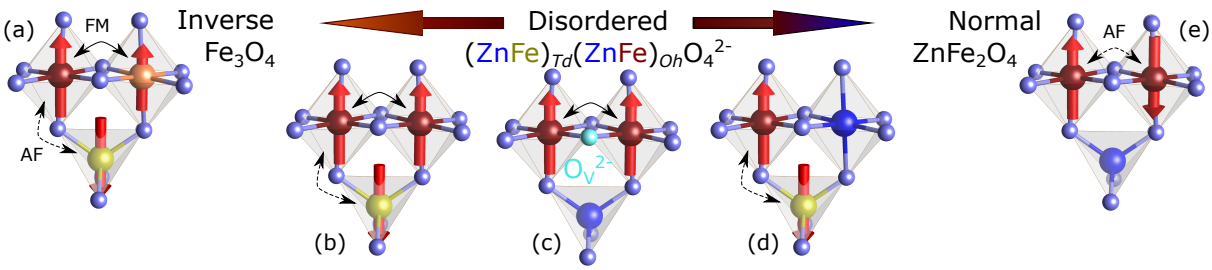

Figure 2.26: Schematic representation of main magnetic configurations and interactions between neighboring cations. (a) Inverse spinel magnetite $Fe^{2+}Fe_2^{3+}O_4$. (b) Disordered $ZnFe_2O_4$ with Fe^{3+} on nominally unoccupied tetrahedral lattice site. (c) Disordered $ZnFe_2O_4$ with the presence of an oxygen vacancy. (d) Disordered $ZnFe_2O_4$ due to the inversion mechanism. (e) Normal $ZnFe_2O_4$ with antiferromagnetic interaction between Fe^{3+}.

[1] V. Zviagin *et al.*, Phys. Status Solidi B **253**, 429 (2016), doi:10.1002/pssb.201552361
[2] V. Zviagin *et al.*, Appl. Phys. Lett. **108**, 13 (2016), doi:10.1063/1.4944898
[3] V. Zviagin *et al.*, Phys. Status Solidi B **2020**, 1900630 (2020), doi:10.1002/pssb.201900630

2.16 Dielectric function of κ-(In,Al,Ga)$_2$O$_3$ thin films

A. Müller, C. Sturm, A. Hassa, M. Kneiß, M. Grundmann

The large band gap energy of about 4.9 eV makes Ga_2O_3 interesting as a deep-UV transparent semiconducting oxide (TSO). The dielectric function (DF) for the monoclinic β-phase of Ga_2O_3 was already discussed in detail, e.g. Ref. [1–3]. The orthorhombic κ-phase is attractive due to its large predicted spontaneous polarization of about 23 µC/cm^2 along its c-axis [4]. However, this phase lacks a full characterization of its optical properties. Furthermore, the incorporation of In as well as Al into Ga_2O_3 as ternary material is interesting for band-gap engineering, but its impact on the DF and vibrational properties is yet to be explored. Here, we report on the optical properties, in particular the DF, which was determined by spectroscopic ellipsometry. The investigated thin films have been grown in (001)-orientation on c-plane sapphire substrates by tin-assisted pulsed laser deposition [5, 6].

Due to the orthorhombic crystal structure the DF of $\kappa - (\mathrm{In, Al, Ga})_2\mathrm{O}_3$ is a diagonal tensor with three independent complex-valued components. Since the deposited film consist of three in-plane rotation domains, the films are effectively optical uniaxial with the optic axis parallel to the surface normal. Thus, in-plane components of the DF are equal, i.e. $\varepsilon_{xx} = \varepsilon_{yy} = \varepsilon_{\perp} \neq \varepsilon_{zz} = \varepsilon_{\parallel}$.

The line-shape of each component of the DF was described by using CPM$_0$ band-band transition and Gaussian oscillator model functions. In the resulting DF, the onset of the absorption is red(blue)-shifted with increasing In(Al) concentrations (Figure 2.27). The band gap can therefore be controlled in the range 4.2 – 5.6 eV by varying the In/Al concentrations. For In concentrations > 23 %, hints of free charge carrier contribution are observable (Figure 2.27). In the case of Al alloying, the line-shape of the DF is similar to those of the β-phase of Ga_2O_3 for all concentrations.

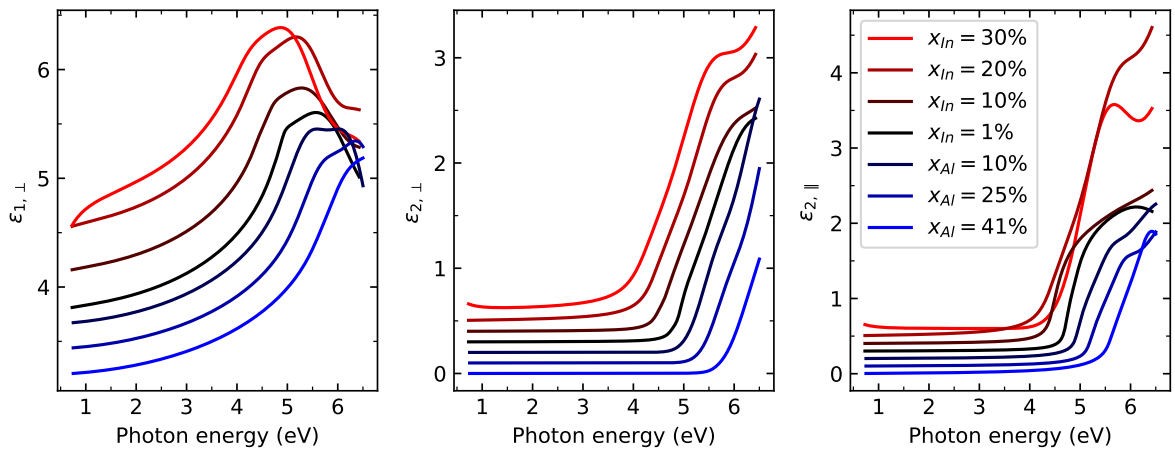

Figure 2.27: Real (a) and imaginary (b, c) components of the dielectric function of $\kappa - (\mathrm{In, Al, Ga})_2\mathrm{O}_3$ for various In and Al concentrations.

The examination in the infrared spectral range showed that the DF is mainly described by 4 phonon modes (Figure 2.28). The corresponding phonon energies decrease with increasing In concentrations (Figure 2.28), and for large In concentrations the phonons were possibly screened by free charge carriers.

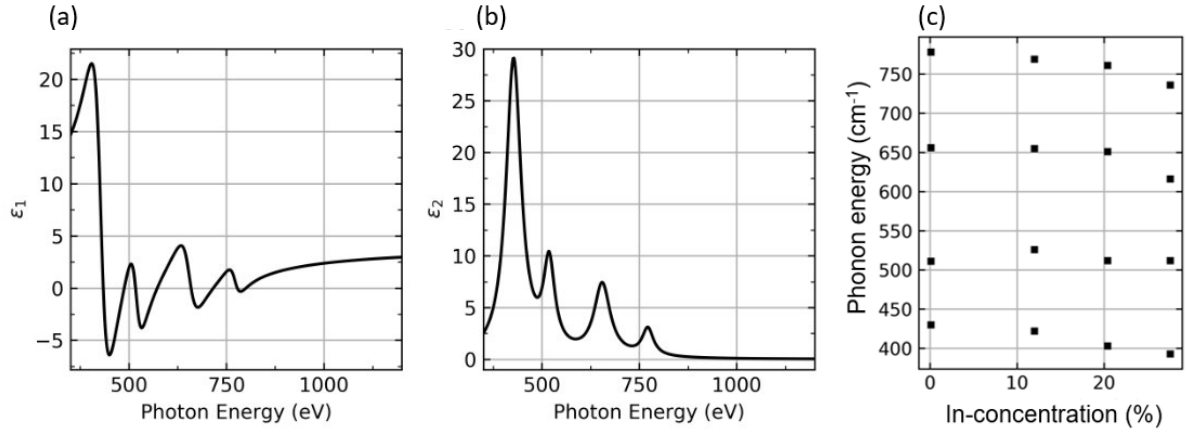

Figure 2.28: Real (a) and imaginary (b) component of the dielectric function of a $\kappa - (In_{0.03}, Ga_{0.97})_2O_3$ thin film in the infrared spectral range. (c) The phonon energy as a function of the In concentration.

[1] C. Sturm *et al.*, APL Mater **3**, 106106 (2015), doi:10.1063/1.4934705
[2] C. Sturm *et al.*, Phys. Rev. B **94**, 035148 (2016), doi:10.1103/PhysRevB.94.035148
[3] A. Mock *et al.*, Phys. Rev. B **96**, 245205 (2017), doi:10.1103/PhysRevB.96.245205
[4] M. B. Maccioni *et al.*, Appl. Phys. Express **9**, 04102 (2016), doi:10.7567/apex.9.041102
[5] M. Kneiß *et al.*, APL Mater **7**, 022516 (2019), doi:10.1063/1.5054378
[6] H. v. Wenckstern *et al.*, CrystEngComm **15**, 100020 (2013), doi:10.1039/C3CE41327F

2.17 Low temperature optical properties of CuI thin film

V. Zviagin, J. Kremkow, E. Krüger, C. Yang, C. Sturm, M. Grundmann

Inspired by their remarkable properties, such as flexibility, transparency and p-type conductivity, $\gamma -$ CuI thin films have attracted significant interest for applications in transparent optoelectronic and thermoelectric devices[1]. However, a deeper understanding of the nature of the electronic structure is necessary for the design of novel transparent optoelectronic devices. In our recent work, we determined the dielectric function of CuI by means of spectroscopic ellipsometry in the spectral range from 0.5 eV to 8.3 eV for temperatures from 10 K to 300 K[2]. The observed features were assigned to electronic transitions in the Brillouin zone, in agreement with theoretical calculations. Based on their temperature dependence, the electron-phonon coupling for the lowest transitions at the Γ-point was found to be smaller than for the high-energy transitions at other symmetry points in the Brillouin zone. The numerical approximation of the dielectric function at 10 K was parametrized in the spectral range from 0.5 eV to 4.0 eV. It was determined that the CuI thin film behaves as an optically anisotropic material at 10 K due to biaxial thermal stress. In this case, the model approximation matches the transmission spectra at that temperature and yields a significant improvement in the fit to the experimentally determined spectra, (Fig. 2.29(a)). Two Tanguy oscillators and one Gaussian function were placed at 3.1 , 3.7 and 4.3 eV, respectively. The imaginary part of the model approximation for polarization parallel ($\varepsilon_{2\|}$) and perpendicular ($\varepsilon_{2\perp}$) to the interface normal of CuI thin film with individual function contributions to the

$\varepsilon_{2\perp}$ is depicted in Fig. 2.29(b). In our future work, the numerically determined dielectric function is to be parametrized in the full measured range and the behavior of individual function parameters is to be analyzed as a function of measured temperature.

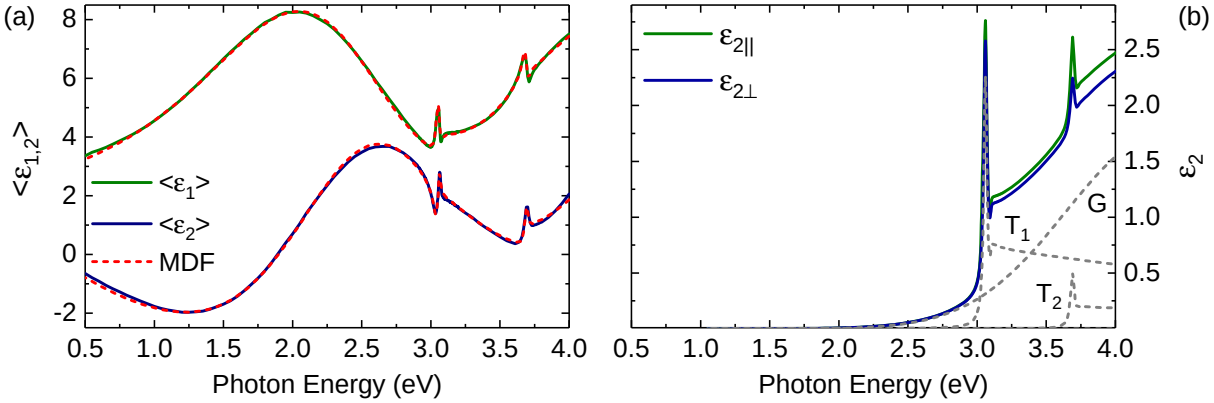

Figure 2.29: (a) Model fit to the experimentally determined spectra of the pseudo dielectric function $\langle\varepsilon_{1,2}\rangle$ at 10 K. (b) Imaginary part of the model dielectric function (MDF) at 10 K for polarization parallel ($\varepsilon_{2,\|}$) and perpendicular ($\varepsilon_{2,\perp}$) to the c-axis of CuI thin film. The functions used to approximate $\varepsilon_{2,\perp}$ are depicted by dashed gray lines.

[1] M. Grundmann *et al.*, Phys. Status Solidi A **210**, 9 (2013), doi:10.1002/pssa.201329349
[2] E. Krüger *et al.*, Appl. Phys. Lett. **113**, 172102 (2018), doi:10.1063/1.5051963

2.18 Influence of the excitation wavelength on the emission properties of carbon nanodots

L. Trefflich, C. Hennemann*, F. Dissinger†, R. Schmidt-Grund‡, C. Sturm, S.R. Waldvogel†, M. Grundmann

*Wilhelm-Ostwald-Gymnasium, Willi-Bredel-Strasse 15, 04279 Leipzig, Germany
†Johannes Gutenberg-Universität Mainz, Department Chemie, Duesbergweg 10-14, 55128 Mainz, Germany
‡now at: Technische Universität Ilmenau, Institut für Physik, Weimarer Str. 25, 98693 Ilmenau, Germany

Carbon nanodots (cdots) are discrete quasi-spherical nanoparticles with diameters below 10 nm [1], which can be synthesized from many environmentally friendly resources, such as grass, tea, coffee and citric acid [1]. Cdots exhibit compelling properties, such as biocompatibility[2], a strong, tunable photoluminescence (PL) and a high stability against photobleaching[3]. This has led to numerous applications in chemistry, physics and life sciences, ranging from photocatalysis[4], chemical sensing[5] and bio-imaging[6] to drug delivery[7]. Cdots have also been used to produce white light LEDs[8], which do not require rare earth elements. Their use as an active material component for laser applications has been recently reported[9]. Our goal is to incorporate cdots in a planar microcavity[10] to develop a tunable, environmentally friendly laser

source. The optical properties of cdots have been extensively studied, but contradicting results have been reported. Some investigations show a dependence of the emission properties on the excitation wavelength, while others do not. Zhang *et al.* pointed out that carbon nanodots, which show no dependence of the emission wavelength on the excitation wavelength, are better suited as an active laser material[11]. Therefore, we investigated the excitation wavelength dependence of the cdots, which were used in our studies in the frame of the BeLL (german, Besondere Lernleistung) of C. Hennemann.

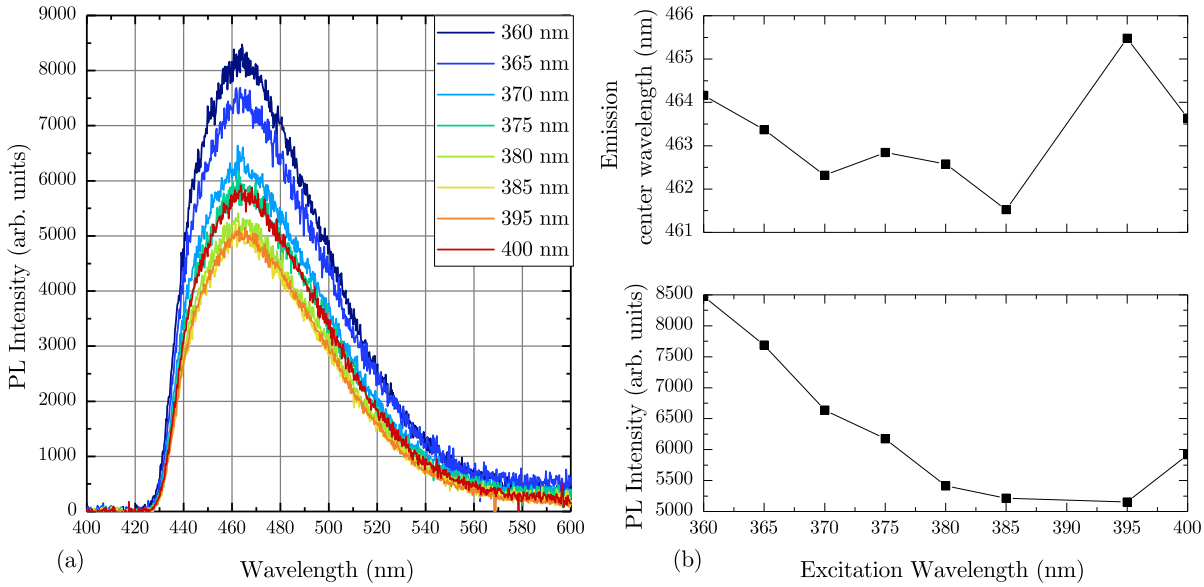

Figure 2.30: (a) Photoluminescence spectra of carbon nanodots for excitation wavelengths between 360 nm and 400 nm. (b) Maximum photoluminescence intensity and emission center wavelength as a function of the excitation wavelength. A shift in the center emission wavelength was not observed, which is beneficial for the use as gain material [9]. Excitation with shorter wavelengths does give a stronger photoluminescence signal, which might be favorable for LED or laser applications.

The carbon nanodot powder was synthesized by F. Dissinger using a pyrolysis method and a 2-aminothiophenol precursor following a protocol by Hu *et al.* [12]. Further information about the synthesis can be found in the supplementary information of [13]. A cdot solution was produced by solving 10 mg cdot powder in 10 ml ethanol using an ultrasonic cleaner. It was then filled in a sealed fused silica cuvette. A 150 W halogen lamp was used as a light source for the photoluminescence spectroscopy experiment. Single wavelengths from the continuous spectrum of the halogen lamp were selected using a Zeiss SPM2 prism monochromator. The cdot solution was then excited with light of wavelengths between 360 nm and 400 nm. This resembles the wavelengths later used for lasing experiments. The intensity of the excitation source was monitored using a Thorlabs S130VC Si diode. The measured intensity was corrected for the varying bandwidth of the monochromatic light, due to the nonlinear dispersion of the prism monochromator. It was kept constant for all excitation wavelengths using a variable neutral density filter. The photoluminscence response was collected using a quarz lens and spectrally analyzed using a Horiba iHR320 monochromator with a Jobin Yvon Open STE CCD camera. Fig. 2.30 (a) shows the measured PL signal of the carbon

nanodots for excitation wavelengths between 360 nm and 400 nm. The cdots exhibit a broad emission between 430 nm and 560 nm with an asymetric line-shape. Fig. 2.30 (b) shows a clear trend of the measured PL intensity for different excitation wavelengths. Excitation with shorter wavelengths (≤ 385 nm) increases the emission intensity by a factor of 1.7. Excitation with shorter wavelengths could therefore be beneficial where maximum emission is needed, for example in LED or laser applications. A shift in emission wavelength with varying excitation wavelengths was not observed. The measured variations are due to the noise in the recorded spectra. We therefore conclude that the cdots, used in our experiments, should be well suited as a gain medium for laser applications.

[1] P. Roy *et al.*, Mater. Today **18**, 8 (2015), doi:10.1016/j.mattod.2015.04.005
[2] J.C.G.E. da Silva *et al.*, Trends Anal. Chem. **30**, 8 (2011), doi:10.1016/j.trac.2011.04.009
[3] Y. Sun *et al.*, J. Am. Chem. Soc. **128**, 24 (2006), doi:10.1021/ja062677d
[4] L. Cao *et al.*, J. Am. Chem. Soc. **133**, 4754 (2011), doi:10.1021/ja200804h
[5] Y. Dong *et al.*, Anal. Chem. **84**, 6220 (2012), doi:10.1021/ac3012126
[6] M. M. F. Baig *et al.*, J. Colloid Interface Sci. **501**, 341 (2017), doi:10.1016/j.jcis.2017.04.045
[7] J. Pardo *et al.*, Molecules **23**, 2 (2018), doi:10.3390/molecules23020378
[8] L. Tang *et al.*, ACS Nano **6**, 6 (2012), doi:10.1021/nn300760g
[9] W. Zhang *et al.*, Nanoscale **9**, 5957 (2017), doi:10.1039/c7nr01101f
[10] H. Hilmer *et al.*, AIP Conf. Proc. **1199**, 151 (2010), doi:10.1063/1.3295340
[11] Y. Zhang *et al.*, ACS Appl. Mater. Interfaces **8**, 38 (2016), doi:10.1021/acsami.6b08315
[12] S. Hu *et al.*, Angew. Chem. Int. Ed. **54**, 10 (2015), doi:10.1002/anie.201411004
[13] F. Dissinger *et al.*, Phys. Status Solidi B **256**, 4 (2019), doi:10.1002/pssb.201800493

2.19 Structural and optical properties of oxygen-doped TiN thin films

F. Delatowski, C. Sturm, F. Jung, S. Hohenberger, M. Lorenz, M. Grundmann

The epitaxial growth of MgO and TiN superlattices allows the realization of optical hyperbolic metamaterials in form of planar periodic nanostructures, consisting of a plasmonic and a dielectric component [1, 2]. Due to the high oxygen affinity of titanium, it is suspected that diffusion of oxygen from the MgO layer into the TiN layers or oxidation occurs during the deposition process [3]. Therefore, the structural and optical properties of oxygen-doped TiN thin film layers are investigated as a function of the doping concentration and the temperature in order to understand the impact of oxygen doping on the properties of the TiN layers and superlattices.

The thin films were fabricated by pulsed laser deposition (PLD) on annealed (100) MgO substrates with a selective miscut angle between 0.05° and 0.1° [4]. Substrate temperatures were varied between room temperature and 600 °C. The growth modes and layer thickness was investigated during the deposition using *in-situ* reflection high-energy electron diffraction (RHEED). The oxygen doping was realized by using an

oxygen-argon gas mixture during the deposition process, whereby the lower technical limit was kept constant $F_{\%} = 0.5\%$ of oxygen in the gas flow.

X-ray diffraction (XRD) and x-ray reflection (XRR) measurements were performed to determine crystal structure and thickness, using a PANanalytical X'pert PRO MRD. For the detection of the high resolution 2Θ-ω scans, an additional secondary monochromator with proportional counter (triple-axis) was used. For substrate temperatures below 500 ℃ the TiN thin film peaks become less prominent and an additional peak is visible at $2\Theta = 48.07°$, which can be related to the (200) TiO_2-anatase reflex [5]. For the films deposited at room temperature neither of the two peaks are visible, whereby amorphous material growth is expected.

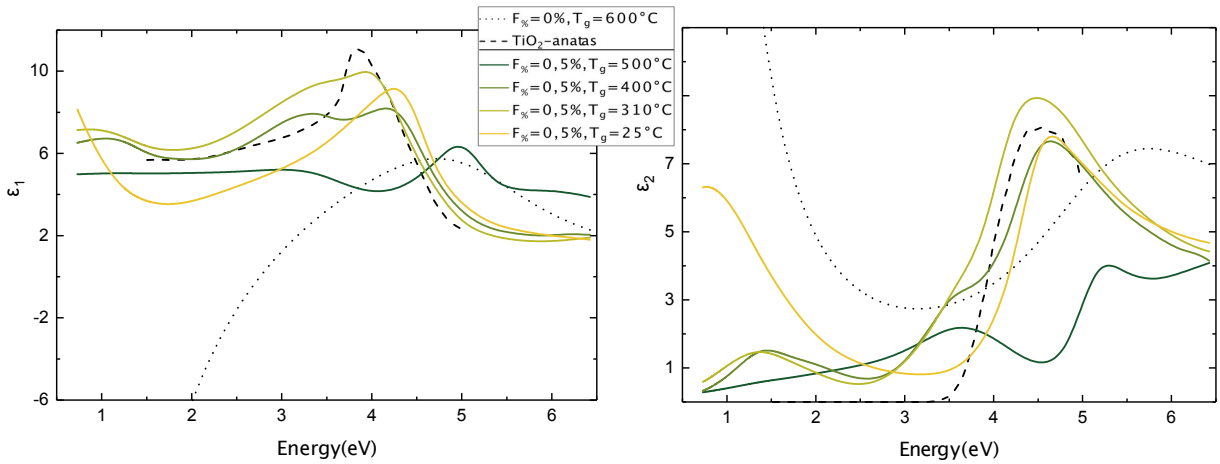

Figure 2.31: Real and imaginary part of the material dielectric function for various substrate temperatures at an oxygen flow of $F_{\%} = 0.5\%$, as compared to the dielectric function of TiN (at $F_{\%} = 0\%$) and TiO_2-anatase [6].

Atomic force microscopy was used to investigate the thin film surface morphology, whereas the dielectric function (DF) of the thin films was determined by spectroscopic ellipsometry in the spectral range between 0.7 eV and 6.5 eV, using a J.A. Woollam RC 2 ellipsometer. The description of the DF was achieved using a numerical B-spline approximation.

The dielectric function for films grown at various substrate temperatures with $F_{\%}$= 0.5% oxygen in the gas flow is shown in Fig. 2.31. The imaginary component of the DF, contains features, characteristic of both TiN and TiO_2, such as a metallic free carrier absorption in the visible spectral range and a sharp transition in the vicinity of the TiO_2 band gap. In contrast to metallic TiN, the real component of the DF is positive for all samples grown with oxygen presence in the deposition chamber. Therefore, plasmonic behavior ($\varepsilon_1 < 0$) is not visible in the measured spectral range.

Our results suggests that samples were produced exhibiting an optical response, which is characteristic of a metallic and a dielectric behavior. Furthermore, it can be concluded that the 2D layer by layer growth and the plasmonic behavior of TiN is likely hindered by the presence of oxygen during the deposition. Consequently, TiN grown under oxygen flow of $F_{\%} \geq 0.5\%$ and at different substrate temperatures is in this case not suitable for the realization of optical hyperbolic metamaterials.

[1] G.V. Naik *et al.*, Opt. Mater. Express **2**, 4 (2012), doi:10.1364/OME.2.000478

[2] G.V. Naik *et al.*, PNAS **111**, 21 (2014), doi:10.1073/pnas.1319446111
[3] F. Jung: *Optical and structural properties of TiN/MgO superlattices*, Master thesis, Universität Leipzig (2018)
[4] M. Bonholzer *et al.*, Phys. Status Solidi A **211**, 11 (2014), doi:10.1002/pssa.201431458
[5] J.K. Burdett *et al.*, J. Am. Chem. Soc . **109**, 3639 (1987), doi:10.1021/ja00236a013
[6] Y.R. Park *et al.*, Thin Solid Films **484**, 1 (2005), doi:0.1016/j.tsf.2005.01.039

2.20 A vortex plate in the Mach-Zehnder Interferometer

A. Märcker, M. Grundmann

As demonstration of the effect of a phase plate on a Gaussian beam in the lecture on Experimental Physics 2 (electrodynamics and optics), a vortex plate has been placed in one arm of a Mach-Zehnder interferometer (Fig. 2.32a). The two exits of the interferometer are projected next to each other and are complementary. Without the vortex plate, a ring-like pattern develops in the slightly divergent beam. The vortex plate (for 532 nm) creates a spiral like pattern (Fig. 2.32b). Small variations of the optical path length lead to a rotation of the spiral which can be nicely captured on video.

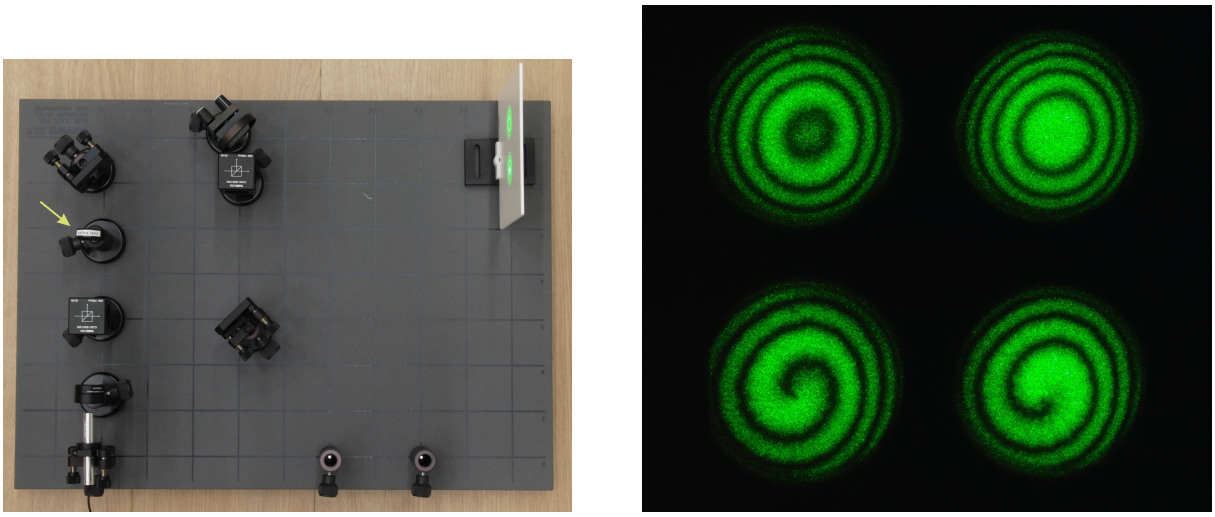

Figure 2.32: (**a**) Bird's eye view of a Mach-Zehnder interferometer with a vortex plate (arrow) within the left arm. (b) Interference patterns without (upper row) and with (lower row) the vortex plate.

3

Funding, Organizational Duties, External Cooperations

3.1 Funding

Polarisationswechselwirkung in Laser-MBE Wurtzit-Perowskit-Heterostrukturen
Prof. Dr. M. Lorenz
SFB 762/3, TP A2 within SFB 762 *Funktionalität Oxidischer Grenzflächen*

Optische Untersuchungen zu magneto-elektro-optischen Wechselwirkungen in ihrer Dynamik in oxidischen Heterostrukturen
Dr. R. Schmidt-Grund
SFB 762/3, TP B03 within SFB 762 *Funktionalität Oxidischer Grenzflächen*

Lateraler Transport in oxidischen Feldeffekt-Strukturen
Dr. H. von Wenckstern, Prof. Dr. M. Grundmann
SFB 762/3, TP B04 within SFB 762 *Funktionalität Oxidischer Grenzflächen*

Spinabhängiges Tunneln in oxidischen Heterostrukturen
Prof. Dr. M. Grundmann, Prof. Dr. B. Rosenow
SFB 762/3, TP B06 within SFB 762 *Funktionalität Oxidischer Grenzflächen*

Quantum Gases and Liquids in Semiconductor Rods conformally coated with Bragg Mirrors
Dr. R. Schmidt-Grund, Prof. Dr. M. Grundmann
DFG SCHM 2710/2-2, TP P1 within FOR 1616 *Dynamics and Interactions of Semiconductor Nanowires for Optoelectronics*

Flexible analoge und digitale Grundschaltungen in amorphen Metalloxiden
Prof. Dr. M. Grundmann
DFG GR 1011/31-2, within SPP *High Frequency Flexible Bendable Electronics for Wireless Communication Systems (FFLexCom)*

Raman-Streuung in anisotropen Kristallen
Prof. Dr. M. Grundmann
GR 1011/33-1

Topologische Effekte in optisch-anisotropen Mikrokavitäten
Dr. R. Schmidt-Grund
DFG SCHM 2710/3-1

Wurtzitische Zink-basierte Oxynitride als vielversprechende photovoltaische Absorber: Epitaxie, Bandstruktur-Anpassung und Heterostrukturen
Dr. C. Yang
YA 511/1-1

Zink-Magnesium Oxinitride
Prof. Dr. M. Grundmann
GR 1011/36-1 (DFG – ANR, cooperative project)

Zwischenband-Solarzellen auf Basis Übergangsmetall-substitutierter Indium-thiospinelle
Dr. H. von Wenckstern
WE 4620/3-1

Remanentes Schalten von Bloch-Polaritonen
Dr. C. Sturm
STU 647/2-1

Koordinationsfonds
Prof. Dr. M. Grundmann
GR 1011/41-1 within FOR 2857 *Kuperiodid als multifunktionaler Halbleiter*

Mikrostruktur-basierte Optimierung des Wachstums dünner CuI-Filme
Prof. Dr. M. Lorenz
LO 790/7-1, P01 within FOR 2857 *Kupferiodid als multifunktionaler Halbleiter*

Amorphe Kupferiodid-Dünnfilme und Kupferiodid-basierte Legierungshalbleiter
Prof. Dr. M. Grundmann
GR 1011/40-1, P03 within FOR 2857 *Kupferiodid als multifunktionaler Halbleiter*

Amorphe Kupferiodid-Dünnfilme und Kupferiodid-basierte Legierungshalbleiter
Dr. C. Yang
YA 511/2-1, P03 within FOR 2857 *Kupferiodid als multifunktionaler Halbleiter*

Elektrische Eigenschaften von CuI Dünnfilmen und Volumenkristallen und Herstellung von CuI-basierten Bauelementen
Dr. H. von Wenckstern
WE 4620/5-1, P05 within FOR 2857 *Kupferiodid als multifunktionaler Halbleiter*

Optische Eigenschaften von Kupferiodid, dotierten Kupferiodid und Kupferiodid-basierten Legierungshalbleitern
Dr. C. Sturm
STU 647/3-1, P06 within FOR 2857 *Kupferiodid als multifunktionaler Halbleiter*

COSIMA – Combinatorisches Oxid-Screening für Materialien und Anwendungen
Prof. Dr. M. Grundmann
Europäischer Fonds für regionale Entwicklung (EFRE)
100282338 and 100315366

Nachwuchsforschergruppe – Oxid-Heterostrukturen: Anwendungen in Bauelementen
Prof. Dr. M. Grundmann
Europäische Sozialfonds (ESF)
100310460

3.2 Organizational Duties

M. Grundmann

- Vice Dean of the Faculty of Physics and Earth Sciences
- Director of the Felix Bloch Institute for Solid State Physics
- Sprecher der Graduiertenschule "Leipzig School of Natural Sciences - Building with Molecules and Nano-objects" (BuildMoNa), http://www.buildmona.de/
- Stellvertretender Sprecher des Sonderforschungsbereiches "Funktionalität Oxidischer Grenzflächen" (SFB 762), http://www.physik.uni-halle.de/sfb762/
- Sprecher der Forschungsgruppe FOR 2857 "Copper Iodide as Multifunctional Semiconductor", https://research.uni-leipzig.de/for2857/
- Sprecher der Fächerübergreifenden Arbeitsgemeinschaft Halbleiterforschung Leipzig (FAHL), https://home.uni-leipzig.de/fahl/
- Sprecher des Freundeskreis der Fakultät für Physik und Geowissenschaften
- Member Editorial Board: Physica Status Solidi (a), (b), RRL, MDPI nanomaterials, Phys. Rev. Research
- Member International Advisory Board: Advanced Electronic Materials
- Project Reviewer: diverse
- Referee: Applied Physics Letters, Electronics Letters, Journal of Applied Physics, Nature, Physica E, Physical Review B, Physical Review Letters, Physica Status Solidi, Advanced Materials, u.a.

M. Lorenz

- Member Editorial Board: Journal of Physics D: Applied Physics (IOP, Bristol, U.K.), Editorial Board Member of Journal Materials (MDPI, Basel, Switzerland)
- Project Reviewer: Deutsche Forschungsgemeinschaft, Heisenberg-Programm Alexander von Humboldt - Stiftung, Czech Science Foundation, Israel Science Foundation, Netherlands Organisation for Scientific Research (NWO)
- Referee: Advanced Functional Materials, Applied Physics Letters, Applied Physics A, Crystal Growth and Design, CrystEngComm, Emergent Materials, Journal of Physics D: Applied Physics, Journal of Alloys and Compounds, Journal of Applied Physics, Journal: Optics and Laser Technology, Materials, Nature Materials, New Journal of Chemistry, Physica B, Progress in Materials Science, Vacuum

R. Schmidt-Grund

- Extended board member of German Association on Ellipsometry (Arbeitskreis Ellipsometrie – Paul Drude e.V.)
- Project Reviewer: Deutsche Forschungsgemeinschaft (DFG), US Department of Energy, Österreichische Akademie der Wissenschaften, German-Israeli Foundation for Scientific Research and Development
- Referee: Scientific journals (ACS, AIP, APS, DPG, Elsevier, IOP, MRS, Nature Publ. Group, OSA, PIER,Wiley)

P. Schlupp
- Referee: ACS Applied Materials and Interfaces

D. Splith
- Referee: Applied Physics Express, Physica Status Solidi A, IEEE Transactions on Electron Devices

C. Sturm
- Referee: APL, Applied Physics, JVSTA, JVSTB, Opt. Lett., Optical Materials Express, Optics Commun., Phys. Rev. B

H. von Wenckstern
- Project Reviewer: Deutsche Forschungsgemeinschaft, U.S. Department of Energy – Office of Science, National Research Fondation RSA
- Associate Editor: Journal of Electronic Materials
- Referee: ACS Materials and Interfaces, Advanced Functional Materials, Annalen der Physik, Applied Physical Letters, APL Materials, Electronic Device Letters, Journal of Applied Physics, Material Science in Semiconductor Processing, Physica Status Solidi, Scientific Reports, Solid State Electronics, Superlattices and Microstructures, Thin Solid Films, u.a.

C. Yang
- Referee: Materials Horizons, Applied Physics Letters, Physical Review Applied, Nanoscale, Advanced Materials Interfaces

V. Zviagin
- Referee: Applied Physics Letters, Materials Research Review, Physica Scripta, Materials Research Express

3.3 External Cooperations

Academic

- Leibniz-Institut für Oberflächenmodifizierung e. V., Leipzig, Germany
  Prof. Dr. A. Anders, Prof. Dr. S. Mayr, Dr. C. Bundesmann, Dr. A. Lotnyk
- Universität Leipzig, Fakultät für Chemie und Mineralogie, Germany
  Prof. Dr. H. Krautscheid, Prof. Dr. R. Denecke, Prof. Dr. O. Oeckler, Dr. V. Gottschalch, Dr. S. Blaurock
- Universität Halle-Wittenberg, Germany
  Prof. Dr. I. Mertig, Prof. Dr. S.G. Ebbinghaus, Prof. Dr. W. Hergert, Prof. Dr. R. Scheer
- Fraunhofer-Institut für Mikrostruktur von Werkstoffen und Systemen IMWS, Halle (Saale), Germany
  Prof. Dr. T. Höche, Dr. C. Patzig, Dr. S. Selle
- Forschungszentrum Dresden-Rossendorf, Germany
  Dr. S. Zhou
- Technische Universität Berlin, Germany

- Humboldt-Universität zu Berlin, Germany
  Prof. Dr. N. Koch
- Leibniz-Institut für Festkörperelektronik – Paul Drude (PDI), Berlin, Germany
  Dr. O. Bierwagen
- Universität Magdeburg, Germany
  Porf. Dr. A. Dadgar, Dr. J. Bläsing
- Universität Jena, Germany
  Prof. Dr. C. Ronning, Prof. Dr. S. Botti
- Technische Universität Ilmenau, Germany
  Prof. Dr. S. Krischok, Dr. R. Schmidt-Grund
- Johannes Gutenberg-Universität Mainz, Department Chemie, Germany
  Prof. Dr. S.R. Waldvogel
- Hochschule Mittweida, Laserinstitut, Germany
  Prof. Dr. A. Horn, T. Pflug, M. Olbrich
- University of Canterbury, Christchurch, New Zealand
  Prof. Dr. M. Allen
- Centre de Recherche sur l'Hétéro-Epitaxie et ses Applications (CNRS-CRHEA), Valbonne, France
  Dr. J. Zúñiga-Pérez, Dr. Guy Feuillet
- Western Michigan University, USA
  Prof. Dr. S. M. Durbin
- The Ohio State University, USA
  Prof. Dr. L. Brillson
- Arizona State University, USA
  Prof. F. Ren
- University of Florida, USA
  Prof. S. Pearton
- Katholieke Universiteit Leuven, Belgium
  Dr. V. Lazenka, Prof. Dr. K. Temst
- University of Oslo, Norway
  Prof. Dr. L. Vines
- ELI Beamlines - International Laser Research Centre, Dolní Brežany, Czech Republic
  Prof. J. Andreasson, Dr. S. Richter, Dr. S. Espinoza, Dr. M. Rebarz

Industry

- Freiberger Compound Materials GmbH, Freiberg, Germany
  Dr. G. Leibiger
- First Sensor AG, Berlin, Germany
  Dr. M. Schillgalies
- Optics Balzers Jena GmbH, Jena, Germany
  Dr. A. Rahm

4

Publications

Journals

L. Brillson, J. Cox, H. Gao, G. Foster, W. Ruane, A. Jarjour, M. Allen, D. Look, H. von Wenckstern, M. Grundmann: *Native Point Defect Measurement and Manipulation In ZnO Nanostructures*, Materials **12**(14), 2242: 1-15 (2019)

C. Fares, M. Kneiß, H. von Wenckstern, M. Grundmann, M. Tadjer, F. Ren, E. Lambers, S.J. Pearton: *Valence Band Offsets for ALD SiO_2 and Al_2O_3 on $(In_xGa_{1-x})_2O_3$ for x=0.25-0.74*, APL Mater. **7**(7), 071115: 1-7 (2019)

C. Fares, Z. Islam, A. Haque, M. Kneiß, H. von Wenckstern, M. Grundmann, M. Tadjer, F. Ren, S.J. Pearton: *Effect of Annealing on the Band Alignment of ALD SiO_2 on $(Al_xGa_{1-x})_2O_3$ for x=0.2-0.65*, ECS J. Solid State Sci. Techn. **8**(12), P751-P756 (2019)

C. Fares, M. Kneiß, H. von Wenckstern, M. Tadjer, F. Ren, E. Lambers, M. Grundmann, S.J. Pearton: *Band Alignment of Atomic Layer Deposited SiO_2 and Al_2O_3 on $(Al_xGa_{1-x})_2O_3$ for x=0.2-0.65*, ECS J. Solid State Sci. Techn. **8**(6), P351-P356 (2019)

M. Grundmann: *Monolithic Waveguide-based Linear Photodetector Array for Use as Ultra-Compact Spectrometer*, IEEE Transact. Electr. Dev. **66**(1), 470-477 (2019)

M. Grundmann: *Modeling of a waveguide-based UV-VIS-IR spectrometer based on a lateral (In,Ga)N alloy gradient*, Phys. Status Solidi A **216**(14), 1900170: 1-5 (2019)

V. Gottschalch, S. Merker, S. Blaurock, M. Kneiß, U. Teschner, M. Grundmann, H. Krautscheid: *Heteroepitaxial growth of α-, β-, γ- and κ-Ga_2O_3 phases by metalorganic vapor phase epitaxy*, J. Cryst. Growth **510**(15 March 2019), 76-84 (2019)

A. Hassa, H. von Wenckstern, D. Splith, C. Sturm, M. Kneiß, V. Prozheeva, M. Grundmann: *Erratum: "Structural, optical, and electrical properties of orthorhombic κ-$(In_xGa_{1-x})_2O_3$ thin films"*, APL Mater. **7**(7), 079901 (2019)

A. Hassa, H. von Wenckstern, D. Splith, C. Sturm, M. Kneiß, V. Prozheeva, M. Grundmann: *Structural, optical and electrical properties of orthorhombic κ-$(In_xGa_{1-x})_2O_3$ thin films*, APL Mater. **7**(2), 022525: 1-9 (2019)

A. Hassa, H. von Wenckstern, L. Vines, M. Grundmann: *Influence of oxygen pressure on growth of Si-doped $(Al_xGa_{1-x})_2O_3$ thin films on c-sapphire substrates by pulsed laser deposition*, ECS J. Solid State Sci. Techn. **8**(7), Q3217-Q2020 (2019)

O. Herrfurth, T. Pflug, M. Olbrich, M. Grundmann, A. Horn, R. Schmidt-Grund: *Femtosecond-time-resolved imaging of the dielectric function of ZnO in the visible to near-IR spectral range*, Appl. Phys. Lett. **115**(21), 212103: 1-5 (2019), (Editor's Pick)

R. Karsthof, M. Grundmann, M.Anton, F. Kremer: *Polaronic inter-acceptor hopping transport in intrinsically doped nickel oxide*, Phys. Rev. B **99**(23), 235201: 1-13 (2019) (Editor's Suggestion)

R. Karsthof, M. Grundmann, H. von Wenckstern, J. Zúñiga-Pérez, C. Deparis: *Nickel oxide-based heterostructures with large band offsets*, Phys. Status Solidi B **XXX**, 1900639: 1-11 (2019)

M. Kneiß, A. Hassa, D. Splith, C. Sturm, H. von Wenckstern, M. Lorenz, M. Grundmann: *Epitaxial Stabilization of Single Phase κ-$(In_xGa_{1-x})_2O_3$ Thin Films up to x=0.28 on c-sapphire and κ-Ga_2O_3 (001) Templates by Tin-assisted VCCS-PLD*, APL Mater. **7**(10), 101102: 1-10 (2019), (Editor's Pick)

M. Kneiß, A. Hassa, D. Splith, C. Sturm, H. von Wenckstern, T. Schultz, N. Koch, M. Grundmann: *Tin-Assisted Heteroepitaxial PLD-growth of κ-Ga_2O_3 Thin Films with High Crystalline Quality*, APL Mater. **7**(2), 022516: 1-11 (2019)

O. Lahr, S. Vogt, H. von Wenckstern, M. Grundmann: *Low-voltage operation of ring oscillators based on room-temperature-deposited amorphous zinc-tin-oxide channel MESFETs*, Adv. Electron. Mater. 2019, 1900548: 1-5 (2019)

O. Lahr, Z. Zhang, F. Grotjahn, P. Schlupp, S. Vogt, H. von Wenckstern, A. Thiede, M. Grundmann: *Full-swing, High-gain Inverters Based on ZnSnO JFETs and MESFETs*, IEEE Transact. Electr. Dev. **66**(8), 3376-3381 (2019)

Z. Li, H. Li, Z. Wu, M. Wang, J. Luo, H. Torun, P. Hu, C. Yang, M. Grundmann, X. Liu, Y.Q. Fu: *Advances in designs and mechanisms of semiconducting metal oxide nanostructures for high-precision gas sensors operated at room-temperature*, Mater. Horiz. **6**(3), 470-506 (2019)

M. Lorenz: *Pulsed Laser Deposition*, digital Encyclopedia of Applied Physics eap810, (Wiley-VCH Verlag GmbH & Co. KGaA.,Weinheim, 2019)

J. Michel, D. Splith, J. Rombach, A. Papadogianni, T. Berthold, S. Krischok, M. Grundmann, O. Bierwagen, H. von Wenckstern, M. Himmerlich: *Processing Strategies for High-Performance Schottky Contacts on n-type Oxide Semiconductors: Insights from In_2O_3*, ACS Appl. Mater. Interfaces **11**(30), 27073-27087 (2019)

S. Müller, L. Thyen, D. Splith, A. Reinhardt, H. von Wenckstern, M. Grundmann: *High-quality Schottky Barrier Diodes on β-Gallium Oxide Thin Films on Glass Substrate*, ECS J. Solid State Sci. Techn. **8**(7), Q3126-Q3132 (2019)

C.E. Precker, J. Barzola-Quiquia, P.D. Esquinazi, M. Stiller, M.K. Chan, M. Jaime, Z. Zhang, M. Grundmann: *Record-Breaking Magnetoresistance at the Edge of a Microflake of Natural Graphite*, Adv. Engin. Mater. **21**(12), 1900991: 1-6 (2019)

S. Prucnal, Y. Berencén, M. Wang, L. Rebohle, R. Kudrawiec, M. Polak, V. Zviagin, R. Schmidt-Grund, M. Grundmann, J. Grenzer, M. Turek, A. Drozdziel, K. Pyszniak, J. Zuk, M. Helm, W. Skorupa, S. Zhou: *Band gap renormalization in n-type GeSn alloys made by ion implantation and flash lamp annealing*, J. Appl. Phys. **125**(20), 203105: 1-7 (2019)

S. Richter, H.-G. Zirnstein, J. Zúñiga-Pérez, E. Krüger, C. Deparis, L. Trefflich, C. Sturm, B. Rosenow, M. Grundmann, R. Schmidt-Grund: *Voigt Exceptional Points in an Anisotropic ZnO-based Planar Microcavity: Square-Root Topology, Polarization Vortices, and Circularity*, Phys. Rev. Lett. **123**(22), 227401: 1-7 (2019)

P. Schlupp, H. von Wenckstern, M. Grundmann: *Electrical properties of vertical p-NiO/n-Ga_2O_3 and p-$ZnCo_2O_4$/n-Ga_2O_3 pn-heterodiodes*, Phys. Status Solidi A **216**(7), 1800729: 1-6 (2019)

R. Schmidt-Grund, T. Michalsky, M. Wille, M. Grundmann: *Coherent polariton modes and lasing in ZnO nano- and microwires*, Phys. Status Solidi B **256**(4), 1800462: 1-17 (2019)

R. Staacke, R. John, M. Kneiß, M. Grundmann, J. Meijer: *Highly transparent conductors for optical and microwave access to spin based quantum systems*, NPJ Quantum Information **5**, 98:1-5 (2019)

P. Storm, M. Kneiß, A. Hassa, T. Schultz, D. Splith, H. von Wenckstern, N. Koch, M. Lorenz, M. Grundmann: *Epitaxial κ-$(Al_xGa_{1-x})_2O_3$ Thin Films and Heterostructures grown by Tin-assisted VCCS-PLD*, APL Mater. **7**(11), 111110: 1-8 (2019), (Editor's Pick)

C. Sturm, V. Zviagin, M. Grundmann: *Applicability of the constitutive equations for the determination of the material properties of optically active materials*, Opt. Lett. **44**(6), 1351-1354 (2019) (Editor's Pick)

H. von Wenckstern, M. Kneiß, A. Hassa, P. Storm, M. Grundmann: *A review of the segmented-target approach to combinatorial material synthesis by pulsed-laser deposition*, Phys. Status Solidi B **XXX**, 1900626: 1-13 (2019)

Publications without peer review

M. Grundmann: *Report Halbleiterphysik/Semiconductor Physics 2018*, Universität Leipzig (2019)

M. Grundmann: *Copper iodide - very transparent with many holes and no holes at the same time*, BuildMoNa Annual Report 2017, 26-30 (2019)

R. Karsthof, M. Grundmann, A.M. Anton, F. Kremer: *Polaronic inter-acceptor hopping transport in intrinsically doped nickel oxide*, arxiv: **1905.03537** (2019)

S. Prucnal, Y. Berencén, M. Wang, J. Grenzer, M. Voelskow, R. Hübner, Y. Yamamoto, A. Scheit, F. Bärwolf, V. Zviagin, R. Schmidt-Grund, M. Grundmann, J. Zuk, M. Turek, A. Drozdziel, K. Pyszniak, R. Kudrawiec, M.P. Polak, L. Rebohle, W. Skorupa, M. Helm,

S. Zhou: *Strain and Band-Gap Engineering in Ge-Sn Alloys via P Doping*, arxiv: **1901.01721** (2019)

S. Richter, O. Herrfurth, S. Espinoza, M. Rebarz, M. Kloz, J.A. Leveillee, A. Schleife, S. Zollner, M. Grundmann, J. Andreasson, R. Schmidt-Grund: *Ultrafast dynamics of hot charge carriers in an oxide semiconductor probed by femtosecond spectroscopic ellipsometry*, arxiv: **1902.05832** (2019)

V. Zviagin, C. Sturm, P. Esquinazi, M. Grundmann, R. Schmidt-Grund: *Control of Magnetic Order in Spinel $ZnFe_2O_4$ Thin Films Through Intrinsic Defect Manipulation*, arxiv: **1909.13711** (2019)

Talks

M. Grundmann: *Copper Iodide as Electonic Material*, E-MRS Fall Meeting 2019, Symposium C, Warsaw, Poland, September 2019 (invited)

M. Grundmann: *$(Al,Ga)_2O_3$ and $(In,Ga)_2O_3$ Alloy Semiconductors in Various Crystal Phases: Physical Properties*, Pseudomorphic Epitaxy and Device Perspectives Materials Research Meeting 2019 – Materials Innovation for Sustainable Development Goals (MRM 2019), Yokohama, Japan, December 2019 (plenary)

M. Grundmann: *Amorphous Transparent N-Type and P-Type Electronic Semiconductors for Thin Film Devices*, Materials Research Meeting 2019 - Materials Innovation for Sustainable Development Goals (MRM 2019), Symposium G2 "Materials Frontier for Transparent Advanced Electronics, 5th Bilateral Symposium between E-MRS and MRS-J", Yokohama, Japan, December 2019 (invited)

A. Hassa, H. von Wenckstern, D. Splith, C. Sturm, M. Kneiss, C. Krömmelbein, M. Grundmann: *Ternary Orthorhombic $(In_xGa_{1-x})_2O_3$ and $(Al_xGa_{1-x})_2O_3$ Thin Films: Growth and Material Properties*, DPG spring meeting, Regensburg, Germany, April 2019

A. Hassa, H. von Wenckstern, D. Splith, C. Sturm, M. Kneiss, C. Krömmelbein, M. Grundmann: *Ternary Orthorhombic $(In_xGa_{1-x})_2O_3$ and $(Al_xGa_{1-x})_2O_3$ Thin Films: Growth and Material Properties*, 61st Electronic Materials Conference, Ann Arbor, Michicgan, USA, June 2019

A. Hassa, H. von Wenckstern, D. Splith, C. Sturm, M. Kneiss, M. Grundmann: *Ternary Orthorhombic $(In_xGa_{1-x})_2O_3$ and $(Al_xGa_{1-x})_2O_3$ Thin Films: Growth and Material Properties*, 3rd International Workshop on Gallium Oxide and other Related Materials, Columbus, Ohio, USA, August 2019

O. Herrfurth, S. Richter, M. Rębarz, S. Espinoza, J. Zúñiga-Pérez, A. Schleife, J. Leveillee, S. Zollner, J. Andreasson, M. Grundmann, R. Schmidt-Grund: *Transient birefringence and dichroism of a m-ZnO thin film studied with tSE*, DPG spring meeting, Regensburg, Germany, April 2019

O. Herrfurth, S. Richter, M. Rębarz, S. Espinoza, J. Zúñiga-Pérez, A. Schleife, J. Leveillee, S. Zollner, J. Andreasson, M. Grundmann and R. Schmidt-Grund: *Transient birefringence and dichroism of a m-ZnO thin film studied with tSE*, 8th International Conference on Spectroscopic Ellipsometry, Barcelona, Spain, May 2019

M. Kneiß, A. Hassa, D. Splith, C. Sturm, H. von Wenckstern, M. Lorenz, T. Schultz, N. Koch, M. Grundmann: *Tin-assisted PLD-growth of Epitaxial κ-Ga_2O_3 Thin Films*, DPG spring meeting, Regensburg, Germany, April 2019

M. Kneiß, P. Storm, A .Hassa, D. Splith, C. Sturm, H. von Wenckstern, M. Lorenz, T. Schultz, N. Koch, M. Grundmann: *Epitaxial κ-$(In_xGa_{1-x})_2O_3$ and κ-$(Al_xGa_{1-x})_2O_3$ Thin Films and Heterostructures Deposited by Tin-assisted VCCS-PLD from Radially-segmented Targets*, 61st Electronic Materials Conference, Ann Arbor, Michigan, USA, June 2019

M. Kneiß, P. Storm, A. Hassa, D. Splith, C. Sturm, H. von Wenckstern, M. Lorenz, T. Schultz, N. Koch, M. Grundmann: *Epitaxial κ-$(In_xGa_{1-x})_2O_3$ and κ-$(Al_xGa_{1-x})_2O_3$ Thin Films and Heterostructures Deposited by Tin-assisted VCCS-PLD from Radially-segmented Targets*, 3rd International Workshop on Gallium Oxide and Other Related Materials, Columbus, Ohio, USA, August 2019

M. Kneiß, P. Storm, A. Hassa, D. Splith, C. Sturm, H. von Wenckstern, M. Lorenz, T. Schultz, N. Koch, M. Grundmann: *Epitaxial κ-$(In_xGa_{1-x})_2O_3$ and κ-$(Al_xGa_{1-x})_2O_3$ Thin Films and Heterostructures Deposited by Tin-assisted VCCS-PLD from Radially-segmented Targets*, Transparent Conductive Oxides, Leipzig, Germany, September 2019

M. Kneiß, P. Storm, A. Hassa, D. Splith, C. Sturm, H. von Wenckstern, M. Lorenz, T. Schultz, N. Koch, M. Grundmann: *Epitaxial κ-$(In_xGa_{1-x})_2O_3$ and κ-$(Al_xGa_{1-x})_2O_3$ Thin Films and Heterostructures Deposited by Tin-assisted VCCS-PLD from Radially-segmented Targets*, Semi Annual Meeting of the Leibniz Science Campus GraFOx, Berlin, Germany, November 2019

O. Lahr, S. Vogt, H. von Wenckstern, M. Grundmann: *Integrated Logic Circuits Based on Amorphous Zinc-Tin-Oxide Thin Films Deposited at Room Temperature*, DPG spring meeting, Regensburg, Germany, April 2019

O. Lahr, H. von Wenckstern, F. Grotjahn, A. Thiede, M. Grundmann: *Devices and Integrated Logic Circuits Based on Amorphous, Room-temperature-deposited Zinc-Tin-Oxide*, FFlexCom Plenary Meeting 2019, Dresden, Oktober 2019

M. Lorenz: *Origin of High Magnetoelectric Coupling in Multiferroic Epitaxial $BiFeO_3$-$BaTiO_3$ Thin Film Composites*, International Congress on Advanced Materials Sciences and Engineering 2019 (AMSE-2019), Osaka, Japan, July 2019 (invited)

M. Lorenz: *Educational system in Germany – Magnetoelectric and multiferroic epitaxial $BiFeO_3$-$BaTiO_3$ thin film composites*, Kinki University, Japan, July 2019, (invited)

A. Reinhardt, A. Welk, H. von Wenckstern, M. Grundmann: *Process optimization for the sputter deposition of amorphous zinc oxynitride thin films*, 28th International Conference on Amorphous and Nanocrystalline Semiconductors, Palaiseau, France, August 2019

A. Reinhardt, A. Welk, H. von Wenckstern, M. Grundmann: *Process optimization for the sputter deposition of amorphous zinc oxynitride thin films*, International Workshop on Transparent Conductive Oxides, Leipzig, Germany, September 2019

P. Schlupp, S. Vogt, H. von Wenckstern, M. Grundmann: *Influence of the cation ratio on defect formation and properties in zinc tin oxide thin films*, International Workshop on Transparent Conductive Oxides, Leipzig, Germany, September 2019

F. Schöppach, R. Karsthof, D. Splith, H. von Wenckstern, M. Grundmann: *Realization of MESFET and inverter devices based on Mg-doped* In_2O_3, DPG spring meeting, Regensburg, Germany, April 2019

D. Splith , A. Hassa , M. Kneiß , M. Grundmann: *Exploration of orthorhombic* $(In,Ga)_2O_3$ *and* $(Al,Ga)_2O_3$ *by compositional screening*, SPIE Photonics West, San Francisco, USA, February 2019 (invited, held by H. von Wenckstern)

D. Splith: *Highly rectifying contacts on* Ga_2O_3, In_2O_3 *and* $(In,Ga)_2O_3$ *thin films*, DPG spring meeting, Regensburg, Germany, April 2019

C. Sturm, S. Höfer, K. Hingerl, T. G. Mayerhöfer, M. Grundmann: *Dielectric function decomposition by dipole orientation distribution*, 8th International Conference on Spectroscopic Ellipsometry, Barcelona, Spain, May 2019 (invited)

C. Sturm, A. Müller, A. Hassa, M. Kneiß, H. von Wenckstern, M. Grundmann: *Dielectric function* κ*-*$(In,Al,Ga)_2O_3$ *thin films*, International Workshop on Gallium Oxide and Related Materials, Columbus (Ohio), United States of America, August 2019

C. Sturm: *Ellipsometry on anisotropic materials: Determination and application of the dielectric tensor*, 4th ELIps user workshop, Dolní Břežany, Czech Republic, November 2019 (invited)

L.Trefflich, R. Schmidt-Grund, C. Sturm, M. Grundmann: *Fabrication and luminescence properties of carbon-nandot-based planar microcavities*, Annual BuildMoNa Conference, Leipzig, Germany, March 2019

H. von Wenckstern: *Fotovoltaische, thermoelektrische und elektrochrome Materialien und Bauelemente auf Glas*, Thementage GLAS "glass connects – Glas verbindet", Düsseldorf, Germany, November 2019 (invited)

V. Zviagin, P. Huth, C. Sturm, J. Lenzner, A. Setzer, R. Denecke, P. Esquinazi, M. Grundmann, R. Schmidt-Grund: *Spectroscopic investigation of disorder in spinel ferrite thin films*, DPG spring meeting, Regensburg, Germany, April 2019

V. Zviagin, P. Huth, C. Sturm, J. Lenzner, A. Setzer, R. Denecke, P. Esquinazi, M. Grundmann, R. Schmidt-Grund: *Spectroscopic study of cationic order in spinel ferrite thin films*, 8th International Conference on Spectroscopic Ellipsometry (ICSE-8), Barcelona, Spain, May 2019

V. Zviagin, P. Huth, C. Sturm, J. Lenzner, A. Setzer, R. Denecke, P. Esquinazi, M. Grundmann, R. Schmidt-Grund: *Ellipsometric determination of cation disorder in magnetic spinel ferrites*, 4th ELIps user workshop, Dolní Břežany, Czech Republic, November 2019

Posters

M. Bar, D. Splith, H. von Wenckstern, M. Grundmann: *Finite element simulation and experimental characterization of field-effect transistors based on amorphous zinc tin oxide*, DPG spring meeting, Regensburg, Germany, April 2019

F.-F. Delatowski, C. Sturm, M. Lorenz, F. Jung, S. Hohenberger, M. Grundmann: *Optical properties of oxygen doped TiN thin films*, DPG spring meeting, Regensburg, Germany, April 2019

M. Grundmann, M. Lorenz, S. Hohenberger, E. Rose: *Pseudomorphic Strain in Corundum-Phase Al-rich (Al,Ga)$_2$O$_3$ Thin Films Grown on R-plane Sapphire*, DPG spring meeting, Regensburg, Germany, April 2019

A. Hassa, M. Kneiß, D. Splith, H. von Wenckstern, C. Sturm, M. Grundmann: *Ternary Orthorhombic (In,Ga,Al)$_2$O$_3$ Thin Films: Growth and Material Properties*, TCO 2019, Leipzig, Germany, September 2019

S. Henn, E. Krüger, C. Sturm, A. Dadgar, M. Wieneke, M. Grundmann. R. Schmidt-Grund: *Exceptional Points in anisotropic thin films*, DPG fall meeting, Freiburg, Germany, September 2019

O. Herrfurth , T. Pflug , M. Olbrich , M. Grundmann, A. Horn and R. Schmidt-Grund: *Hot-carrier propagation in ZnO studied with femtosecond pump-probe imaging ellipsometry*, 4th ELIps user workshop, Dolní Břežany, Czech Republic, November 2019

T. Jawinski, R. Pickenhain, L. Wägele, M. Lorenz, R. Scheer, M. Grundmann, H. von Wenckstern: *Properties of In$_2$S$_3$:V – a Potential Material for Intermediate Band Solar Cells*, DPG spring meeting, Regensburg, Germany, April 2019

T. Jawinski, R. Pickenhain, L. Wägele, R. Scheer, M. Grundmann, H. von Wenckstern: *Photocurrent measurements and deep level transient spectroscopy on In$_2$S$_3$:V intermediate band solar cells*, European Photovoltaic Solar Energy Conference (EU PVSEC), Marseille, Frace, September 2019

M. Kneiß, A. Hassa, P. Storm, D. Splith, H. von Wenckstern, M. Lorenz, M. Grundmann: *PLD-growth of Epitaxial κ-(In$_x$,Ga$_{1-x}$)$_2$O$_3$/κ-Ga$_2$O$_3$ Heterostructures Using Radially-segmented Targets*, Annual BuildMoNa Conference, Leipzig, Germany, March 2019

M. Kneiß, A. Hassa, P. Storm, D. Splith, H. von Wenckstern, M. Lorenz, M. Grundmann: *PLD-growth of Epitaxial κ-(In$_x$,Ga$_{1-x}$)$_2$O$_3$/κ-Ga$_2$O$_3$ Heterostructures Using Radially-segmented Targets*, DPG spring meeting, Regensburg, Germany, April 2019

C. Krömmelbein, A. Hassa, D. Splith, M. Kneiß, H. von Wenckstern, M. Grundmann: *Structural, Optical and Electrical Properties of Zr-doped κ-(In$_x$Ga$_{1-x}$)$_2$O$_3$ Thin Films*, DPG spring meeting, Regensburg, Germany, April 2019

C. Krömmelbein, A. Hassa, D. Splith, M. Kneiß, H. von Wenckstern, M. Grundmann: *Electrical Properties of Zr-doped κ-(In$_x$Ga$_{1-x}$)$_2$O$_3$ Thin Films Grown by CCS-PLD*, Electronic Materials Conference, Ann Arbor, Michigan, USA, June 2019

E. Krüger, S. Richter, H.-G. Zirnstein, J. Zúñiga-Pérez, C. Deparis, L. Trefflich, C. Sturm , B. Rosenow, M. Grundmann, R. Schmidt-Grund: *Voigt exceptional-points in anisotropic ZnO-based photonic structures*, DPG spring meeting, Regensburg, Germany, April 2019

E. Krüger, C. Sturm, S. Richter, H.-G. Zirnstein, S. Henn, J. Zúñiga-Pérez, C. Deparis, L. Trefflich, B. Rosenow, M. Grundmann, R. Schmidt-Grund: *From Singular Optic Axes in Biaxial Crystals to Exceptional Points in Anisotropic Planar Microcavities*, 8th International Conference on Spectroscopic Ellipsometry, Barcelona, Spain, May 2019

E. Krüger, S. Richter, S. Henn, H.-G. Zirnstein, J. Zúñiga-Pérez, C. Deparis, L. Trefflich, C. Sturm, B. Rosenow, R. Schmidt-Grund, M. Grundmann: *Towards topological non-trivial photonic systems based on dielectric planar heterostructures*, BuildMoNa-Workshop (2019-T4), Zingst, Germany, October 2019

O. Lahr, H. von Wenckstern, M. Grundmann: *Dynamic Behavior of Amorphous Zinc-Tin-Oxide-based Devices*, TCO 2019, Leipzig, Germany, September 2019

A. Müller, C. Sturm, A. Hassa, M. Kneiß, H. von Wenkstern, M. Grundmann: *IR-VUV Dielectric Function of κ-(In,Ga,Al)$_2$O$_3$ Thin Films*, Transparent Conductive Oxides – Fundamentals and Applications, Leipzig, Germany, September 2019

A. Müller, C. Sturm, M. Kneiß, V. Zviagin, M. Grundmann: *Optical phonon modes and dielectric funktion of orthorhombic κ-Ga$_2$O$_3$ thin films*, DPG spring meeting, Regensburg, Germany, April 2019

S. Müller, D. Splith, H. von Wenckstern, M. Grundmann: *Growth of MoO$_3$ Microflakes by Thermal Evaporation*, DPG spring meeting, Regensburg, Germany, April 2019

A. Reinhardt, A. Welk, H. von Wenckstern, M. Grundmann, T. Schultz, N. Koch: *Optimizing the sputter deposition process of amorphous zinc oxynitride thin films*, DPG spring meeting, Regensburg, Germany, April 2019

P. Schlupp, H. von Wenckstern, M Grundmann: *Structural, electrical and optical porperties of W$_x$Mo$_{1-x}$O$_3$ thin films fabricated by pulsed laser deposition*, DPG spring meeting, Regensburg, Germany, April 2019

P. Schlupp, L.L. Bock, H. von Wenckstern, M. Grundmann: *Electrochromic switching of WO$_3$ and NiO thin films due to (de)intercalation of lithium ions in propylene carbonate*, TCO 2019, Leipzig, Germany, September 2019

F. Schöppach, D. Splith, H. von Wenckstern, M. Grundmann: *Properties of MESFET and inverter devices based on In$_2$O$_3$*, TCO 2019, Leipzig, Germany, September 2019

D. Splith, A. Hassa, P. Schlupp, H. von Wenckstern, M. Grundmann: *Highly rectifying contacts on (In,Ga)$_2$O$_3$ thin films grown by pulsed laser deposition*, Compound Semiconductor Week, Nara, Japan, Mai 2019

D. Splith, A. Hassa, P. Schlupp, H. von Wenckstern, M. Grundmann: *Highly rectifying contacts on (In,Ga)$_2$O$_3$ thin films grown by pulsed laser deposition*, International Workshop on Gallium Oxide and Related Materials, Columbus, Ohio, USA, August 2019

D. Splith, S. Müller, H. von Wenckstern, M. Grundmann: *Molybdenum oxide nanoflakes: Growth and electrical characterization*, TCO 2019, Leipzig, Germany, September 2019

P. Storm, M. Kneiß, D. Splith, H. von Wenckstern, M. Lorenz, M. Grundmann: *Characterization of κ-(In,Al,Ga)$_2$O$_3$ Thin Films grown by VCCS PLD*, DPG spring meeting, Regensburg, Germany, April 2019

T. Stralka, D. Splith, M. Kneiß, C. Yang, H. von Wenckstern, M. Grundmann: *Copper iodide: AFM studies and beyond*, TCO 2019, Leipzig, Germany, September 2019

C. Sturm, A. Müller, A. Hassa, M. Kneiß, V. Zviagin, H. von Wenckstern, M. Grundmann: *Dielectric Function of κ-(In,Al,Ga)$_2$O$_3$ thin films*, 8th International Conference on Spectroscopic Ellipsometry, Barcelona, Spain, May 2019

C. Sturm, V. Zviagin, M. Grundmann: *Applicability of the constitutive equations for the determination of the material properties of optically active materials*, 8th International Conference on Spectroscopic Ellipsometry, Barcelona, Spain, May 2019

L. Trefflich, F. Dissinger, N. Weizenmann, C. Sturm, S. R. Waldvogel, R. Seidel, M. Grundmann, R. Schmidt-Grund: *Production and characterization of carbon-nandot-based planar microcavities*, DPG spring meeting, Regensburg, Germany, April 2019

L. Trefflich, F. Dissinger, N. Weizenmann, C. Sturm, R. Schmidt-Grund, R. Seidel, S. R. Waldvogel, M. Grundmann: *Optical properties of carbon-nanodot-based planar microcavities*, BuildMoNa-Workshop (2019-T4), Zingst, Germany, October 2019

A. Welk, A. Reinhardt, O. Herrfurth, H. von Wenckstern, M. Grundmann: *Tuning material properties of ZnON by Mg^{2+} cationic substitution*, 28th International Conference on Amorphous and Nanocrystalline Semiconductors, Palaiseau, France, August 2019

A. Welk, A. Reinhardt, O. Herrfurth, H. von Wenckstern, M. Grundmann: *Tuning material properties of ZnON by Mg^{2+} cationic substitution*, International Workshop on Transparent Conductive Oxides, Leipzig, Germany, September 2019

V. Zviagin, P. Huth, C. Sturm, J. Lenzner, A. Setzer, R. Denecke, P. Esquinazi, M. Grundmann, R. Schmidt-Grund: *Origin of ferrimagnetic properties in disordered spinel ferrite thin films*, DPG spring meeting, Regensburg, Germany, April 2019

V. Zviagin, P. Huth, C. Sturm, J. Lenzner, A. Setzer, R. Denecke, P. Esquinazi, M. Grundmann, R. Schmidt-Grund: *Ellipsometric determination of cation disorder in magnetic spinel ferrites*, 4th ELIps Workshop, Dolní Brezany, Czech Republic, November 2019

5

Graduations

Doctorate

- Vitaly Zviagin
  Ellipsometric Determination of Cation Disorder in Magnetically Ordered Spinel Ferrite Thin Films
  July 2019

Master

- Yousif Abou Leila
  Reactive Etching of Ga_2O_3 and Electrical Characterization of Ga_2O_3-based Diodes
  January 2019
- Michael Bar
  Simulation und Herstellung von lateralen und vertikalen Feldeffekttransistoren auf Basis von Zink-Zinnoxid
  November 2019
- Ron Hildebrandt
  Intermediate Band Solar Cells based on Indium Sulfide
  January 2019
- Catharina Krömmelbein
  Growth, Structural and Electrical Characterization of Ternary, Orthorhombic Group-III Sesquioxides
  October 2019
- Oliver Lahr
  Ringoszillatoren auf der Basis von ZTO Dünnfilmen
  January 2019
- Fabian Schöppach
  Bipolar and transparent devices: Case studies of transparent solar cells and field-effect transistors
  February 2019

- Philipp Storm
  Tin-assisted Growth of Epitaxial κ-$(Al_xGa_{1-x})_2O_3$ Thin Films and Heterostructures by VCCS-PLD
  September 2019
- Laurenz Thyen
  Charakterisierung von β-Galliumoxid Dünnfilmen auf Quarzglas durch Hochtemperaturmessungen an Pt-Schottky-Kontakten
  June 2019
- Jonathan Wernerson
  Zinc-Tin-Oxide-Based Vertical Field-Effect Transistors
  July 2019

Bachelor

- Sebastian Bürger
  Gallium incorporation into bixbyite In_2O_3 thin films
  September 2019
- Felix-Florian Delatowski
  Strukturelle und optische Eigenschaften von sauerstoffdotierten TiN Dünnfilmen
  June 2019
- Mario Klebahn
  Si-dotierte β-Galliumoxid-Dünnfilme auf (001)-Al_2O_3 mit Fehlschnitt in <110>-Richtung
  September 2019
- Eduard Rose
  Sputter-Abscheidung von Sn-dotierten CuI-Dünnfilmen
  January 2019
- Christopher Walter
  Untersuchungen von MgNiO:Li-Dünnfilmen – strukturelle, optische und elektrische Eigenschaften
  October 2019

6

Guests

- Fangjuan Geng
  University of Jinan, Jinan, PR China
  China Scholarship Council: Agreement for Study Abroad for CSC Sponsored Chinese Citizens
  September 2019 – March 2021
- Dr.-Ing. Krzysztof Grzegorz Dorywalski
  Politechnika Koszalinska, Koszalin, Poland
  August 2019 – September 2019
- Michitaka Fukumoto
  Japan Society for the Promotion of Science: Overseas Challenge Program for Young Researchers
  April 2018 – March 2019
- Dr. Wenlei Yu
  Wenzhou Medical University, Zhejiang, PR China
  August 2018 – July 2019

Author Index

B

Berthold, T. 38
Bierwagen, O. 38

D

Dadgar, A. 43
Delatowski, F. 56
Denecke, R. 50
Dissinger, F. 54

E

Esquinazi, P. 50

F

Fares, C. 37

G

Grundmann, M. . 17, 19, 21, 23, 25, 27, 29, 31, 33, 35, 37, 38, 43, 44, 48, 50, 52–54, 56, 58

H

Hassa, A. 23, 25, 27, 29, 52
Henn, S. 44
Hennemann, C. 54
Herrfurth, O. 48
Hildebrandt, R. 43
Himmerlich, M. 38
Hohenberger, S. 40, 56
Horn, A. 48

J

Jung, F. 56

K

Kneiss, M. 23, 25, 27, 29, 37, 52
Koch, N. 25, 27
Kremkow, J. 53
Krischok, S. 38
Krüger, E. 44, 53

L

Lahr, O. 17
Lorenz, M. 25, 27, 29, 40, 56

M

Michel, J. 38
Märcker, A. 58
Müller, A. 52
Müller, S. 33

O

Olbrich, M. 48

P

Papadogianni, A. 38
Pearton, S. 37

Pflug, T. 48

R

Reinhardt, A. 21, 33
Ren, F. 37
Rombach, J. 38

S

Schlupp, P. 19, 31
Schmidt-Grund, R. 44, 48, 50, 54
Schultz, T. 25, 27
Splith, D. 23, 25, 27, 29, 31, 33, 38
Storm, P. 23, 27
Sturm, C. 25, 29, 43, 44, 50, 52–54, 56

T

Tadjer, M. 37
Thyen, L. 33
Trefflich, L. 54

V

Vogt, S. 17, 19
von Wenckstern, H. . 17, 19, 21, 23, 25, 27, 29, 31, 33, 37, 38

W

Waldvogel, S.R. 54
Wieneke, M. 43

Y

Yang, C. 53

Z

Zviagin, V. 50, 53


UNIVERSITÄT LEIPZIG
TCO2019
Transparent Conductive Oxides – Fundamentals and Applications
23-27 September 2019
Historical Focus: 120 Years of Drude Theory of the Electron Gas
Monday, 23 Sept. 2019
13h s.t.
Everybody is welcome to these lectures
The Bädeker Lecture
Wednesday, 25 September 2019
17h s.t.
Novel Transparent Oxide Semiconductors: Design, Property and Application
Felix Bloch Institute for Solid State Physics
Lecture Hall for Theoretical Physics
Linnéstraße 5, 04103 Leipzig
Invited Speakers
Program Committee
Registration via www.buildmona.de/TCO2019
BuildMoNa
Malvern Panalytical
DFG
FOR 2857
FHI